# Influence of Surface Preparation on the Chemical Vapor Deposition of W on Si(100) and Polycrystalline TiN Surfaces

Scott Len Lantz

A dissertation presented to the faculty of the
Oregon Graduate Institute of Science & Technology
in partial fulfillment of the requirements for the degree of

Doctor of Philosophy
in
Electrical Engineering

January 1995

The dissertation "Influence of Surface Preparation on the Chemical Vapor Deposition of W on Si(100) and Polycrystalline TiN Surfaces" by Scott Len Lantz has been examined and approved by the following Examination Committee:

Anthony E. Bell
Professor
Thesis Advisor

Rajendra Solanki
Professor

Wayne K. Ford
Intel Corporation

Don Danielson
Intel Corporation

# TABLE OF CONTENTS


TABLE OF CONTENTS ..... *iii*

ABSTRACT ..... *v*

CHAPTER 1 INTRODUCTION ..... 1

1.1 Historical development of W CVD ..... 1

1.2 Technological challenges of W CVD ..... 2

1.3 References for Chapter 1 ..... 6

CHAPTER 2 EXPERIMENTAL PROCEDURES ..... 9

2.1 Introduction ..... 9

2.2 Sample heating and temperature measurement ..... 13

2.3 Ar sputter cleaning ..... 13

2.4 Gas dosing procedures and system characterization ..... 16

2.4.1 Hardware description ..... 16

2.4.2 Dosing procedures ..... 19

2.4.3 Gas flow rates ..... 20

22.4.4 Sample positioning ..... 22

2.5 Auger electron spectroscopy measurements ..... 25

2.6 References for Chapter 2 ..... 26

CHAPTER 3 $WF_6$ REACTIONS WITH Si(100) SURFACES ..... 27

3.1 Introduction ..... 27

3.2 Sample Preparation and Characterization ..... 28

3.3 Results ..... 29

3.3.1 $WF_6$ + Si(100) After Sputter Clean ..... 29

3.3.2 $WF_6$ + Si(100) After HF Clean ..... 35

3.4 Discussion ..... 42

3.4.1 Reaction Kinetics and Pathways ..... 42

3.4.2 Porous morphology and Induction Period ..... 47

3.5 References for Chapter 3 ..... 51
CHAPTER 4 $WF_6$ AND $SiH_4$ REACTIONS WITH TiN SURFACES ..... 55
4.1 Introduction ..... 55
4.2 TiN sample preparation and characterization ..... 57
4.2.1 RIS TiN ..... 57
4.2.2 MOCVD TiN ..... 60
4.2.3 LPCVD TiN ..... 64
4.2.4 $WF_6$ and $SiH_4$ dosing procedures ..... 71
4.3 $WF_6$ reactions with TiN, no pre-cleaning ..... 71
4.4 $WF_6$ reactions with TiN,with pre-cleaning ..... 82
4.5 $SiH_4$ reactions with TiN ..... 91
4.6 Sequential $WF_6$ and $SiH_4$ reactions with TiN ..... 95
4.7 Discussion ..... 99
4.7.1 Reaction Pathways ..... 99
4.7.2 Surface Chemistry and Morphology Influences on $WF_6$ Reactions ..... 99
4.7.3 W Thin Film Growth Modes ..... 100
4.7.4 $WF_6$ Adsorption Kinetic Models ..... 105
4.7.5 Interpretation of $SiH_4$ reactions ..... 112
4.8 References for Chapter 4 ..... 113
CHAPTER 5. SUMMARY AND CONCLUSIONS ..... 117
APPENDIX A ELECTRON BEAM AND INSTRUMENTAL EFFECTS ..... 119

# ABSTRACT

The chemical reactions for initial stages of CVD (chemical vapor deposition) W film growth were studied in an ultra high vacuum (UHV) environment. A UHV environment was chosen in order to isolate and characterize the effects that surface perparation may have on W CVD processes typcially encountered in semiconductor manufacturing. A UHV gas dosing system was specially contructed in order to simulate conditions of CVD film growth which could be studied *in situ* with Auger electron spectroscopy (AES). The W CVD reactions were studied on Si(100) and polycrystalline thin film TiN samples, which were prepared and/or pretreated in a variety of ways. The deposition rate of W from the $WF_6$ + Si(100) reaction and the W/Si interface morphology were both sensitive to surface oxygen. A thin (~ 1 nm) surface oxide layer can impede W film growth at moderate deposition temperatures (300 to 450 °C), and lead to an interface structure with large scale porosity (up to 300 nm pore size) at temperatures above 450 °C. $WF_6$ reactions with TiN substrates nucleate W films *via* kinetics that are sensitive to the chemical and physical properties of the TiN surfaces. Between the temperatures of 300 and 550 °C the effective activation energy for the clean surface is 0.04 eV and for the oxidized surface is 0.6 eV. A $SiH_4$ pre-exposure of clean and oxidized TiN accelerates the subsequent $WF_6$ reaction by depositing Si. Comparisons of the $WF_6$ and $SiH_4$ reactions on surfaces of TiN films deposited by two different CVD methods show that the initial $WF_6$ reaction rates were the same for all of the TiN samples, but the reaction deposited more W on the CVD TiN films which had greater surface roughness values.

# 1

# INTRODUCTION

## 1.1 Historical development of W CVD

The trend in scaling of integrated circuits into submicron dimensions has placed considerable challenges on the use of sputter deposited Al for metal interconnects. One of the critical drawbacks in conventional sputtered Al technology for multilevel metallization has been poor step coverage at contact and via holes, especially when there are high depth-to-diameter aspect ratios. This problem is due to shadowing effects which degrade Al film growth uniformity during sputter deposition which in turn can lead to premature open failures induced by electromigration. Because of these reliability concerns, multilevel metal design rules have had to incorporate larger diameter vias, tapered side walls, and Al pads above and below the vias to prevent unevenly covered structures. The implementation of these strategies however, has resulted in progressively larger consumption of premium device area. Since this trend contradicts to the push for continued miniaturization of circuits, alternate metallization schemes, including CVD W have received an enormous amount of attention [1-9].

With the recent scaling of circuit design rules to less than 1 micron, CVD W began to be used in place of sputtered Al for contact and via fill in multilevel metallization structures. CVD W has become the technique of choice for filling submicron contacts and vias for a variety of reasons. CVD W is a planar-compatible process with inherently good step coverage, and no additional metal pads nor sloped sidewalls are required. W has an additional advantage of excellent resistance to electromigration phenomena associated with high current densities found in small diameter contacts and vias [10].

There are generally two approaches to using CVD W for contact and via fill: selective deposition and blanket deposition. The basic process steps for the selective process are illustrated in Fig. 1-1. A W-containing gas, $WF_6$ is used as the source of W. A film of W is deposited on the

wafer surface as the $WF_6$ is chemically reduced to metallic W via surface reactions. The most common methods of reducing the $WF_6$ are with $H_2$, $SiH_4$, or with the substrate itself [11,12]. The process is *selective* in that $WF_6$ reduction takes place only on conducting surfaces like Si and metals and not on insulating $SiO_2$ or $Si_3N_4$ surfaces. The selectivity is due mostly to large differences in reaction thermodynamics [13], but extrinsic parameters such as gas partial pressures [14], and substrate temperature [15-17] can also be of influence.

The method for depositing W most commonly used in production today is the blanket film deposition. The process steps are illustrated in Fig. 1-2. After the vias are formed and an adhesion layer is deposited, a continuous film of W is deposited over the entire wafer. The top layer is then removed, leaving behind the W plugs. The film removal step can be accomplished with an RF plasma etch [18,19], or chemical-mechanical polishing [20]. The wafer surface is then planar and is ready for the next layer of metallization.

The adhesion layer which is used to promote uniform W film growth on all exposed surfaces, must meet several criteria. In addition to providing good adhesion, it also must be compatible with the $WF_6$ chemistry, have reasonable step coverage, and it must have low contact resistance. Although many other films have been considered [21-23] for blanket W adhesion layer applications, sputter-deposited titanium nitride (TiN) is the most commonly used material. This is because in addition to meeting all of the above requirements, it was already being used as a diffusion barrier [24] for Al metallization. W can be deposited onto TiN with either $H_2$ reduction or $SiH_4$ reduction. $H_2$ reduction generally gives a higher purity film [12] and better thickness uniformity [25] and step coverage [26]. The big drawbacks of $H_2$ reduction on TiN however are poor nucleation, possible attack of underlying substrates by the $WF_6$, and low growth rates. Incubation times of several minutes [27,28] have also been reported. $SiH_4$ reduction has poor step coverage but readily deposits onto TiN. Therefore the blanket W process usually begins with a $SiH_4$ reduction step, depositing about 10 nm of W, then continues with the $H_2$ reduction for the rest.

### 1.2 Technological challenges of W CVD

Throughout the 1980's there was been a tremendous concentration of effort put toward the development of a manufacturable selective W CVD process [2-9]. The selective process is, in principle a simpler and more efficient process, requiring fewer steps, using less equipment and materials than the blanket process described below. In fact, today there are over 80 patents granted [29] for selective W processes. In spite of this enormous effort and apparent success

however, the technique has still not been incorporated into high-volume manufacturing. Most of the CVD equipment manufacturers have abandoned efforts at developing a commercial selective W reactor. This lack of commercial success is due primarily to selectivity loss, where aberrant nucleation sites form on insulator surfaces which then grow into W islands that can decrease product performance and reliability by creating direct electrical short circuits or current leakage paths. This is illustrated in Fig. 1-1(d) along some of the other concerns with the selective process, which include encroachment [30] and wormhole [30,31] damage to the Si substrate (Si consumption), excessive W surface roughness [32,33], and non-uniform W growth rates [12].

The loss of selectivity has been attributed to several different reasons including undesirable reaction products [34] and reactor cleanliness [12]. A large amount of research effort has focused on one or more of these explanations, sometimes showing a correlation to selectively loss. Relatively few studies however have addressed the issue of how surface preparation influences the individual deposition reactions and overall W film quality. In Chapter 3 these questions are addressed in detail for the simplest case, the $WF_6$ + Si(100) reaction. The kinetics of the $WF_6$ + Si reaction are studied over a temperature range of 300-550 °C for sets of samples cleaned in different ways. The properties of the deposited W films are characterized with Auger depth profiles, X-ray diffraction, and high-resolution SEM.

Although the blanket W technique is more widely used, it is not without its own set of concerns. Surface roughness of the deposited W can lead to lack of control over the etch endpoint [12,22]. Film uniformity across the wafer surfaces can be difficult to control, especially when the local deposition rate is mass flow limited. This particular problem can be directly influenced by surface chemistry and therefore substrate preparation. The results in Chapter 4 address this issue by examining how variations in the TiN surface properties influence the initial $WF_6$ and $SiH_4$ reactions. A variety of TiN surfaces were studied including those deposited by reactive ion sputtering (RIS), and also by chemical vapor deposition. Different cleaning techniques were employed to elucidate the influence of surface oxidation, residual contamination, and surface morphology on the initial reactions.

This thesis is organized into five Chapters and one Appendix. Chapter 2 describes the system hardware design and experimental procedures used. Chapter 3 describes the results obtained in studying $WF_6$ + Si(100) reactions. Results for $WF_6$ and $SiH_4$ reactions with TiN surfaces are described in Chapter 4. Chapter 5 summarizes the key results. Appendix A addresses the effects of instrument settings and electron beam interactions on the Auger data.

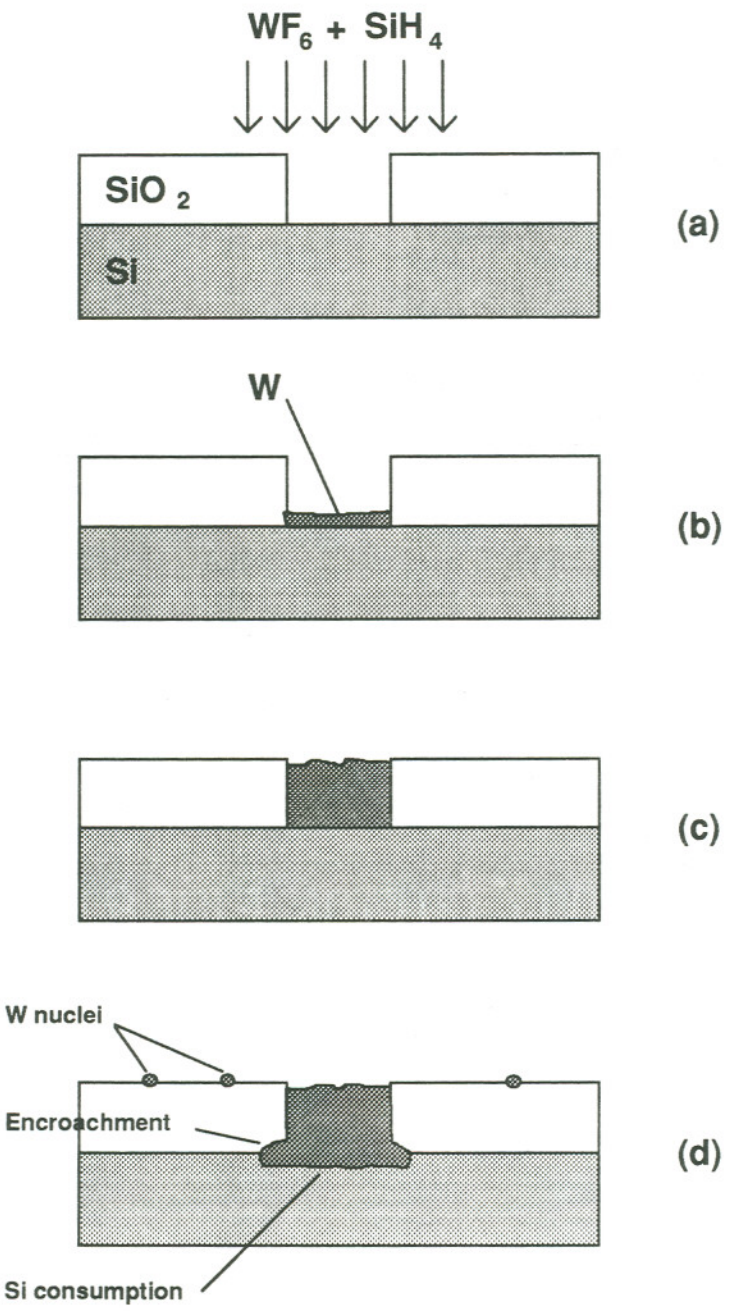


Figure 1-1. Selective W process steps. (a) Reduction of $WF_6$ by exposed Si surfaces, (b) Growth of W film on exposed Si surface, (c) Complete via fill without W deposition on dielectric surfaces, and (d) Typical manufacturing concerns with the selective process.

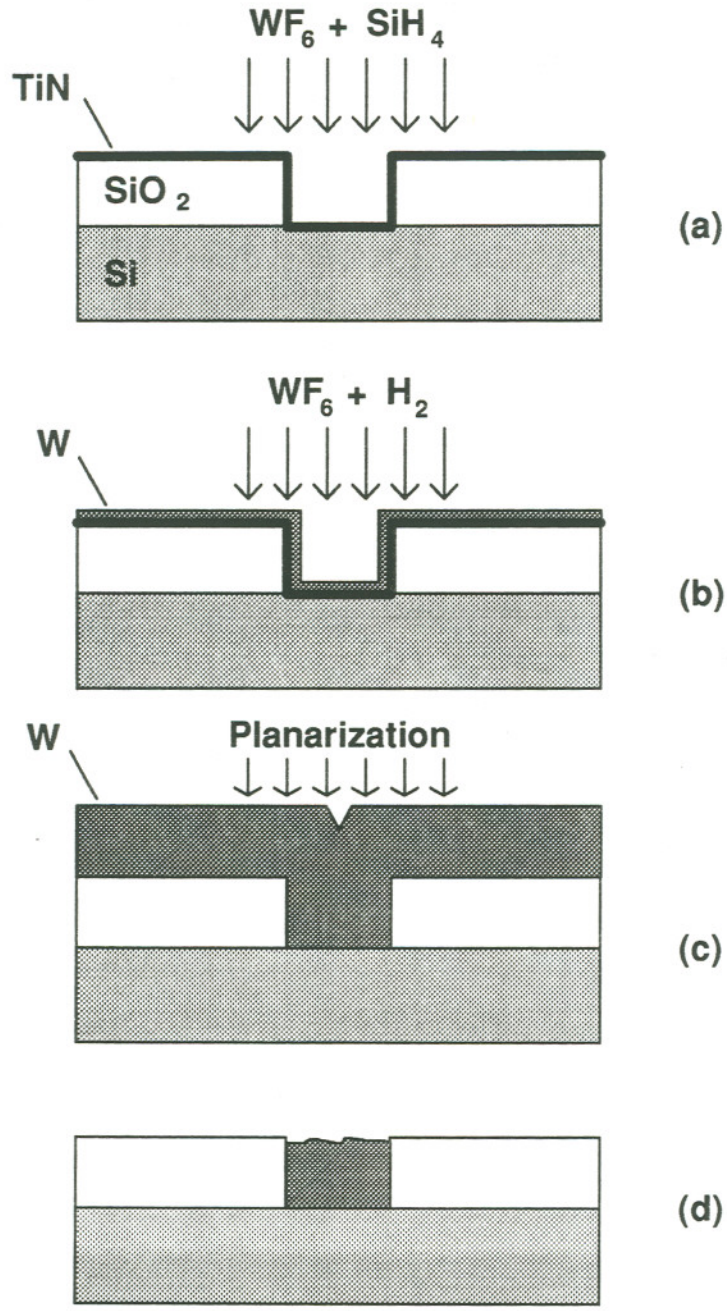


Figure 1-2. Blanket W CVD process steps. (a) Nucleation step via $SiH_4$ reduction of $WF_6$, (b) Hydrogen reduction step, (c) Planarization step by plasma etch or chemical-mechanical polish, and (d) Planarized W-filled vias ready for next metallization step.

## 1.3 References for Chapter 1

1-1. M.L Green, AIP Conf. Proc. 167, 173 (1988).

1-2. R.S. Blewer, ed., *Tungsten and Other Refractory Metals for VLSI Applications*, Materials Research Society, Pittsburgh, PA, (1986).

1-3. E.K. Broadbent, ed., *Tungsten and Other Refractory Metals for VLSI Applications II*, Materials Research Society, Pittsburgh, PA, (1987).

1-4. V.A. Wells, ed., *Tungsten and Other Refractory Metals for VLSI Applications III*, Materials Research Society, Pittsburgh, PA, (1988).

1-5. R.S. Blewer and C. McConica, ed., *Tungsten and Other Refractory Metals for VLSI Applications IV*, Materials Research Society, Pittsburgh, PA, (1989).

1-6. S.S. Wong and S. Furukawa, eds., *Tungsten and Other Advanced Metals for VLSI/ULSI Applications V*, Materials Research Society, Pittsburgh, PA, (1990).

1-7. G.C. Smith and R. Blumenthal, eds., *Tungsten and Other Refractory Metals for ULSI Applications in 1990*, Materials Research Society, Pittsburgh, PA, (1991).

1-8. V.V.S. Rana, R.V. Joshi, and I. Ohdomari, eds., *Advanced Metallization for ULSI Applications*, Materials Research Society, Pittsburgh, PA, (1992).

1-9. T.S. Cale, F.S. Pintchovski, eds., *Advanced Metallization for ULSI Applications 1992*, Materials Research Society, Pittsburgh, PA, (1993).

1-10. P. Gargini, C. Tseng, and M.H. Woods, 1982 Intl. Reliability Phys. Symp. 66, (1982).

1-11. E.K. Broadbent and C.L. Ramiller, J. Electrochem. Soc. 131(6), 1427 (1984).

1-12. J.E.J. Schmitz, *Chemical Vapor Deposition of Tungsten and Tungsten Silicides*, Noyes Publications, New Park, NJ, (1992).

1-13. J-O Carlsson and A. Harsta, Thin Sol. Films 158, 107 (1988).

1-14. N. Kobayashi, Semiconductor World p. 68, July (1991).

1-15. C.M. McConica and K. Krishnami, J. Electrochem. Soc. 133(12), 2542 (1986).

1-16. J.I. Ulacia, F.S. Howell, H. Korner, and Ch. Werner, Appl. Surf. Sci. 38, 370 (1989).

1-17. R. Rosler, J. Mendonca, and M. Rice, J. Vac. Sci. Technol. B6(6), 1721 (1988).

1-18. K. Koller, H.P. Erb, and H. Korner, Appl. Surf. Sci. 53, 54 (1991).

1-19. J. Berthold, and C. Wieczorek, Appl. Surf. Sci. 38, 506 (1989).

1-20. W.L. Guthrie, M. Desai, E.G. Colgan, and R. P. Singh, ULSI-VII Conf. Proc., Materials Res. Soc., Pittsburgh, PA (1992).

1-21. A. Sherman, Jap. J. Appl. Phys. 30, 3553 (1991).

1-22. E.K. Broadbent, J. Vac. Sci. Technol. B5(6), 1661 (1987).

1-23. D. Pramanik, and V. Jain, Sol. St. Technol. p. 97, May (1991).

1-24. W. Sinke, G.P.A. Frijling, and F.W. Saris, Appl. Phys. Lett. 47(5), 471 (1985).

1-25. S. Chatterjee and C.M. McConica, J. Electrochem. Soc. 137(1), 328 (1990).

1-26. C. McConica, S. Chatterjee, and S. Sivaram, 5th Intl.VMIC Conf. Proc., (1988).

1-27. V.V.S. Rana, J. A. Taylor, L.H. Holschwander, in ref. 1-3, p. 187.

1-28. H. Itoh, N. Kaji, T. Watanabe, and H. Okano, Jap. J. Appl. Phys. 30, 1525 (1991).

1-29. U.S. Patent Office, CD-ROM database

1-30. E.K. Broadbent, A.E. Morgan, J.M. DeBlasi, P. van der Putte, B. Coulman, B.J. Burrow, and D.K. Sadana, J. Electrochem. Soc. 133(8), 1715 (1986).

1-31. W.T. Stacy, J. Electrochem. Soc. 132(2), 444 (1985).

1-32. H-C. Wulu, SRC Technical Report No. T90043, (1989).

1-33. C.M. Melliar-Smith, A.C. Adams, R.H. Kaiser, and R.A. Kushner, J. Electrochem. Soc. 121(2), 299 (1974).

1-34. J.R. Creighton, J. Electrochem. Soc. 136, 271 (1989).

# 2

# EXPERIMENTAL PROCEDURES

## 2.1 Introduction

The gas dosing experiments were carried out in a UHV environment. The system was constructed from a Perkin-Elmer 545 Auger chamber with a custom-built sample holder and feed through manipulator. A UTI 100C quadrupole mass spectrometer (QMS) and high-precision repetitive gas dosing capabilities were also added to the system, as described in detail below. Fig. 2-1 shows how the main components of the system were arranged. The sample manipulator was used to rotate the samples between the Auger optics axis, the gas dosing nozzle, and/or the QMS entrance aperture. The gas doser, RGA entrance slit, and focal point of the Ar sputter gun were aligned along the circumferential path of the sample's rotational motion This allowed the use of rotation only for moving the sample to the various positions inside the chamber.

The samples were 1 cm x 2 cm pieces of Si wafers. The samples were brought into the chamber through a load lock system pumped by a Leybold 50 liter turbo pump backed by a Danielson TRIBODYNE two stage oil-less diaphragm pump. This pump combination was able to evacuate the load lock to $< 10^{-5}$ Torr within a few minutes. Fig. 2-2 shows the load lock pressure versus time for a typical pump down cycle. The turbo pump was started at ~ 2 minutes of pumping time where the pumping efficiency suddenly increased. The oil-less backing pump was used to reduce the degree of oil contamination in the vacuum system. The load lock housed a mechanical arm with a pincer grip assembly. The pincer grip was used to hold the samples during transfer between the load lock and the UHV chamber.

Inside the UHV chamber the samples were place into a stainless steel shelf bracket which was part of the sample holder assembly. The assembly, shown in Fig. 2-3 consisted of a boron nitride ceramic block with a stainless steel shelf bracket. A ~ 500 Watt thin film heating element was mounted on the face of the ceramic block as shown and was covered by a thin GRAFOIL

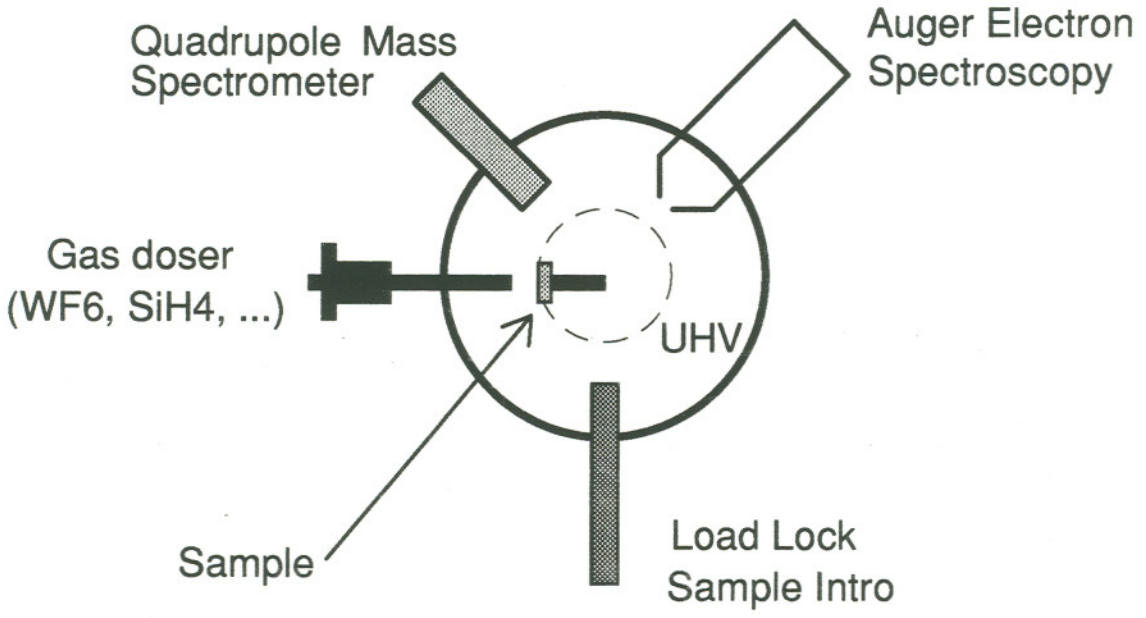


Fig. 2-1. Physical layout of UHV system.

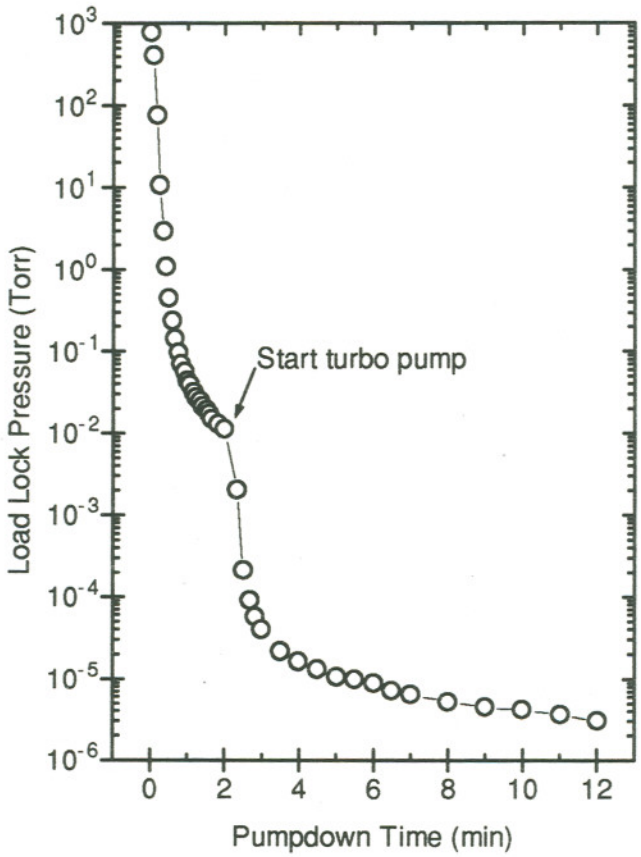


Fig. 2-2. Sample load lock pressure during pump down.

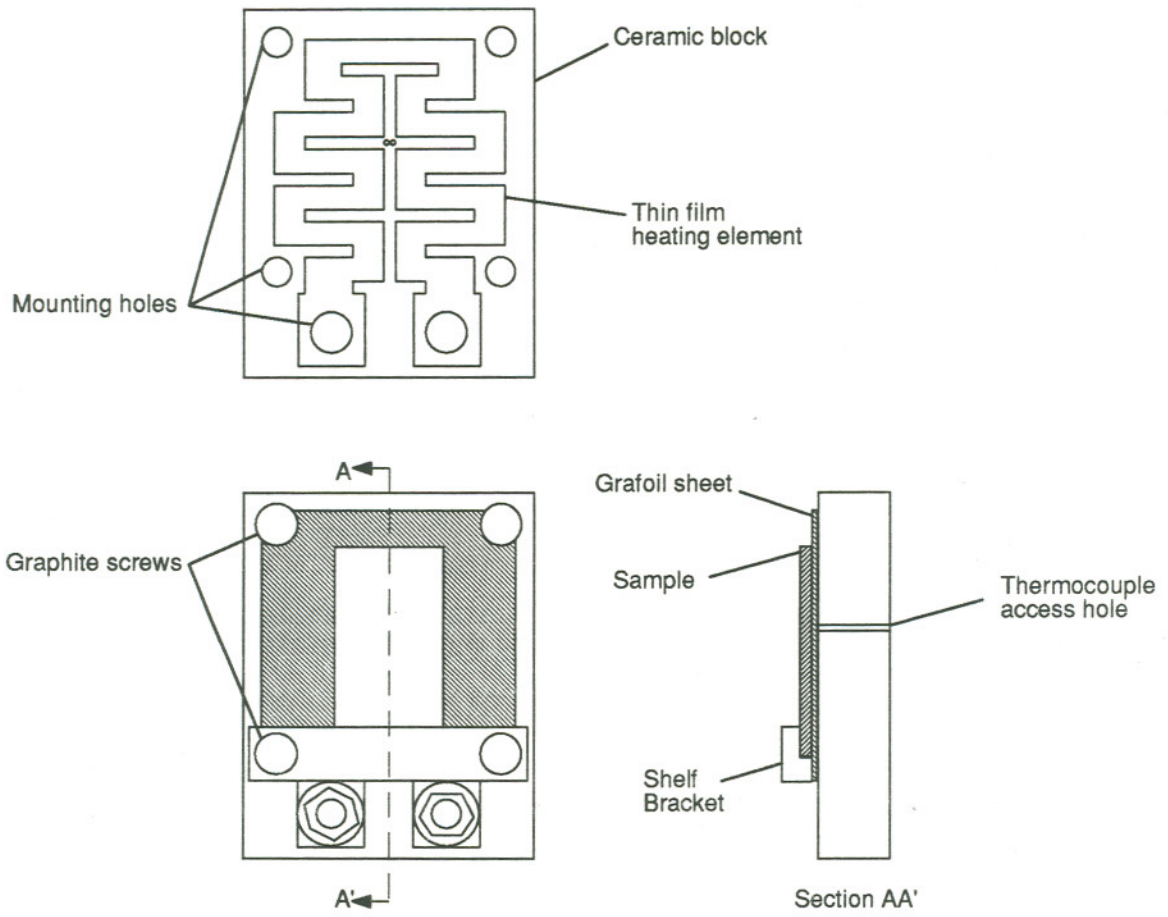


Fig. 2-3. Sample holder and heater assembly. The holder assembly mounts to tantalum rods via the two large mounting holes near the bottom of the ceramic block.

(pyrolytic graphite) sheet to uniformly disperse the heat. The GRAFOIL sheet was held in place by graphite screws at the corners. A type K thermocouple, used to infer the sample temperature, was mounted behind the GRAFOIL sheet at the center of the ceramic block. The assembly was mounted to two tantalum rods, 1/4" diameter near the bottom of the ceramic block that were used for mechanical support as well as electrical contact to the heating element.

### 2.2 Sample heating and temperature measurement

The sample heating element was powered by a Hewlett-Packard 6012A power supply and controlled by a RHK TM310 programmable temperature controller. Heating at ~ 500 Watts, the heater block could be thermally ramped in excess of 10 °C/sec. Control of the sample temperature was not very good because of thermal cycling and drift when such a high ramp rate was used, so for the gas dosing experiments, the thermal ramp rate was kept to 5 °C/sec. The sample temperature versus block temperature was calibrated by direct measurements of the sample surface temperature. A 0.006" type K thermocouple was glued on the surface of a sample, and monitored during a thermal ramp cycle. Fig. 2-4 shows how the sample surface temperature correlated with the block temperature for a typical ramp cycle at 5 °C/sec. The sample surface temperature stabilized at ~ 500 °C within about one minute after the block had reached the set point temperature of 600 °C.

When the samples were heated for the gas dosing experiments a wait time of 1 minute was used before performing the gas exposures in order to ensure confidence in the sample temperatures. Fig. 2-5 shows a temperature correlation plot that was used in determining the heater block set point temperatures. The error bars were determined by considering two different sources of error. The first is an estimate of the uncertainty associated with the sample temperature drifts observed between 1 and 2 minutes after the set point temperature was reached. The second source of error came from scatter in repeatability of sample placement. The sample with the thermocouple was repeated loaded into the shelf bracket then cycled to the set point temperatures. There was some scatter in the sample temperature due to the placement relative to the heater block thermocouple and the random nature of the way it contacted the GRAFOIL sheet. The plot shows that there was a combined uncertainty of about ± 15 °C throughout the temperature range.

### 2.3 Ar sputter cleaning

Argon ion bombardment was used to pre-clean some of the samples prior to gas dosing. The sputter gun was a Perkin Elmer model Φ04-191. The set points of the sputter gun were optimized in terms of sputtering uniformity versus sputter rate, and were determined to be 4 kV

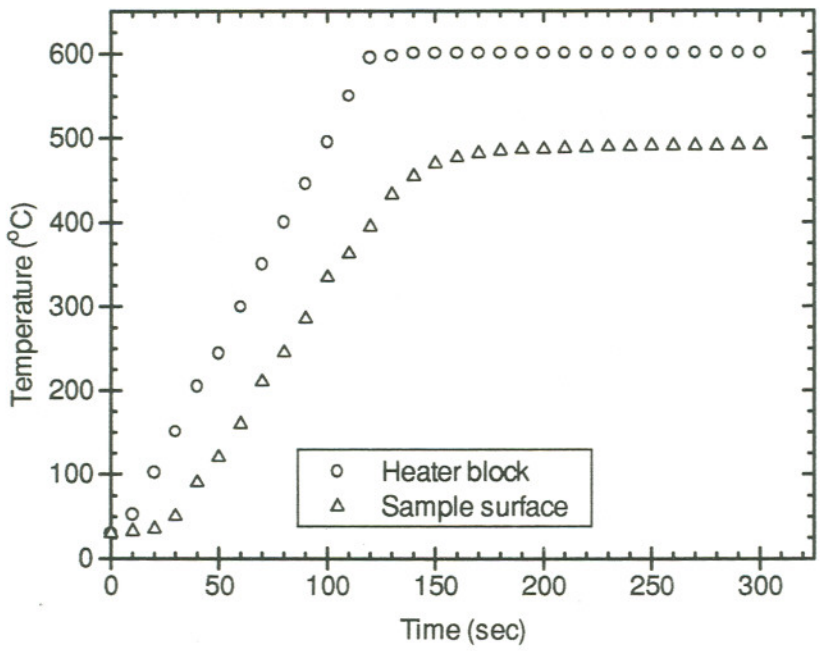


Fig. 2-4. Sample surface temperature and heater block temperature during thermal ramp at a rate of 5 °C/sec to a final block temperature of 600 °C.

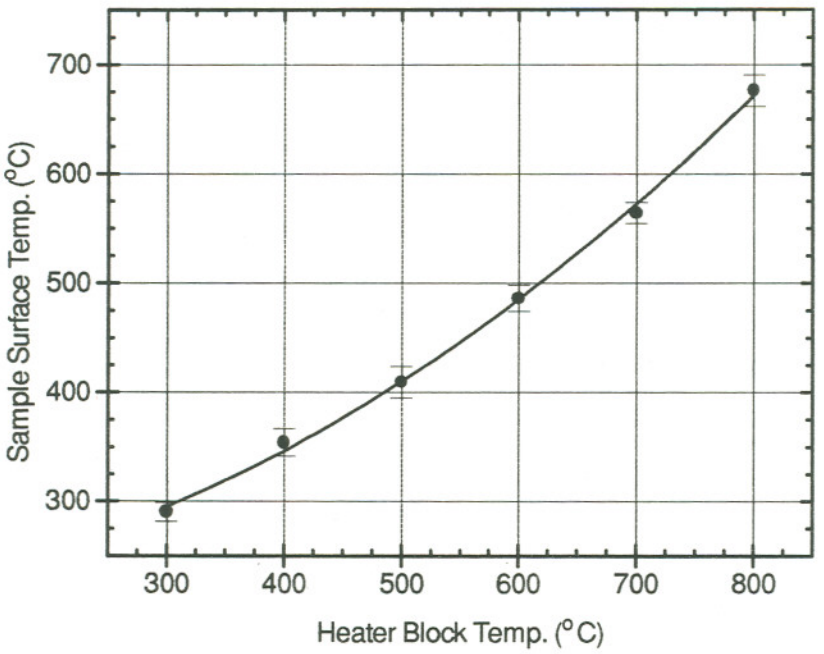


Fig. 2-5. Calibration plot of sample surface temperature versus heater block temperature. Error bars correspond to uncertainties in sample temperature due to thermal drift and repeatablity in sample positioning inside the holder assembly.

accelerating voltage, 25 mA emission current, full scale raster, and at the focus set point labeled "0" as recommended by the manufacturer. These settings gave a uniform sputtering rate of ~ 1 nm/minute across a 1 cm diameter area on the sample surface.

Operation of the sputter gun required the UHV chamber to be pressurized with Ar to a pressure of $5x10^{-5}$ Torr. A high-precision UHV leak valve was used to introduce the Ar into the UHV chamber. System recovery from such a high pressure was slow because the excessive use of Ar saturated the ion pump. It took 20-30 minutes for the chamber pressure to return to the $10^{-9}$ Torr range. In order to avoid long wait times for system recovery, the ion pump was isolated from the chamber during the Ar sputtering by closing the large poppet valve at the bottom of the chamber bell jar. The load lock gate valve was then opened to pump away the excess Ar flowing into the chamber. System recovery time using this technique improved to just a few minutes. The purity of the Ar ambient inside the chamber with this configuration was investigated by monitoring the system pressure with the poppet valve closed and the load lock gate valve open. Fig. 2-6 shows the rise in chamber pressure over 30 minutes in this configuration. For typical sputtering times of 10-20 minutes, the pressure remains in the mid $10^{-9}$ Torr range, which represents a contribution of less than 0.002 % to the $5x10^{-5}$ Torr Ar background.

Even with the high-purity Ar ambient additional measures were needed in order to effectively sputter clean the samples. The sputtering was relatively ineffective when performed with the samples at room temperature. This was probably due to re-deposition of C and O that was sputtered from the sample and sample holder assembly onto the samples. The samples were usually heated to 550 °C during and immediately after the sputter clean to keep the surface as clean as possible. Heating the samples to 550 °C during sputtering and while the system returned to the $1x10^{-9}$ Torr pressure range was effective at preventing the accumulation of C and O on the surface.

## 2.4 Gas dosing procedures and system characterization

### 2.4.1 Hardware description

The gases used for the dosing experiments were high purity electronic grade and housed next to the UHV chamber in a ventilated gas safety cabinet. The gases were stored in 1 liter cylinders and connected to a manifold constructed of 1/8" electropolished stainless steel tubing. The manifold, depicted in Fig. 2-7, was pumped with a Balzer's TPU 100 turbo pump, backed by a Fomblin-based corrosive series rotary vane Alcatel mechanical pump. The gas manifold was connected to a high purity $N_2$ supply for purging the gas lines of reactive gases and also for purging moisture from the lines if they were exposed to atmosphere during system maintenance. The gas cylinders were stainless steel, except for the $WF_6$ cylinder which was MONEL.

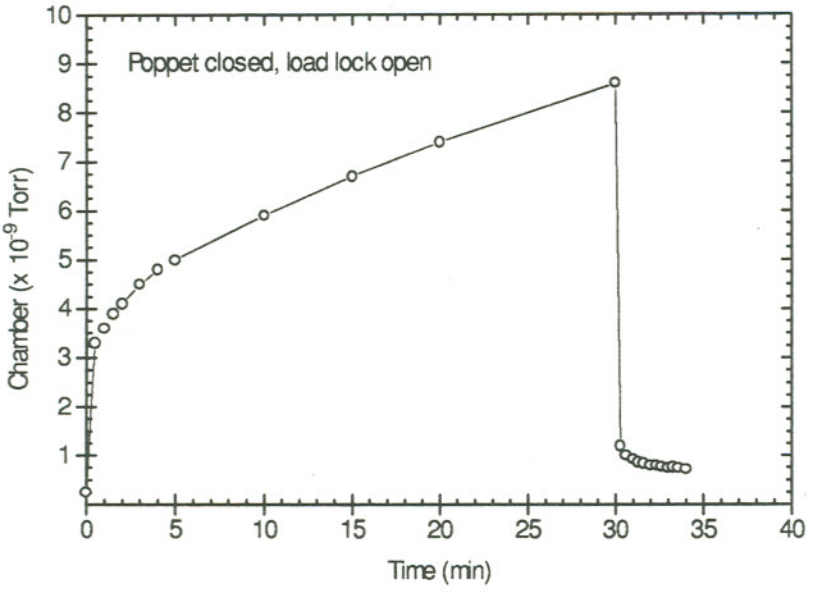


Fig. 2-6. UHV chamber pressure rise with the poppet valve closed and the sample load lock gate valve open. The poppet valve was opened and the load lock gate valve were closed at ~ 30 min.

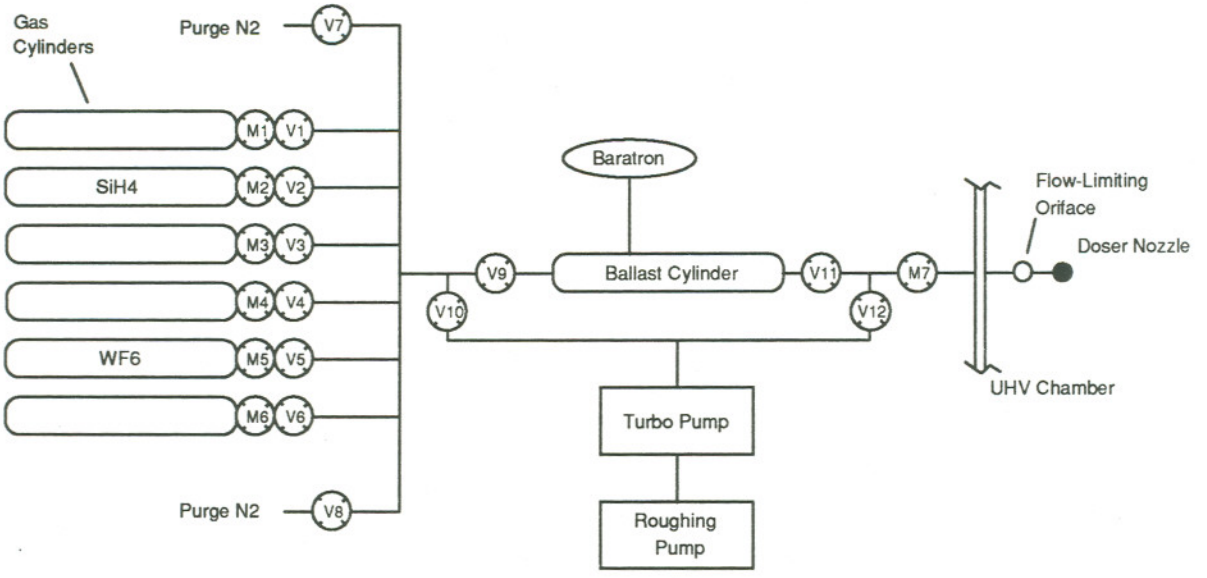


Fig. 2-7. Description of gas manifold hardware components, plumbing, and valves. Valves M1-M7 are mechanical shut-off valves. Valves V1-V12 are electronically-activated pneumatic valves.

Each of the gas cylinders was fitted with a manual valve, labeled M1-M6 in Fig. 2-7. Valves V1-V6 were located adjacent to the manual valves were pneumatically-operated and controlled by push button switches. An interlock selector circuit prohibited more than one of these pneumatic valves to open at one time. The $N_2$ purge gas was controlled by valves V7 and V8. The gas manifold was isolated from the ballast cylinder by valve V9 and the turbo pump by V10. Valves V11 and V12 allowed the gas lines between the ballast and the UHV chamber to be pressurized and/or evacuated. Manual valve M7 was closed when the gas lines had to be extensively purged or vented for repair. The gas line terminated inside the UHV chamber with a pin-hole doser nozzle which is described in Section 2.4.4.

A one liter stainless steel cylinder was used as a gas ballast, i.e. a temporary "constant" pressure gas source. The gas flow rate from the ballast into the UHV chamber was limited by a 94 μm diameter aperture located near the UHV feed-through. The flow rate with this aperture in the gas line was low enough that when the cylinder was charged to about 1 Torr, the pressure, and therefore the gas flow rate, did not change appreciably over a couple minutes of dosing time. Characterization and calibration of gas flow rates are discussed in more detail in Section 2.4.3.

Since $WF_6$ vapor condenses into a liquid at temperatures near 20 °C [1], the temperatures of the $WF_6$ cylinder, ballast cylinder, and all of the tubing were maintained slightly higher than room temperature, ~ 25-30 °C. This reduced of the chance of $WF_6$ condensation inside the manifold system. The cylinders and manifold tubing were wrapped with 5 separate heater tapes and covered with fiberglass insulation. The heater tapes were controlled individually by digital temperature controllers connected to thermocouples mounted in contact with the cylinders and tubing.

### 2.4.2 Dosing procedures

The first step in setting up the system for dosing was to purge the ballast cylinder and all of the gas lines of any residual gases and/or moisture. If the system had recently been used or had been exposed to atmosphere, all of the lines and the ballast were purged with $N_2$ for several minutes. If the system was left under vacuum, the purge step was unnecessary. After the system had been purged, the ballast was filled with the desired gas and the lines were conditioned according to the following check list. These procedures begin with the assumption that the system is in the normal idle state which is defined as: V1-V8 closed, V9-V12 open, M1-M7 closed, pumps on, manifold pressure $< 5 \times 10^{-6}$ Torr.

1. Close V9, V10, and V11.
2. Select appropriate cylinder *X*, by selecting valve V*X* with selector switch
3. Open manual valve M*X* on cylinder.
4. Open pneumatic valve V*X* for 1 second.
5. Close manual valve M*X*.
6. Open V9 momentarily to pressurize ballast, to 1-10 Torr.
7. Open manual valve M7.
8. Close V12.
9. Open V11 for ~ 30 seconds, then close V11 and open V12.

Steps 1-6 prepare the ballast cylinder for the dosing experiments. Steps 7-9 expose the gas lines and doser nozzle to the dosing gas, and constitute a "passivation" treatment. For reactive gases, a transient effect was observed if this treatment was not performed. This conditioning step was performed with the sample facing away from the doser nozzle in order to avoid unwanted exposure to the gas.

The procedures for dosing a sample after steps 1-9 had been completed were simple. With the sample positioned in front of the doser nozzle, valve V12 was closed and valve V11 was opened. Once the dose was completed (typically 10-20 seconds) valve V11 was closed then valve V12 was opened immediately. The wait time for opening valve V12 was made as small as possible in order to keep the gas exposure as precise as possible. Once V12 was opened, the UHV chamber recovered very quickly, i.e. ~ 1/2 sec. If valve V12 was not opened, the gas trapped between V11 and the aperture continued to supply the doser nozzle, creating a long "tail" on the effective gas exposure.

### 2.4.3 Gas flow rates

The gas flow rate into the UHV chamber was controlled by adjusting the ballast pressure. The gas flow rate was calculated from the rate of decrease of the ballast pressure. Fig. 2-8 shows how the ballast pressure changed with time for $WF_6$ and $SiH_4$ gases. The rates of pressure changes at 1 Torr for $WF_6$ and $SiH_4$ were $1.6 \times 10^{-4}$ and $4.8 \times 10^{-4}$ Torr/sec respectively. These numbers were used in the ideal gas equation (Boyle's Law) to calculate the molecular flow rate, *viz.*,

$$\frac{\Delta N}{\Delta t} = \frac{\Delta p}{\Delta t} \cdot \frac{V}{kT} \qquad (2.1)$$

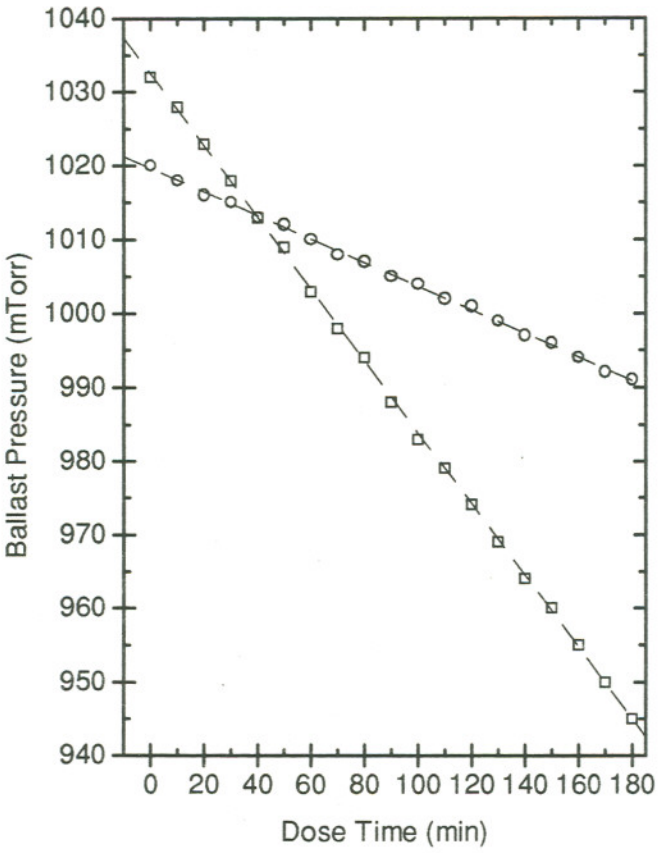


Fig. 2-8. Ballast pressure versus dose time. The dashed lines correspond to linear decay rates of 0.486 and 0.160 mTorr/min for $SiH_4$ and $WF_6$ respectively.

where V is the effective volume and k is the Boltzman constant. The effective ballast volume was estimated to be 1.05 liters and includes ~ 2 ft of 1/8" ID tubing between the ballast cylinder and the flow-limiting aperture. With V = 1.05 liters and 1/kT = $3.1 \times 10^{19}$ molecules/Torr·liter [2], molecular flow rates of $5.2 \times 10^{15}$ and $1.56 \times 10^{16}$ molecules/sec are obtained for $WF_6$ and $SiH_4$.

These flow rates agree well with predictions based on aperture conductance calculations. The flow limiting aperture mentioned in Section 2.4.1 was constructed by drilling a 94 μm diameter hole in a 0.030" thick VCR gasket. The molecular flow conductance of such a structure is given by

$$C = \rho \cdot C_A \tag{2.2}$$

where $C_A$ is the conductance of an ideal circular orifice, and ρ is the transmission factor that is a correction factor for the cylindrical geometry of the aperture. This aperture has a length-to-diameter ratio of 8.1 which gives a transmission factor of 0.18 +/- 0.02 [2]. The conductance of an ideal 94 μm orifice is given by

$$C_A = (8kT / \pi m)^{1/2} \cdot A \tag{2.3}$$
$$= 0.0012 \text{ liter/sec for } WF_6$$
$$= 0.0037 \text{ liter/sec for } SiH_4$$

which gives overall effective conductances of 0.21 and 0.63 $cm^3$/sec for $WF_6$ and $SiH_4$., with *A* being the cross-sectional area of the oriface. The molecular flows through the aperture are thus

$$Q = \Delta p \cdot C = \Delta p \cdot C_A \cdot \rho \tag{2.4}$$
$$= 0.00021 \text{ Torr·liter/sec} = 6.6 \times 10^{15} \text{ mol/sec for } WF_6$$
$$= 0.00063 \text{ Torr·liter/sec} = 2.0 \times 10^{16} \text{ mol/sec for } SiH_4$$

### 2.4.4 Sample positioning and gas exposure rates

The doser nozzle design, based on recommendations by Campbell and Valone [3], approximated a "cosine emitter". The angular distribution of gas flux emitted from such a nozzle approximates a cosine distribution [4]. This is illustrated in Fig. 2-9 which shows how the normalized flux intensity and the total amount of flux intercepted by the sample depend on the angle subtended by the sample from the doser axis, $\theta_{max}$. The flux intensity decreases with a

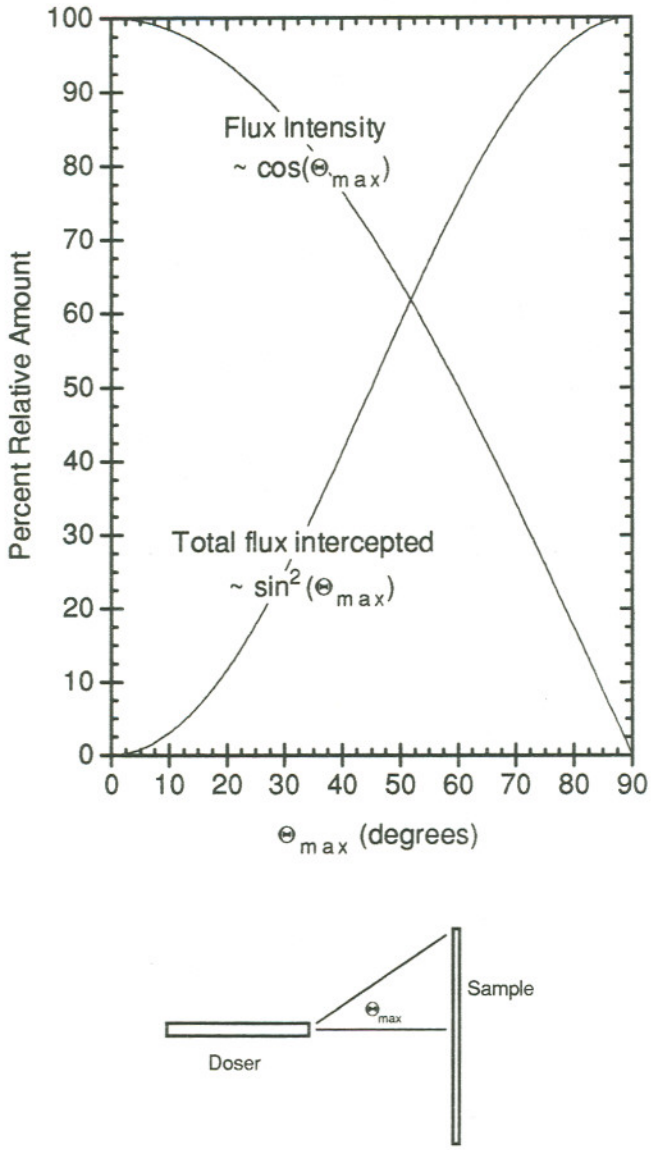


Fig. 2-9. Gas exposure uniformity (relative intensity) and efficiency (total intercepted flux) versus angle subtended by sample ($\theta_{max}$).

cosine dependence while the total intercepted flux increases as sine-squared. There is clearly a trade-off for uniformity versus efficiency in specifying the sample-doser separation. In the dosing experiments for this study the samples were moved between gas doses, so it was desirable to have good uniformity over a fairly large area on the sample ~ 5 mm diameter. A flux uniformity of 90 % over a 5 mm diameter area required a maximum subtended angle of 30° with a sample doser separation of ~ 5 mm. The conditions were used in all of the experiments described in the following chapters.

The gas flux intercepted by the 5 mm diameter area when $\theta_{max} = 30°$ is 25% of the total, or

$$0.25 \cdot 6.6\text{x}10^{15} = 1.65\text{x}10^{15} \text{ mol/sec for } WF_6$$
$$0.25 \cdot 2.0\text{x}10^{16} = 5.00\text{x}10^{15} \text{ mol/sec for } SiH_4$$

Dividing by the 0.196 $cm^2$ area gives the net flux at the sample surface,

$$8.4\text{x}10^{15} \text{ mol/sec}\cdot cm^2 \text{ for } WF_6$$
$$2.5\text{x}10^{16} \text{ mol/sec}\cdot cm^2 \text{ for } SiH_4.$$

It is often useful to describe the gas exposures in units of Langmuirs or $1\text{x}10^{-6}$ Torr · sec. Using a conversion factor of

$$3.1\text{x}10^{19} \frac{\text{molecules} / cm^2}{\text{Torr} \cdot \text{liter}} \qquad (2.5)$$

from Ref. 2-2, gas exposure rates for $WF_6$ and $SiH_4$ were both 0.72 Langmuirs per second of dosing time with the ballast charged to 1 Torr. This is convenient because the gas exposure in terms of Langmuirs is independent of the gas species.

The dosing times were typically less than two minutes which corresponds to ballast pressure changes of 6% for $SiH_4$ and 2% for $WF_6$. Therefore the error in ignoring the drop in ballast pressure would typically be 2-6%. When longer dosing times were used, the ballast was periodically re-charged to 1 Torr in order to avoid larger errors in estimates of total gas exposure on the samples.

## 2.5 Auger Electron Spectroscopy Measurements

Auger electron spectroscopy measurements were performed between gas exposures in order to monitor the surface chemistry of the gas/surface interactions. Auger data were collected with an incident beam energy of 3 keV and a beam current of 10 μA with a spot size of ~ 10 μm at the surface. These settings were chosen in order to maximize the Auger data signal to noise ratio while minimizing the electron beam effects at the surface. Since prolonged exposure to the incident Auger electron beam was found to change the TiN surface chemistry and cause rapid F desorption. As an additional precaution against beam effects, the samples were moved perpendicular to the incident beam between the sequential acquisitions of Auger data in order to expose a fresh area on the sample for each measurement. The influence of instrument settings and electron beam effects on the Auger data are discussed in more detail in Appendix A.

Peak to peak amplitudes of Auger derivative spectra were used to monitor the initial $WF_6$ and $SiH_4$ reactions. Only a qualitative determination of surface F coverage from the Auger data was possible because of electron stimulated desorption of the F. Unless otherwise indicated, the W(NOO) transition at 180 eV and the Si(LVV) transition at 92 eV were used to measure the amounts of these elements deposited on the surface. Independent RBS measurements were used to calibrate the W(NOO) Auger measurements into absolute coverages.

Auger sputter depth profiles were performed on samples ex situ in a Perkin Elmer Φ660 system to study W film composition and thickness. XPS measurements of TiN surfaces before and after sputter cleaning were performed in a Fisons 310F system.

## 2.6 References for Chapter 2

2-1. Encyclopedia of Chemical Technology, Vol. 23, 1982.

2-2. R.W. Carlson, in "Methods of Experimental Physics", *Vol. 14 Vacuum Physics and Technology*, Academic Press, New York, NY, (1979).

2-3. C.T. Campbell and S.M. Valone, J. Vac. Sci. Technol. A(3), 2 (1985).

2-4. H.C.W. Beijerinck and N.F. Verster, J. Appl. Phys. 46, 5 (1975).

# 3

# $WF_6$ REACTIONS WITH Si(100) SURFACES

## 3.1 Introduction

The growth of W films by Si reduction of $WF_6$ is of fundamental interest for selective deposition. In principle it is the simplest process, and has been the subject of intense research and development efforts for several years. As early as 1965, researchers were able to demonstrate the deposition of W onto Si from the reduction of $WF_6$ [1]. During the early and mid-1980's, serious attention was given to exploring the possibilities of using selective CVD W processes in integrated circuit fabrication [2-6]. In spite of the tremendous effort to understand and control this seemingly simple process, a general fundamental description of the process that is applicable to commercially viable systems still does not exist. This is due largely to the extreme sensitivity of the $WF_6$ + Si reaction to surface preparation as well as reactor temperature, pressure, reactor type, and gas flow dynamics.

Some previous experiments have been carried out in UHV systems with precise control over deposition conditions and initial substrate characterization. These experiments have identified and characterized several key aspects of the $WF_6$ + Si reaction. In two independent experiments with different UHV techniques, Yarmoff and McFreely [7] (using in situ XPS) and Jackman and Foord [8] (using TPD and AES/LEED) have shown that $WF_6$ chemisorbs dissociatively on Si surfaces and that F from the dissociated $WF_6$ will inhibit further $WF_6$ adsorption. Both groups also demonstrated that the mechanism for W film growth beyond monolayer coverages is the (thermally activated) diffusion of Si through the W layer where it can combine with surface F to form volatile Si-F compounds. Using a $WF_6$ molecular beam and a residual gas analyzer in a UHV system, Yu, *et.al.* [9] showed that the dominant volatile reaction product changes from $SiF_4$ to $SiF_2$ at ~ 450 °C. Groenon, *et.al.* [10] were able to show explicitly that $SiF_4$ evolution is thermally activated ($E_d$ = 1.6 eV) with the $SiF_3$ + F reaction as the rate-limiting step.

During the fabrication of integrated circuits however, Si wafers are usually cleaned by a wet chemical process which can leave some residual surface O and C on the Si surfaces and the deposition reactions take place in a non-ideal ambient which can complicate the $WF_6$ reduction process. The mechanisms under these conditions are less understood, and in fact a wide variety of phenomena have been reported in past studies of W film deposition by $WF_6$ reduction on HF-cleaned Si substrates. For example, some groups found that the deposition of W ceases after a self-limiting thickness of 10-20 nm is reached [11,12] while others were able to grow films over 100 nm [9,13,14]. Different types of temperature dependence for W deposition have been observed over 200-600 °C including a) Arrhenius, [9,13,15] b) Maximum thickness at ~ 350 °C, [16-18] and c) No temperature dependence at all [11]. Variations in morphology and microstructure of deposited W films have also been reported including "wormhole" formation [19,20], lateral encroachment [21,22], excessive interface roughness [20], and W film porosity [9,14,17,23]. Such a wide range of results is most likely due to differences in initial surface conditions caused by variations in preparation techniques and also to reactor conditions such as cleanliness, temperature, pressure, and flow.

In this study the initial deposition of W on a Si substrate was studied in the presence of O and C contamination layers without the above complications. W films were deposited from $WF_6$ in a UHV environment while monitoring the deposition *in situ* with Auger electron spectroscopy. The growth of thin W films on HF-cleaned Si(100) surfaces is characterized and compared to films deposited on UHV sputter-cleaned Si(100) surfaces. The results show that the initial W deposition rate and film morphology are very sensitive to small amounts of surface oxide contamination. A phenomenological model is presented, which describes how the temperature-dependent film morphology develops, and an extensive review of past results is provided.

### 3.2 Sample Preparation and Characterization

The samples were 1 cm x 2 cm pieces of a p-type, B-doped, 4 Ohm-cm Si(100) wafer. The samples were cleaned with a 10 sec dip in a 5:1 HF solution, rinsed in deionized water, and dried with $N_2$. Once inside the UHV chamber some of the samples received further cleaning by using a 4 keV Ar ion bombardment at 550 °C. The 550 °C temperature was necessary to keep O from re-depositing on the surface. This procedure completely removed any residual contaminants on the surface down to a detectability limit of ~ 0.1 % atomic concentration. The samples cleaned with only the HF process did have some O and C contamination. The thickness of the contamination layer was estimated from the Auger data using the methods outlined in Appendix A to be 0.5 to 1 nm. The set of samples that received only the wet HF clean will be referred to as

"HF-cleaned" and the samples that received a sputter clean in addition to the HF clean will be called "sputter-cleaned".

The uptake of W on the Si(100) surface was monitored by Auger electron spectroscopy measurements taken between $WF_6$ exposures. The first derivative peak-to-peak amplitudes of the Si(LVV) and W(NOO) Auger transitions were used to monitor the growth of the W films. The Auger beam energy was 3 kV with a beam current of ~ 10 μA and the beam diameter was 10 μm at the sample. Since the Auger electron beam was found to cause F desorption from the surface, the Auger data were collected at different locations on the sample for each measurement, and the beam exposure time was kept to a minimum. The electron beam also transmogrified the HF-cleaned sample surfaces by decomposing the Si-O bonds and producing a purely elemental species of Si. This happened within a few seconds of beam exposure time, indicating that the Si-O layer was not very robust.

## 3.3 Results

### 3.3.1 WF6 + Si(100) After Sputter Clean

The initial reaction of $WF_6$ with sputter-cleaned Si(100) surfaces resulted in the immediate deposition of W. Fig. 3-1 shows how the W(NOO) Auger signal increases with $WF_6$ exposure up to ~ 15 L for substrate temperatures of 300, 400, and 550 °C. The initial reaction probability, or sticking coefficient increases with substrate temperature. The dashed lines drawn through the data points correspond to a least squares linear fit of the data and are used as an estimate of the initial $WF_6$ reaction probability. The temperature dependence of the initial reaction probability throughout the 300-550 °C temperature range follows an Arrhenius behavior, as illustrated in Fig. 3-2. Here, the initial reaction probability is plotted versus inverse temperature with a logarithmic ordinate. The average activation energy is 0.16 ± 0.03 eV, given by the slope of the straight line shown in the plot. The reaction probability ranges from about 0.06 at 300 °C up to 0.15 at 550 °C. The error bars are an estimate of the uncertainty in choosing a "best fit" line caused by scatter in the Auger data.

By measuring both the Si(LVV) and the W(NOO) signals, the relative surface concentrations of W and Si could be monitored in situ during film growth. Fig. 3-3 shows the relative surface concentrations at several substrate temperatures after $WF_6$ exposures up to 200 L. The atomic concentrations were calculated by using standard procedures [24] with standard elemental Auger sensitivity factors for the Si(LVV) and W(NOO) peak-to-peak amplitudes [24]. This method is not strictly quantitative, but does serve to illustrate how the relative W and Si concentrations at the surface change as the $WF_6$ reaction proceeds. Initially, the W concentration

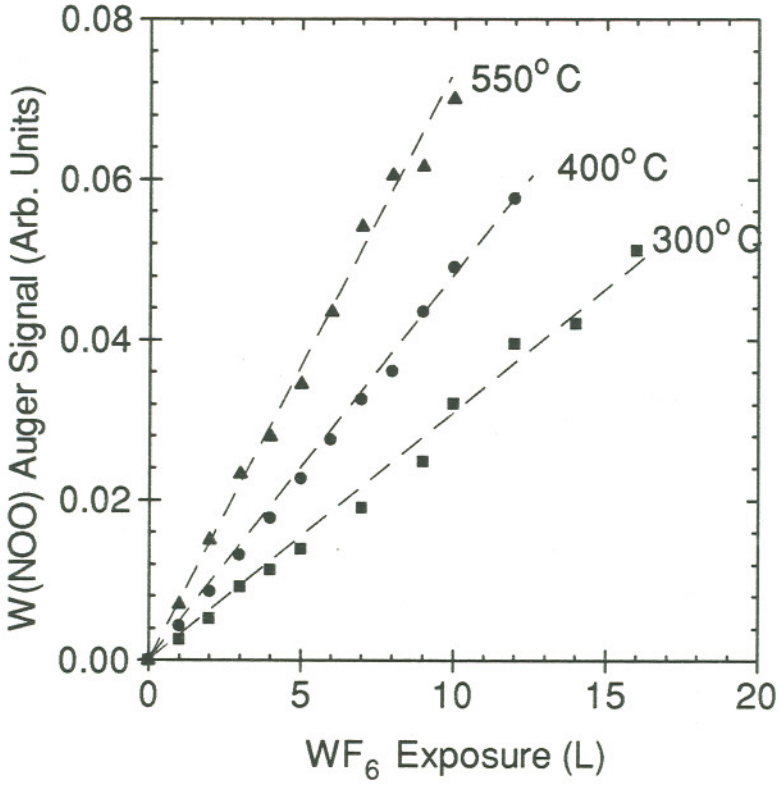


Figure 3.1 W(NOO) Auger signal during $WF_6$ exposure at 300, 400, and 550 °C, for the sputter-cleaned Si(100) surface.

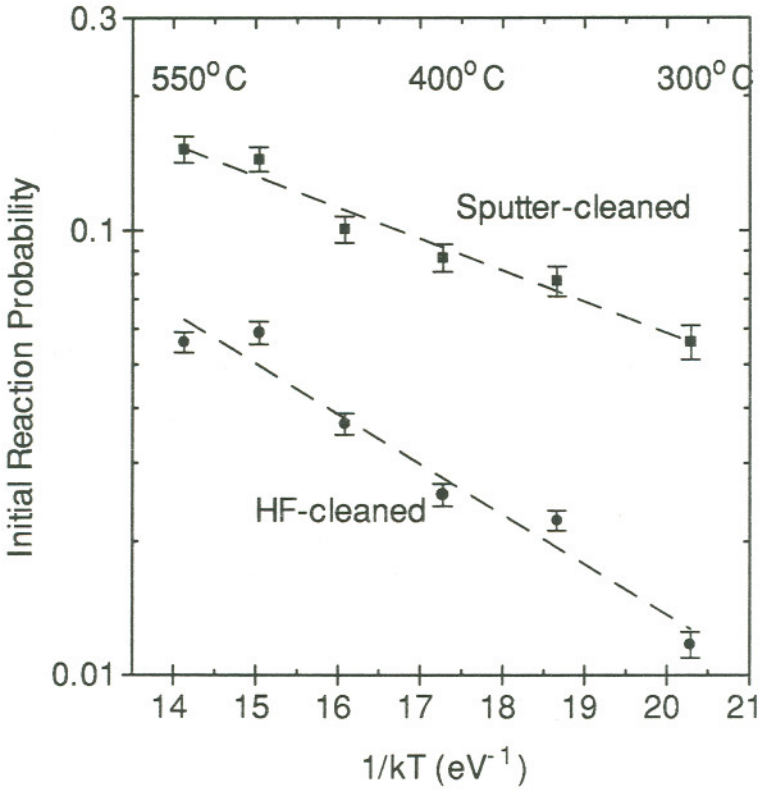


Figure 3.2 Temperature dependence of the initial deposition rate of W on sputter-cleaned Si(100) (square data points), and HF-cleaned Si(100) (round data points).

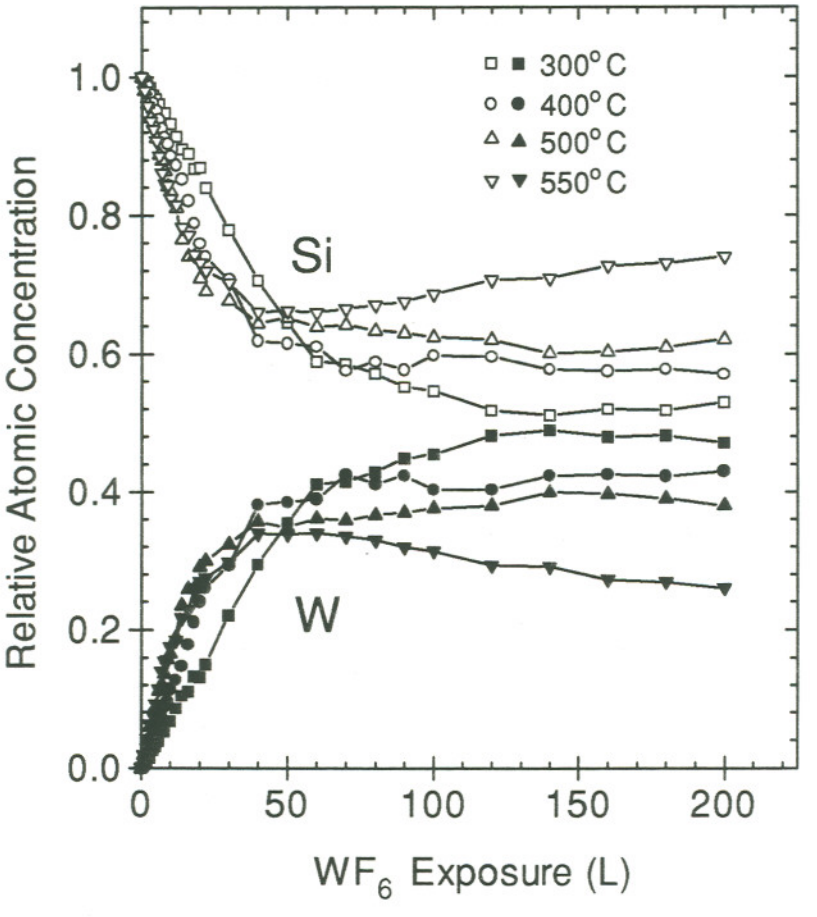


Figure 3.3 Relative surface concentration of W and Si during $WF_6$ exposure on sputter-cleaned Si(100) at 300, 400, 500, and 550 °C. The lines are added to provide visual clarity.

increases and the Si decreases as the depositing W covers the Si substrate. After ~ 50 L the relative concentrations change only slightly. At higher temperatures the Si concentration actually increases with $WF_6$ exposure beyond ~ 50 L, indicating either W island coalescence or some type of diffusion phenomenon. In a later discussion, this effect is attributed to the diffusion of Si through a uniformly deposited W layer. The relative surface concentration of Si increases with temperature from about 50 % at 300 °C up to ~ 75 % for the films grown at 550 °C.

Although the relative changes in the W and Si signals are small for exposures beyond ~ 50 L, Auger sputter depth profiles showed that W deposition continues. For example, between 100 L and 200 L the 400 °C film thickness increased from 3 nm to 12 nm, and the 550 °C film thickness increased from 13 nm to 40 nm. The film thicknesses were obtained by sputter-etching through the deposited film with a focused Ar ion beam to the Si substrate, and then measuring the depth of the sputter crater with a stylus profilometer. Auger data were periodically collected from within the sputter crater to give "in-depth" concentration profiles. Fig. 3-4 shows depth profile data for films grown at 450 °C and 500 °C with 200 L $WF_6$ exposures. The peak-to-peak amplitudes of the Si(LVV) and W(NOO) transitions are plotted versus sputter time, along with O(KLL) and C(KLL). Some O and C were detected at the surface but were at or below the noise level, ~ 1% inside the films. The surface O and C are from adsorbed gases from the lab atmosphere which occurred when the samples were exposed to the lab ambient upon transfer from the reaction chamber to the depth profile chamber. The profiles also indicate that more Si is incorporated into the higher temperature films, and that the amount of Si at the surface is higher than inside the films. All of the profiles through films deposited above 450 °C exhibited these characteristics, which support the premise that Si is diffusing through the growing film and segregating at the outer surface. The diffusion/segregation of the W/Si system has in fact been observed under similar circumstances [7,25], and is believed to be the mechanism responsible for the formation of W silicide by high temperature annealing [7,9,10,25,26].

Both a wet chemical test and X-ray diffraction measurements were used to test for silicide formation within the films. The results suggest W silicide did form in the films deposited at temperatures higher than 450 °C. The wet chemical test consisted of dipping the samples in a 30% $H_2O_2$:$H_2O$ solution maintained at 50 °C. The selectivity of this solution in etching W versus $WSi_2$ was verified using standard, sputter-deposited thin film samples. The etch rate for metallic W was found to be 240 nm/min, while no etching was observed with a $WSi_2$ film after 2 minutes in the solution. The Si(100) samples with films deposited above 450 °C were impervious to a 2 minute dip in the solution, suggesting silicide formation, whereas the films deposited at 450 °C and below readily dissolved within a few seconds which suggests metallic W composition.

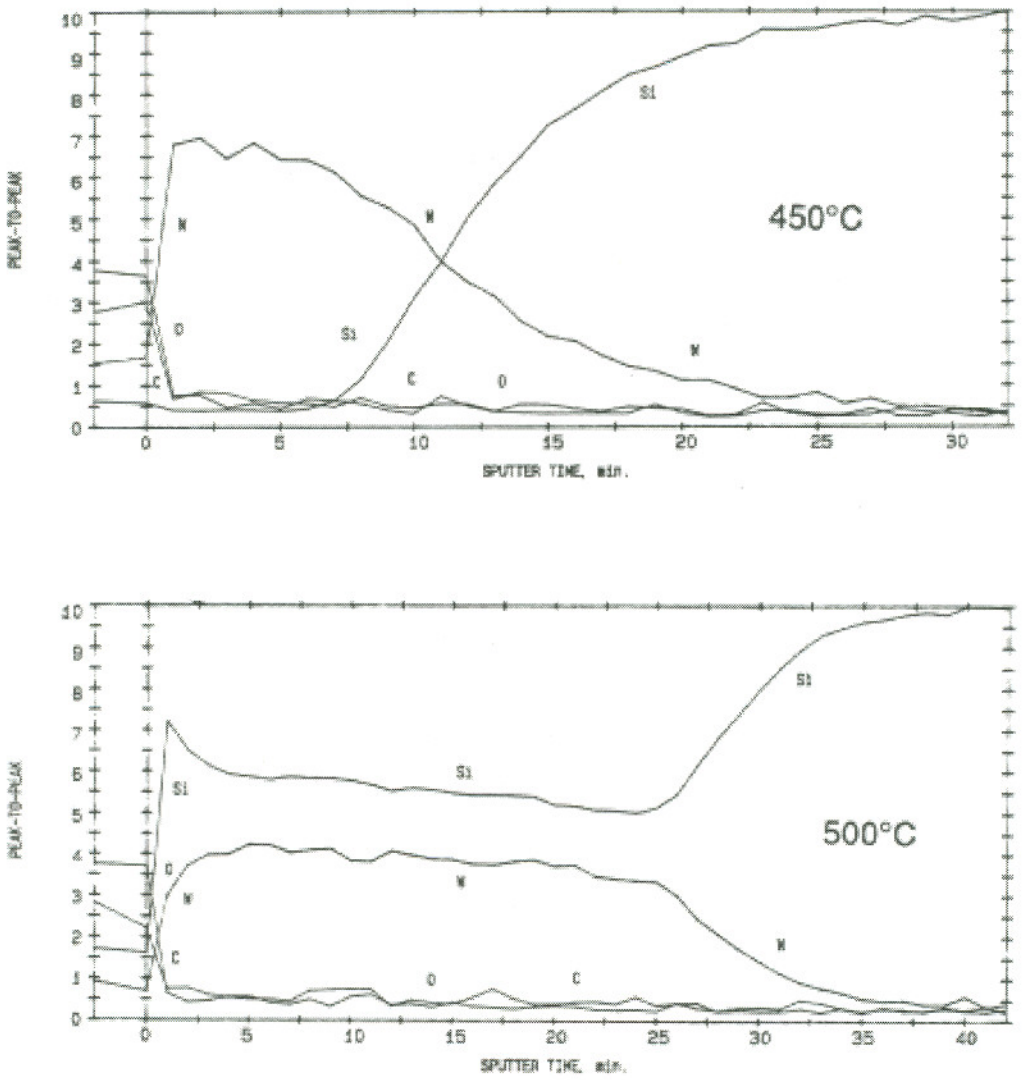


Figure 3.4 Auger sputter depth profile of W films deposited sputter-cleaned Si(100) surfaces from 200 L $WF_6$ exposures at 400 and 550 °C.

X-ray diffraction measurements of the higher temperature films showed some crystallinity that differed from either Si or metallic W. The diffraction peaks were diffuse and weak due to the thin film character of the samples. The peaks do however, line up with some of the higher order planes of $W_5Si_3$ and hexagonal $WSi_2$ crystal structures. This is probably due to the constrained atomic structure of the thin (less than 40 nm) silicide films. The most stable form of W silicide is tetragonal $WSi_2$, but this phase usually forms at higher temperatures than used here. The transition to tet-$WSi_2$, according to calculations by d'Huerle, *et.al.* [27] should begin at $T \approx 550$ °C. Experiments by Murarka, *et.al.* [28] with sputter deposited W films on Si confirmed this prediction and also showed that a pure single phase tet-$WSi_2$ film wasn't actually completed until temperatures in excess of 700 °C were reached. In another more recent study by Cros, *et.al.* [25] with evaporated W films on Si(100) it was demonstrated that Si diffusion through the W begins at $T \sim 400$ °C and that tet-$WSi_2$ does not completely form unless $T \geq 700$ °C. Thus it is not surprising that only the lower temperature less-stable silicide phases were observed here.

SEM images of the films deposited on the sputter-cleaned samples after 200 L showed a smooth and uniform morphology on a 100 nm length scale when imaged at 37,000× magnification. The uniform morphology was observed with all of the films deposited on the sputter cleaned samples. The uniform morphology discounts the possibility of large scale porosity or W island coalescence, and solidifies the theory that Si is diffusing through the growing film. Thus the observed Auger data in Fig. 3-3 is associated with grain boundary diffusion of Si, instead of island formation. It is generally accepted [7,10,13,26,29,30] that the mechanism which sustains W deposition from the $WF_6$ + Si reaction beyond a few monolayers is the diffusion of Si through the W film. The Si atoms can then readily combine with F to form volatile $SiF_x$ species which desorb, creating more adsorption sites for the $WF_6$ . The uptake data in Fig. 3-1, the depth profile data in Fig. 3-4, and the SEM images are all consistent with these ideas.

### 3.3.2 $WF_6$ + Si(100) After HF Clean

When the Si(100) substrates were cleaned with only the wet HF process, the $WF_6$ reaction was markedly different. Fig. 3-5 shows the W(NOO) Auger amplitudes plotted versus $WF_6$ exposure for substrate temperatures of 300, 400, and 550 °C. The initial reaction probability can again be approximated by a linear fit to the data, but the lines do not intersect the origin. This indicates an induction, or incubation period during which W deposition was not observed. The induction period appears to decrease with increasing temperature, and is discussed in more detail below. The initial reaction probability (after the induction period) is more sensitive to temperature than for the sputter-cleaned case, as evident in Fig. 3-2 which compares the initial $WF_6$ reaction

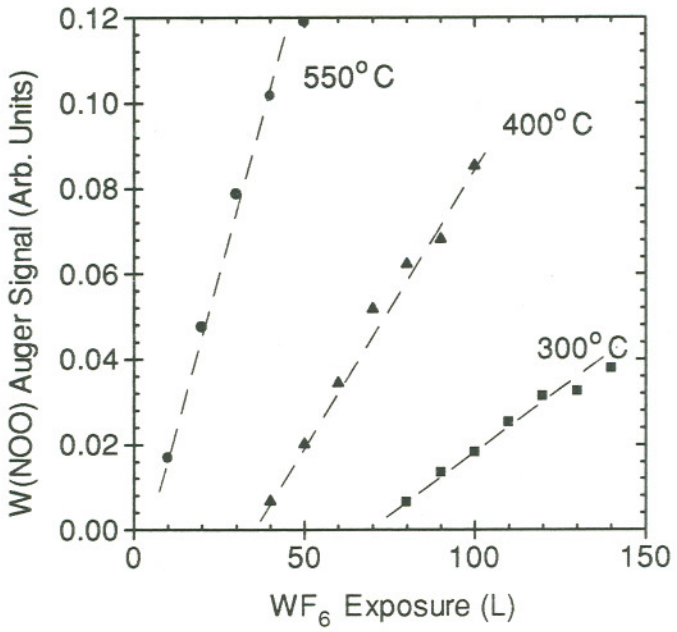


Figure 3.5 W(NOO) Auger signal during $WF_6$ exposure at 300, 400, and 550 °C on the HF-cleaned Si(100) surface.

probabilities for the two sets of samples. The reaction probabilities are generally lower on the HF-cleaned samples, ranging from ~ 0.003 at 300 °C up to ~ 0.2 at 550 °C. An Arrhenius fit to the data gives an average activation energy of 0.26 ± 0.05 eV.

Fig. 3-6 shows the relative concentrations of W and Si on the surface for the HF-cleaned samples during $WF_6$ exposures up to 200 L. The results for the 500 °C and 550 °C films are similar to the corresponding data in Fig. 3, in that the relative concentrations do not change much after ~ 50 L. The 300 °C and 400 °C results suggest that less W is deposited on the HF-cleaned substrates at lower temperatures. This was confirmed by film thickness measurements *via* sputter depth profiles after 200 L exposures.

Fig. 3-7 shows Auger depth profile data results for the 450, 500, and 550 °C films. The amount of Si incorporated in the films increases with temperature, as well as the film thickness (inferred by the time required to sputter through the films). The O and C were again at the noise level in the films which was typically ~ 1 % atomic concentration. The relative amount of Si incorporation was less than for the sputter cleaned samples, *cf.* Fig. 3-4, although the higher Si concentration at the surface is again observed.

The peroxide wet etch and XRD measurements were also used to test for silicide formation on the HF-cleaned samples. The wet etch test results again suggested silicide formation for deposition temperatures greater than 450 °C. The XRD results were essentially the same as the results with the sputter cleaned substrates even though the depth profiles showed lower concentrations of Si in the films. Weak diffraction peaks were observed for the lower temperature silicide phases, $W_5Si_3$ and hex-$WSi_2$.

SEM images at 37,000× of the films grown at 450 °C and below showed a morphology indistinguishable from the set of films grown on the sputter cleaned substrates. The films grown at 500 °C and above, however, showed a temperature dependent porous film structure. Fig. 3-8 compares SEM images for the films deposited on HF-cleaned samples at 450, 500, and 550 °C. The black areas in the higher temperature film images correspond to gaps or pores in the deposited W films. The pore size increases with temperature from ~ 100 nm in diameter at 500 °C up to 300 nm for the 550 °C film.

The initial period during the $WF_6$ exposures for which no W deposition was observed was referred to above as the induction period. The length of this period (in terms of $WF_6$ exposure time, or total exposure) increases with decreasing temperature. Fig. 3-9 shows explicitly how the induction period varies with temperature. The length of the induction period is displayed in units of seconds at 2.5 x $10^{16}$ molecules/sec·cm$^2$., and was estimated by extrapolating the lines shown in Fig. 3-5 through the horizontal axis. Over the temperature range studied, the induction period

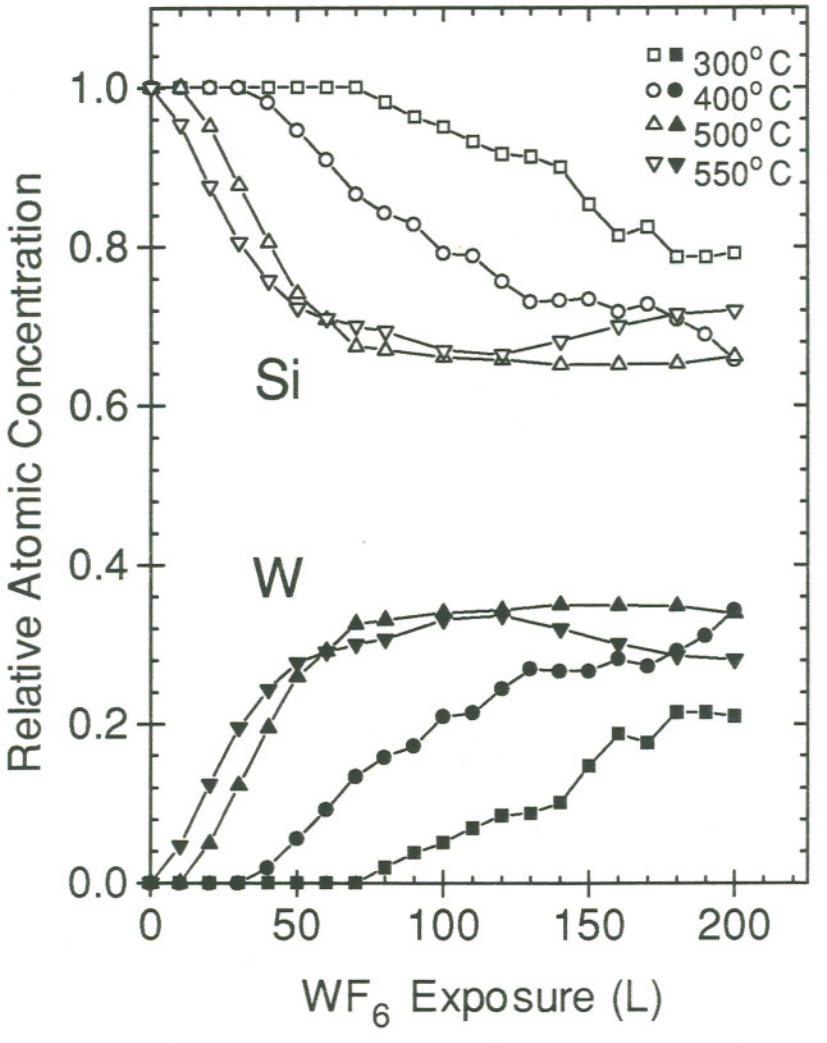


Figure 3.6 Relative surface concentration of W and Si during $WF_6$ exposure on HF-cleaned Si(100). The lines are added to provide visual clarity.

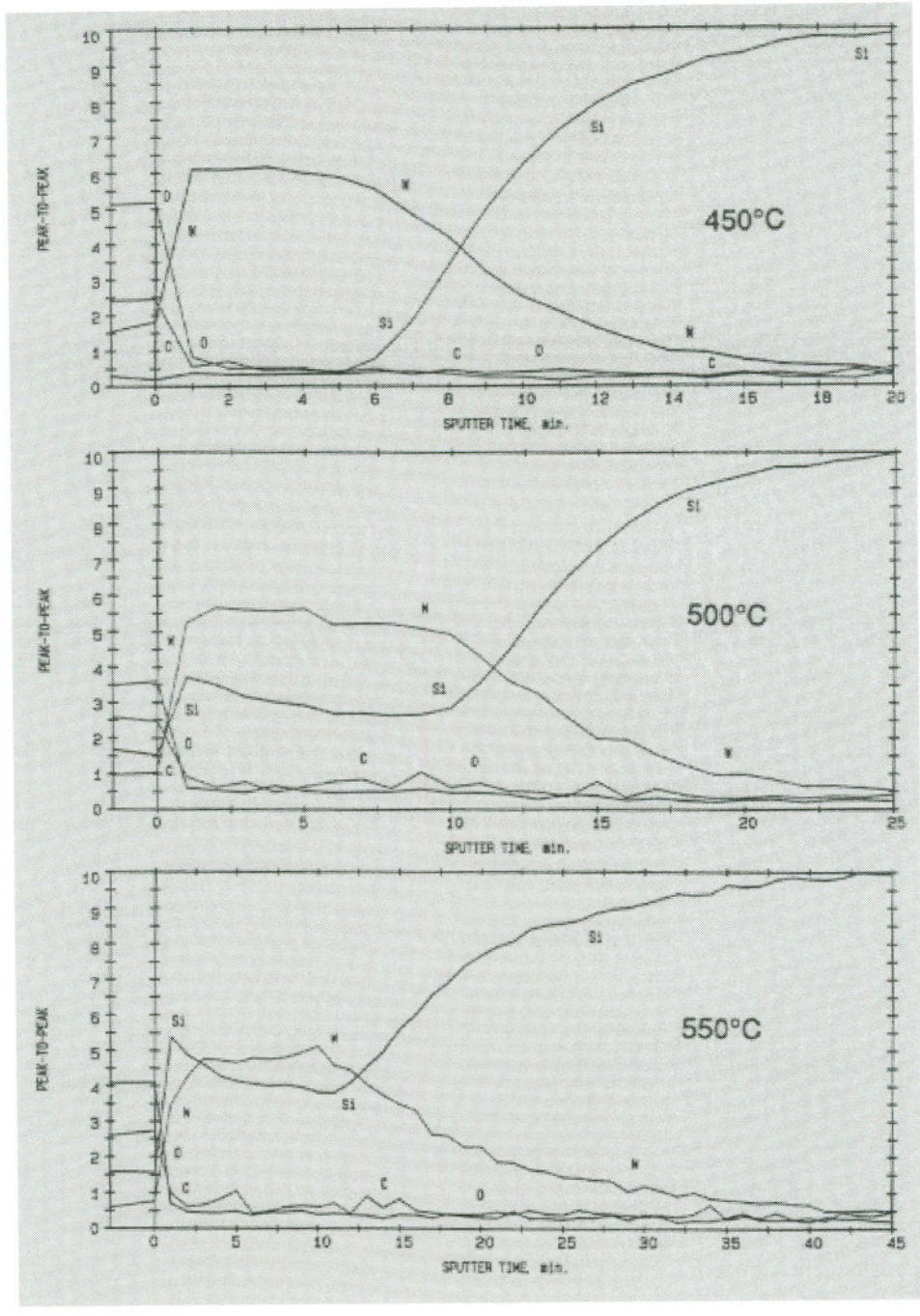


Figure 3.7 Auger sputter depth profiles for W films deposited on HF-cleaned Si(100) surfaces from 200 L $WF_6$ exposures at 450, 500, and 550 °C.

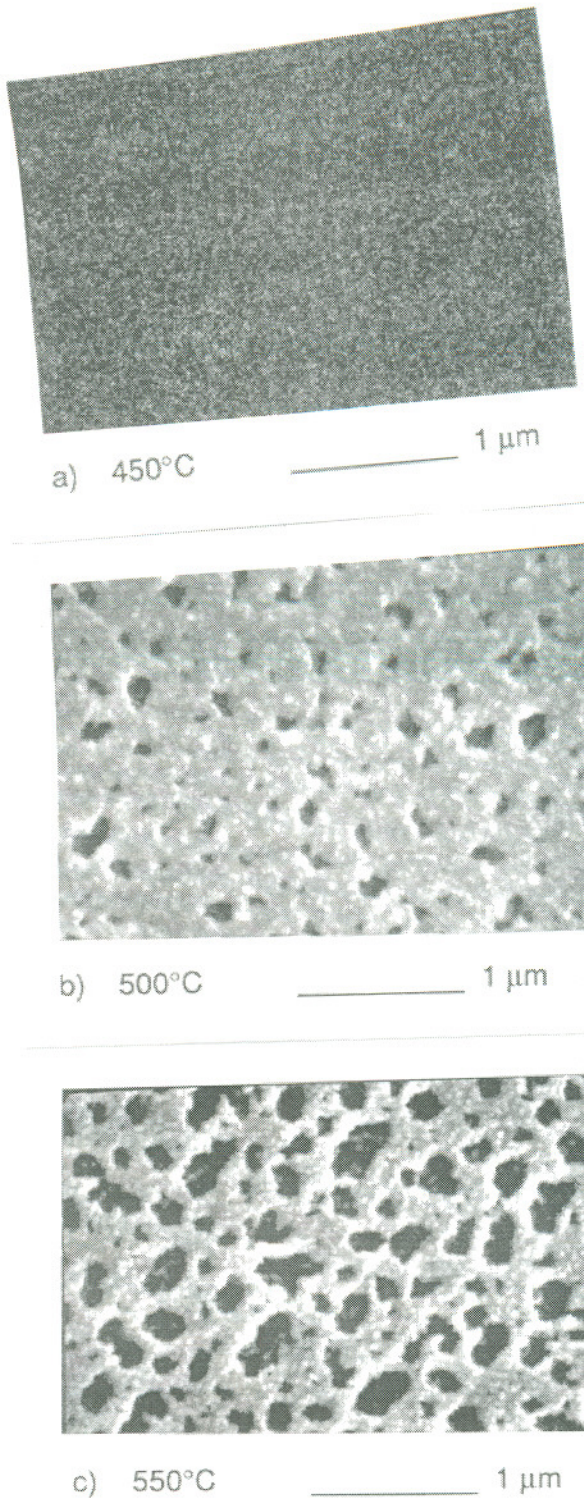


Figure 3.8 SEM images of W films deposited on HF-cleaned Si(100) at a) 450 °C, b) 500 °C, and c) 550 °C. A 1 μm line is shown in the figure for length reference.

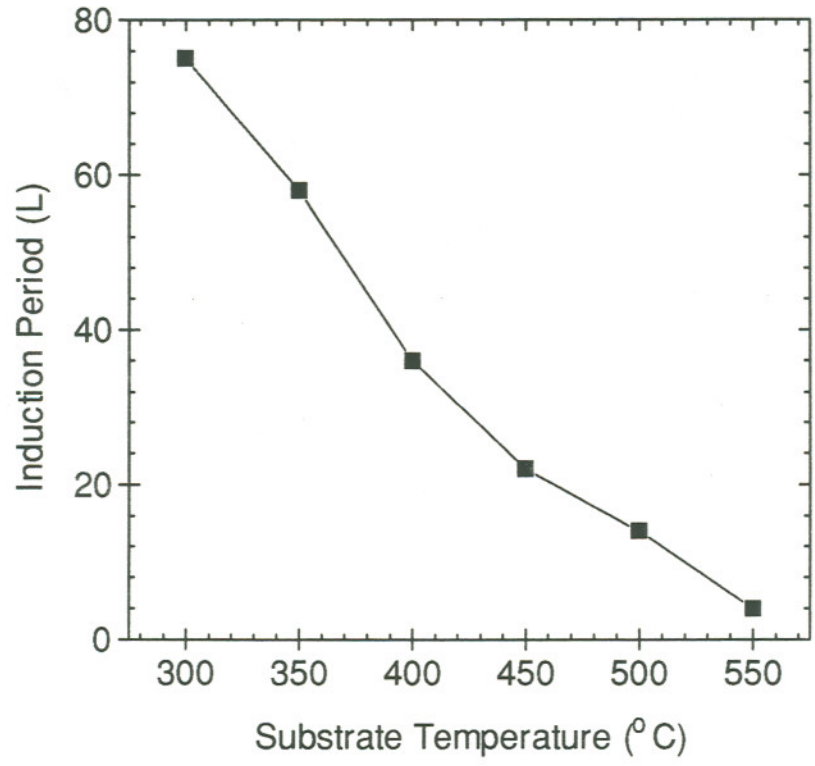


Figure 3.9 Length of induction period in Langmuirs versus substrate temperature.

ranges from ~ 7 sec at 550 °C up to ~ 104 sec at 300 °C.

In order to gain a better understanding of what occurs during the induction period, two additional samples were prepared, each with different amounts of surface O and C. These samples did not receive any HF treatment, but the contamination layers were partially removed with *in vacuo* sputter cleaning. The samples were maintained at 550 °C during the 4 keV Ar ion sputter, and a low beam current was used in order to decrease the sputtering yield. Fig. 3-10 shows the relative atomic concentrations of C and O on these two samples after sputtering, compared to a typical HF-cleaned sample. Sample #1 has less C and O than the HF-cleaned sample, and Sample #2 has less C, but more O. These two samples were then heated to 450 °C and exposed to $WF_6$ . The W(NOO) Auger signals are plotted against $WF_6$ exposure in Fig. 3-10 along with data for the HF-cleaned and fully-sputter-cleaned sample exposures. An induction period is observed for all of the samples with surface contamination, and increases with the amount of O. Since the induction period is seen for these samples without the HF clean, it cannot be attributed to surface H or F left over from the clean. The induction period does not track with the amount of C, indicating that C does not have a direct influence. For Sample #2 which had the highest initial oxygen level, the induction period is ~ 60 L. A distinguishing feature of the data for this sample is that the uptake of W begins very slowly, then gradually increases to its maximum rate near 100 L. To further illustrate this point, Fig. 3-11 shows the peak-to peak amplitudes of the W(NOO), O(KLL), and Si(LVV) transitions as Sample #2 is exposed to $WF_6$ at 450 °C. Up to 60 L both the O and the Si signals slowly decrease and the W signal increases very slowly. After ~ 60 L, the W signal begins to rise more rapidly, the Si signal begins to increase, and the O signal drops very quickly.

The interpretation of these features is that induction period corresponds to a period of etching of the oxide layer. Once the Si substrate is uncovered by the etching, Si diffusion begins along with rapid W deposition. This theory is developed more fully in the discussions below.

## 3.4 Discussion

### 3.4.1 Reaction Kinetics and Pathways

In previous studies, Yu *et.al.* [31] measured a reaction probability of 0.3 ± 0.04 for the $WF_6$ + Si(100) reaction, but did not observe any temperature dependence over 200-700 °C. The Si(100) surfaces were cleaned by Ar sputtering and annealed to 1000 °C prior to $WF_6$ exposure. The experimental apparatus consisted of a UHV chamber with a pulsed molecular beam of $WF_6$ incident at 45° on the sample, and a differentially-pumped quadrupole RGA used to detect the gas

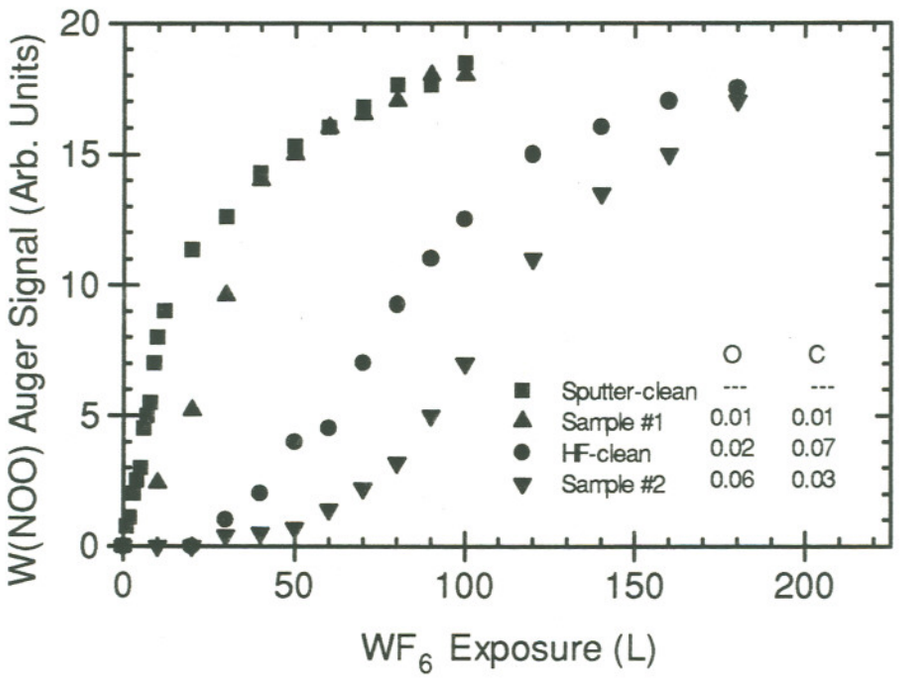


Figure 3.10 W(NOO) Auger signal during $WF_6$ exposure at 450 °C for samples with different methods of cleaning. The relative atomic concentrations of contaminants are shown in the legend.

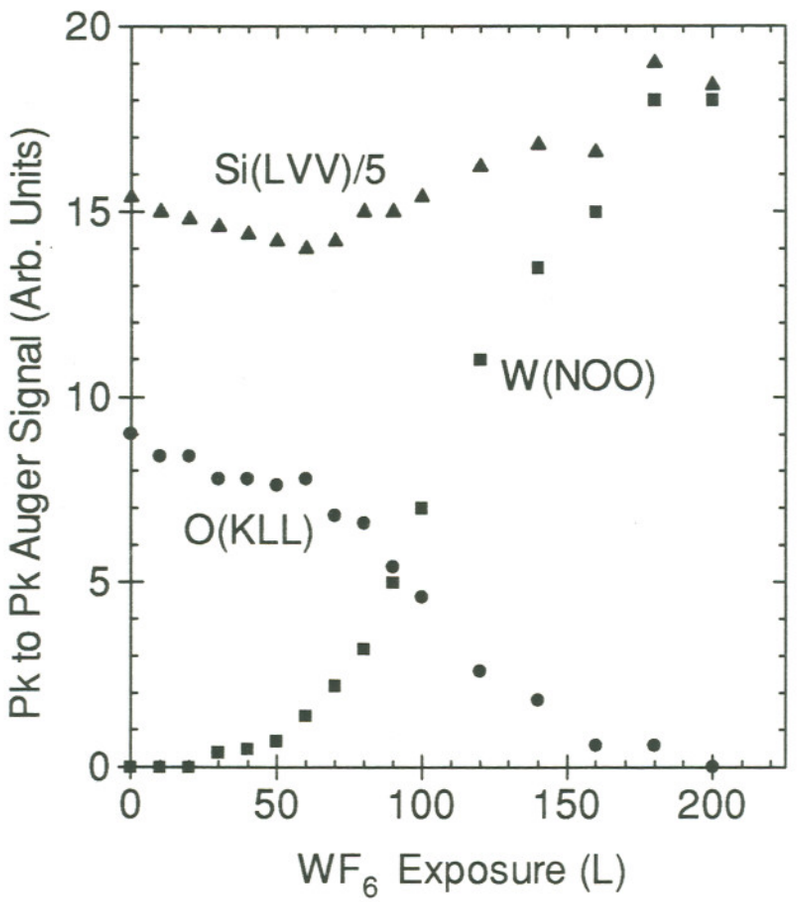


Figure 3.11 Peak to peak Auger amplitudes of W(NOO), Si(LVV), and O(KLL) during $WF_6$ exposure at 450 °C for Sample #2.

$$s_o = \frac{r_{sat} - r_o}{r_{sat}} \qquad (3.1)$$

where $r_o$ and $r_{sat}$ are the reflected $W^+$ signals from the clean and "saturated" Si(100) surfaces respectively. A value for $r_{sat}$ was obtained with the substrate at room temperature where a saturation effect was observed in that the reflected $W^+$ signal approached a constant value.

If the initial Si(100) surfaces were the same, then this method should give the same results as the methods used in this work. The only difference in sample preparation was the 1000 °C anneal used by Yu. This higher temperature anneal would have tended to passivate the surface which in turn would have given a lower reaction probability. In fact, they observed a stable p(2x1) surface structure with LEED after the anneal, indicating surface atomic re-arrangement, akin to lowering the surface reactivity. Within the estimated uncertainties in the $s_o$ values, Yu's results are are consistent with the values found in this study.

The lack of temperature dependence in Yu's results could have been another consequence of the high temperature anneal. The Arrhenius temperature dependence observed in Fig. 3-2 is an indication of an energy barrier for the adsorption process, *cf.* Chapter 4. The 1000 °C anneal performed by Yu, in addition to passivating the surface, could have eliminated the reaction pathway that was responsible for the activation barrier.

The observation of lower $s_o$ values obtained in this work with the HF-cleaned substrates would be expected since these surfaces were covered with residual O and C. The O would passivate the surface by chemically bonding to the Si atoms, reducing the number of adsorption sites. Although some UHV studies of the $WF_6$ + Si reaction in the presence of surface O have been carried out [32], the work in this thesis represents the first time measurements of initial reaction probabilities on (O and C contaminated) surfaces prepared ex situ.

The activation energies calculated from the Auger data are average effective values for the initial $WF_6$ reaction probabilities, $s_o$. These results are unique in that they also represent attempts at determining the activation energies with measurements taken "during" film growth. Previous attempts have been based on post deposition W film thickness measurements and a large variety of results have been published using this method. For example, Kuiper, *et.al.* [13] determined an activation energy of 0.33 eV, and Yu, *et.al.* [9] reported 0.48 eV, both using RBS measurements to estimate film thicknesses for substrate temperatures 200-700 °C. In both cases the reaction probability, or reaction rate was assumed to be proportional to the film thickness. Using an *in situ* plasma clean, Wood [33] determined an activation energy of 0.16 eV for the Si reduction of $WF_6$ . Weight gain measurements were used to estimate amounts of W deposited, and again a constant

reaction probability was assumed. In these studies the films were generally 10-100 nm thick, and deposited in standard or near-standard LPCVD reactors without precise characterization of the initial surface conditions. Except for Wood, they all used some variant of a wet (typically HF-based) clean prior to W film growth. The variations in activation energies are probably due to differences in initial surface conditions. Also, any variations with extrinsic parameters, *e.g.* pressure or temperature, which are often not precisely controlled in commercial-type reactors could have contributed to the differences in values for $E_a$.

The value of 0.16 eV obtained in this work agrees well with the result of Wood [33] who had also used an *in situ* clean prior to deposition. All the other studies which used only wet HF cleans gave higher $E_a$ values, as did this work when the samples were cleaned with only the wet HF process. The apparent trend is that higher $E_a$ values are found (1) when *ex situ* cleans are used and (2) when the $WF_6$ reaction probabilities are estimated from W film thickness measurements.

Surface oxidation would be present to some degree when the cleans are used, as shown by the results of this work. This would tend to create an energy barrier to the adsorption process and give a higher effective activation energy. Some observations of the effects of surface oxide have been reported. For example, surface oxide was shown to interfere with the dissociation of $WF_6$ [32]. The oxide layer is also known to act as a diffusion barrier to Si [26,34,35], which would also tend to cause a higher activation energy. Electron transfer from the substrate, which is believed to be necessary for $WF_6$ dissociation [36], would be inhibited and the overall reactivity would be much less owing to the passivating effect of a oxide layer.

When the activation energies are obtained using film thickness measurements additional mechanisms must be considered, *viz.* surface and bulk diffusion of different species, [7,29,30] enthalpies of compound formation and dissociation [37,38], and desorption of volatile reaction products [8,10,31]. Any one of these mechanisms can rate-limit the $WF_6$ reaction when the W layer is more than a monolayer thick. The rate-limiting step is also subject to change during film growth and the overall reaction rate is subject to change with film thickness as evidenced in this study by the depth profile film thickness measurements mentioned in Section 3.3.1. Small variations in extrinsic parameters such as temperature and pressure can also influence the reaction pathways and rates. In fact Yu, *et.al.* [9] have observed a transition in the dominant volatile reaction product from $SiF_4$ to $SiF_2$ at temperatures ~ 450 °C. Activation energies for diffusion, and desorption are typically 1 eV or greater [10,27,30]. Thus if these phenomena were contributing to limit the $WF_6$ reaction rate, the activation energy should increase, which is the observed trend.

The magnitudes of the activation energies measured in this study, 0.16 and 0.26 eV, are quite small in comparison to values predicted for some of the more common rate-limiting mechanisms. For example, a likely rate limiting step would be $WF_6$ (or $WF_x$ with $x \leq 6$) dissociation. Previous studies have suggested that at $T < 150$ K, the deposition of W on Si(100) from $WF_6$ is in fact rate limited by the dissociation of adsorbed $WF_6$ molecules [8,39]. The bond dissociation energy however for each of the $WF_x \rightarrow WF_{x-1} + F$ reactions is about 120 kcal/mole [37], or about 5 eV/molecule, which is much too large to correspond to the activation barriers measured in this study. In general it is very difficult to assign a particular physical or chemical mechanism to an empirically-derived activation barrier based simply on feasibility and order-of-magnitude estimates. There could be contributions from several individual phenomena producing the overall effects that were be measured by the techniques used in this study. It can be stated unequivocally however that the barrier is not simply due alone to $WF_x$ dissociation, surface F diffusion, grain boundary diffusion of Si, or $SiF_x$ thermal desorption.

### 3.4.2 Porous morphology and induction period

The porous film structures observed on the HF-cleaned substrates illustrate how sensitive the $WF_6$ + Si reaction can be to surface preparation. Porous film structures have previously been observed on Si surfaces throughout the 200 to 700 °C temperature range for films grown by $WF_6$ + Si reactions in commercial LPCVD reactors, and a variety of film morphologies have been reported. For example Park, *et.al* [17] observed with TEM the growth of porous films at 300 °C on HF-cleaned Si with pore sizes 2-3 nm in diameter. By comparing TEM and RBS measurements, Green et.al. [40] showed that W films deposited on HF-cleaned Si are less dense than bulk metallic tungsten and attributed this to small scale discontinuities or "microporosity" in the deposited films. Morosanu and Soltuz [15] reported "hole type" defects at higher deposition temperatures though they did not specify the sizes or densities of the defects. Wong, *et.al.* [14] also observed W films from the $WF_6$ + Si reaction with what they call "microchannel" defects. In addition to porous film structures some other rather striking morphological features have been observed with $WF_6$ + Si reactions including worm-hole formation, lateral encroachment, and excessive interface roughness [20]. These features will not be addressed any further in this thesis, but many general summaries and theories can be found in the literature [2,3,20,41].

The key to porous film growth, as presented in this thesis is the presence of an initial oxide layer on the Si surface. The model, which is shown in Fig. 3-12 has been adapted from comments made by Broadbent and Ramiller [11], and Holleman, *et.al.* [42]. The oxide layers encountered in this work were very thin and probably non-stoichiometric, *i.e.* $SiO_2$ with $x < 2$. The induction

period as described in Fig. 3-12, is attributed to an initial etching reaction, which is most likely [43] *via*

$$2WF_6 + 3SiO_x \rightarrow 2WO_y + 3SiF_4 \qquad (3.2)$$

where $x \leq 2$ and $y \leq 3$. This proposition is consistent with a study by Busta and Tang, [21] in which they propose that $WF_6$ reacts with and decomposes an initial $SiO_x$ contamination layer, and a W-O compound forms. They were not able to identify the W-O compound by XPS analysis, but when their initial oxide layer was greater than 2 nm they were able to observe the formation of β-W ($W_3O$) with X-ray diffraction. In a more recent study, Park, *et.al.* [17] reported the formation of $WO_3$ at the W/Si interface for HF-cleaned Si, using XPS. It is also conceivable that etching may occur during the induction period *via* formation of volatile W-O or W-O-F compounds. Both $WO_3$ and $WOF_4$ are known to be volatile [44,45]. Thermodynamic calculations and past thermal desorption experiments however, suggest that for this temperature range (300 to 550 °C) the formation of volatile W compounds is not very likely. Carlsson and Boman [43] have investigated all reasonably possible $WF_6$ + Si and $WF_6$ + $SiO_2$ reactions based on thermodynamic equilibria calculations. Their results show that the most energetically-favorable gas phase product of the reaction with $SiO_2$ is $SiF_4$. Volatile W compounds such as $WO_2F_2$ or $WOF_4$ are less likely by several orders of magnitude. Solid phase $WO_3$ is the most favorable reaction product containing W. With temperature programmed desorption experiments studying $WF_6$ + Si reactions with thin initial oxide layers, Raupp and Hindman [39] looked for but failed to detect any volatile $WO_x$ or $WO_xF_y$ compounds.

The next step in the model predicts that once the Si substrate is exposed, the rate of W deposition beings to increase and Si diffusion begins, as new reaction pathways, *viz.*

$$2WF_6 + 3Si \rightarrow 2W(s) + 3SiF_4(g) \qquad (3.3)$$

and

$$WF_6 + 3Si \rightarrow W(s) + 3SiF_2(g) \qquad (3.4)$$

become available. These new pathways are much more aggressive than the initial etching reactions [43] so W deposition is accelerated at the points where the Si substrate is first reached. Two

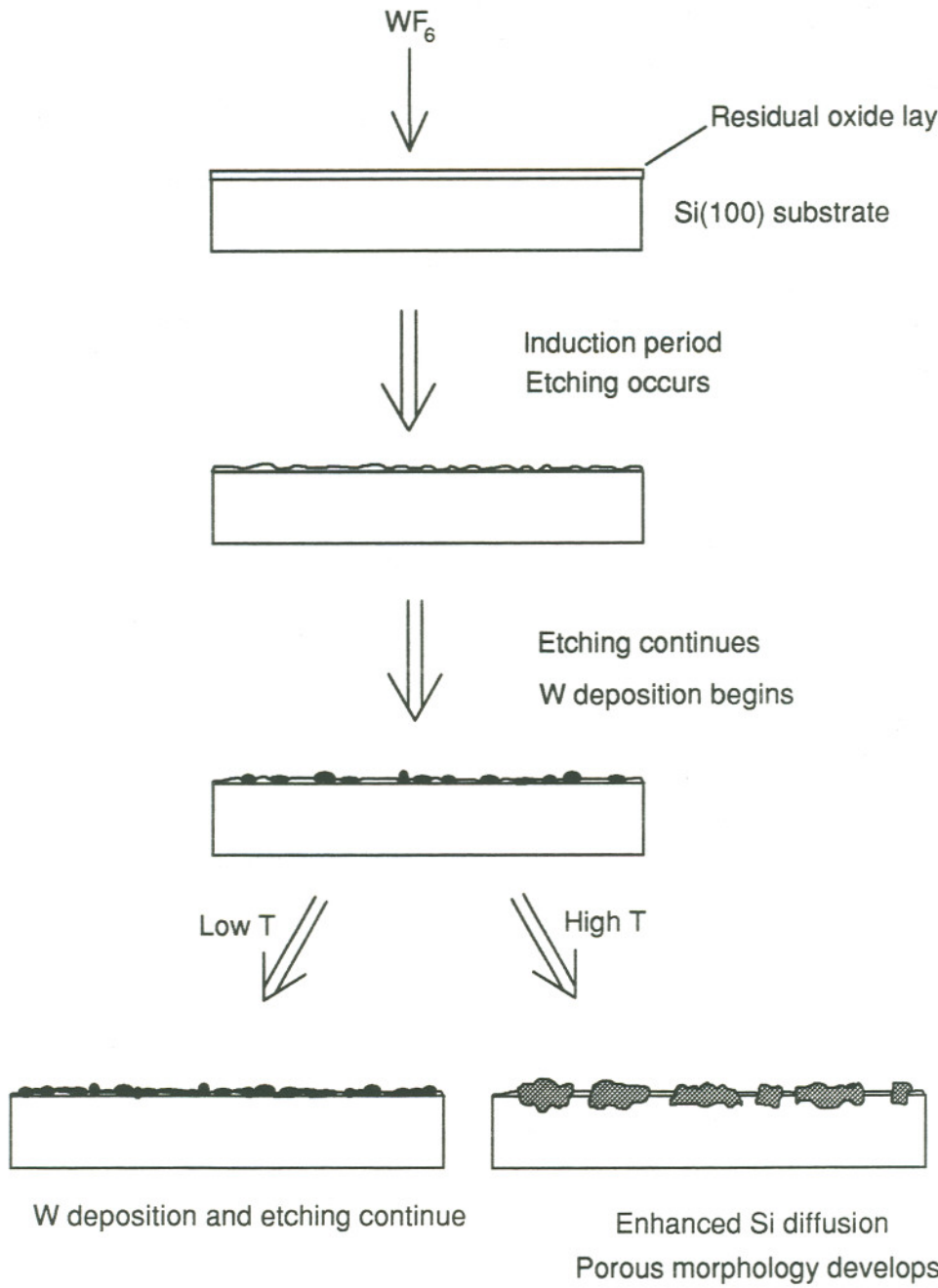


Figure 3.12 Illustration of the $WF_6$ + Si reaction and W film growth with an initial oxide layer.

factors contribute to the enhanced porosity at higher temperatures; a) enhanced Si diffusion, and b) the transition from eq. (3.2) to (3.3) as the dominant reaction pathway at ~ 450°C [9]. The enhancement of Si diffusion brings more Si atoms to the surface of the growing film faster, increasing the capacity for F removal. Eq. (3.3) is a more aggressive etching reaction since more Si atoms are removed per each W atom deposited. At 450 °C and below, there is less of an accelerating effect as the Si substrate is reached, leading to a more uniform (and less thick) film. The temperature dependence of the film morphology is then attributed to a mismatch in Si-O etching versus W deposition reaction rates which increases with temperature.

Several theories have previously attempted to explain film porosity, which ignored the influence of the oxide layer. Kuiper [13] and Green [40] have attributed film porosity to the etching nature of reactions (3.2) and (3.3) together with the molecular volume differences of W and Si [40]. Wood and Collins [46] propose that the evolution of $SiF_4$ creates pores in the depositing film which then lead to hole-like defects. Porous films however, have only been reported for Si surfaces cleaned *ex situ* prior to $WF_6$ exposure, where they are susceptible to O and C contamination from atmospheric gases. In some studies with commercial reactors [21,42] porous films were not observed unless the substrate is initially covered with a relatively thick (2-3 nm) chemically-grown oxide layer. There is a lack of experimental results to support the above-mentioned etching/density/$SiF_x$ evolution theories.

### 3.5 References for Chapter 3

3-1. C. Crowell, J. Savace, and S. Sze, Tr. Metal Soc. AIME 233, 478 (1965).

3-2. E.K. Broadbent and W.T. Stacy, Solid State Technol. 2 (12), 51 1985.

3-3. R.S. Blewer, Solid State Technol. 29 (11), 117 (1986).

3-4. N.E. Miller and I. Beinglass, Solid State Technol. 25 (12), 86 (1982).

3-5. E.K. Broadbent, J. Vac. Sci. Technol. B 5 (6), 1661 (1987).

3-6. U.S. Patent Office, CD-ROM Publication, (1993).

3-7. J.A. Yarmoff and F.R. McFreely, J. Appl. Phys. 63 (11), 5213 (1988).

3-8. R.B. Jackman and J.S. Foord, Surf. Sci. 201, 47 (1988).

3-9. M.L. Yu, B.N. Eldridge, and R.V. Joshi, "Tungsten and other Refractory Metals for VLSI Applications IV", edited by R.S. Blewer and C.M. McConica (Materials Research Society, Pittsburgh, PA, 1989), p. 221.

3-10. P.A.C. Groenen, J.G.A. Holscher, and H.H. Brongersma, Appl. Surf. Sci. 53, 30 (1991).

3-11. E.K. Broadbent and C.L. Ramiller, J. Electrochem. Soc. 131, 1427 (1984).

3-12. K.Y. Ahn, T. Lin, J. Angilello, "Tungsten and other Refractory Metals for VLSI Applications III", edited by V.A. Wells (Materials Research Society, Pittsburgh, PA, 1988), p. 25.

3-13. A.E.T. Kuiper, M.F.C. Willemsen, and J.E.J. Schmitz, Appl. Surf. Sci. 38, 338 (1989).

3-14. M. Wong, N. Kobayashi, R. Browning, D. Paine, and K.C. Saraswat, J. Electrochem. Soc. 134, 2339 (1987).

3-15. C-E. Morosanu and V. Soltuz, Thin Solid Films 52, 181 (1978).

3-16. M.L. Green, Y.S. Ali, B.A. Davidson, L.C. Feldman, and S. Nakahara, Materials Res. Soc. Proc. 54, 723 (1986).

3-17. H.L. Park, C.D. Park, and J.S. Chun, Thin Solid Films 166, 37 (1988).

3-18. K.Y. Tsao and H.H. Busta, J. Electrochem. Soc. 131, 2702 (1984).

3-19. W.T. Stacy, E.K. Broadbent, and M. H. Norcott, J. Electrochem. Soc. 132, 444 (1985).

3-20. D.C. Paine, J.C. Bravman, and K.C. Saraswat, "Tungsten and other Refractory Metals for VLSI Applications", edited by R.S. Blewer (Materials Research Society, Pittsburgh, PA, 1986), p117.

3-21. H.H. Busta and C.H. Tang, J. Electrochem. Soc. 133, 1195 (1986).

3-22. R.S. Blewer, VLSI Multilevel Interconnection Conf. Proc., T.E. Wade, Ed., 306 (1980).

3-23. M.L. Green, Y.S. Ali, T. Boone, B.A. Davidson, L.C. Feldman, and S. Nakahara, "Tungsten and other Refractory Metals for VLSI Applications II", edited by E.K. Broadbent (Materials Research Society, Pittsburgh, PA, 1987), p. 85.

3-24. L.E. Davis, N.C. MacDonald, P.W. Palmberg, G.E. Raich, and R.E. Weber, "Handbook of Auger Electron Spectroscopy", Physical Electronics Division, Perkin-Elmer Corp., Eden Prairie, MN (1978).

3-25. A. Cros, R. Pierrisnard, F. Pierre, and J.M. Layet, Appl. Surf. Sci. 38, 148 (1991).

3-26. S.L. Zhang, U. Smith, R. Buchta, and M. Ostling, J. Appl. Phys. 69 (1), 213 (1991).

3-27. F.M. d'Heurle, C.S. Petersson, and M.Y.Tsai, J. Appl. Phys. 51 (11), 5976 (1981).

3-28. S.P. Murarka, M.H. Read, and C.C. Chang, J. Appl. Phys. 52 (12), 7450 (1981).

3-29. M.L. Yu, K.Y. Ahn, and R.V. Joshi, IBM J. Res. Develop. 34 6, 875 (1990).

3-20. G.J. Luesink, C.R. Kleijn, T.G.M. Oosterlaken, G.C.A.M. Janssen, and S. Radelaar, J. Appl. Phys. 72(2), 490 (1992).

3-31. M.L. Yu, B.N. Eldridge, and R.V. Joshi, AIP Conf. Proc. 167, 202 (1988)

3-32. J.A. Yarmoff and F.R. McFreely, AIP Conf. Proc. 167, 210 (1988).

3-33. J. Wood, Appl. Surf. Sci. 38, 397 (1989).

3-34. R.S. Blewer and M.E. Tracy, "Tungsten and other Refractory Metals for VLSI Applications", edited by R.S. Blewer (Materials Research Society, Pittsburgh, PA, 1986), p. 53.

3-35. D.J. Silversmith, D.D. Rathman, and R.W. Mountain, Thin Solid Films 93, 413 (1982).

3-36. H. Itoh, N. Kaji, T. Watanabe, and H. Okano, Jap. J. Appl. Phys. 30, 1525 (1991).

3-37. R. Arora and R. Pollard, J. Electrochem. Soc. 138, 1523 (1991).

3-38. M.L. Hitchman, A.D. Jobson, L. F. Tz. Kwakman, Appl. Surf. Sci. 38, 312 (1989).

3-39. G.B. Raupp and G.T. Hindman, "Tungsten and other Refractory Metals for VLSI Applications IV", edited by R.S. Blewer and C.M. McConica (Materials Research Society, Pittsburgh, PA, 1989), p. 231.

3-40. M.L. Green and R.A. Levy, J. Electrochem. Soc. 132 (5), 1243 (1985).

3-41. J.E.J. Schmitz, "Chemical Vapor Deposition of Tungsten and Tungsten Silicides", Noyes Publications, New Park, NJ, 1992.

3-42. J. Holleman, A. Hasper, and J. Middlehoek, J. Electrochem. Soc. 138, 783 (1991).

3-43. J-O Carlsson and M. Boman, J. Vac. Sci. Technol. A 3(6), 2298 (1985).

3-44. S.P. Murarka, J. Vac. Sci. Technol. 17(4), 775 (1980).

3-45. D.A.Bell, Mat. Res. Corp. Tech. Report # T92197 (1992).

3-46. J. Wood and R. Collins, Appl. Surf. Sci. 38, 359 (1989).

# 4

# $WF_6$ AND $SiH_4$ REACTIONS WITH TiN SURFACES

## 4.1 Introduction

CVD W films used for applications in integrated circuit manufacturing usually employ the blanket deposition technique [1]. The blanket CVD W film deposition is typically a two-step process, with the W film deposited onto a thin (20-50 nm) TiN film which serves as an adhesion layer to promote uniform W growth and sometimes as a diffusion barrier between the W and underlying Si or silicide layers [1-3]. The first step is a nucleation step in which $WF_6$ reacts heterogeneously with $SiH_4$ on the TiN surface, forming a thin layer of W. The second step uses $H_2$ reduction of $WF_6$ to deposit the remainder of the W film, 0.5-1 μm total thickness. The $H_2$ reduction reaction gives a higher deposition rate and a more pure W film, but nucleation on TiN surfaces is relatively slow with poor uniformity [1,4]. The $SiH_4$ reduction reaction is thus necessary to quickly deposit a uniform W "seed" layer upon which the $H_2$ reduction reaction can take place.

Since the nucleation reactions take place on the TiN surface, the reactions are expected to be sensitive to the chemical and possibly the physical properties of the TiN surface. The sensitivity of such reactions to surface conditions has already been demonstrated in Chapter 3 with the use of Si(100) substrates, and past studies of the nucleation reactions suggest a sensitivity to surface conditions [5,6]. It is therefore expected that the nucleation reactions will be sensitive to the TiN surface conditions as well. The work in this Chapter address how the nucleation reactions are influenced by differences in chemical and physical properties of TiN surfaces. The differences were due to differences in deposition techniques, deposition chemistries, and sample cleaning techniques and represent normal variations one would expect to encounter in a manufacturing environment. Examples of these variations include, film crystal structures and chemical impurities.

In modern small-geometry integrated circuits, TiN films deposited by chemical vapor

deposition are being considered [7,8] as an alternative to conventional sputter-deposited TiN films. The CVD films have better conformal coverage than sputtered films into structures with large depth-to-width aspect ratios. The potential use of CVD TiN films however raises the question of how the W CVD reactions, especially the nucleation reactions might be different. The films deposited by CVD methods could have subtle chemical composition and/or microstructural differences that could affect the $WF_6$ and $SiH_4$ reactions on the surface. This issue was partially investigated by Kumar, *et.al.* recently who made comparisons [9,10] of $WF_6$ reactions on LPCVD and sputtered TiN surfaces. Their results suggest that there may be some difference in the reaction mechanisms in that the reaction of $WF_6$ with the CVD TiN surface appeared to be more aggressive, depositing a thicker W layer. The differences in the TiN films were not well characterized however, which eliminated any possibility of assigning a conclusive explanation to the observed differences.

The different deposition techniques introduce differences in the TiN surface properties that are generally repeatable and fixed. A less predictable concern is how the nucleation reactions are affected by variations in TiN surface properties introduced by more subtle means. One such example is the exposure of the TiN films to atmosphere. In typical industrial applications the TiN films are transported from the sputter deposition chamber to the CVD W reactor in atmosphere where they are susceptible to oxidation and adsorption of airborne chemical contaminants. The amount of oxidation and/or residual contamination may change with time spent between process steps and these changes could influence the reactions on the surface. This was partially explored by Yu, et.al. [6] with previous thermal desorption and molecular beam dosing experiments. They studied the reactions of TiN surfaces with $WF_6$ and $SiH_4$ independently in a carefully controlled UHV environment. Although the thrust of the experiments was to characterize how $WF_6$ and $SiH_4$ reacted with pristine UHV-prepared TiN surfaces, some experiments were performed with "industrial" TiN surfaces that were sputter deposited TiN films that had been exposed to atmosphere. Their results showed that both $WF_6$ and $SiH_4$ dissociated on and reacted with the pristine TiN, and that these reactions were inhibited on the "industrial" TiN surfaces at room temperature. These results raise a number of questions, such as how the adsorption and decomposition of $WF_6$ and $SiH_4$ on TiN surfaces would be affected at higher temperatures typical of industrial processing, and whether the reactions can be controlled by surface preparation. The work in this chapter addresses these questions in detail. The initial reactions of TiN with $WF_6$ and $SiH_4$ are characterized using *in situ* Auger electron spectroscopy (AES) over a range of typical process temperatures, 300-550 °C. The surface reactions with typical industrial TiN films are compared to reactions on TiN surfaces prepared with *in vacuo* sputter cleaning and/or annealing.

Other influences could be TiN film microstructure or surface morphology, both of which are known to be dependent on the TiN deposition conditions [11,12]. The oxidation kinetics of TiN have been studied under a variety of environmental conditions [13,14], and are known to be influenced by the film microstructure [15,16]. It is therefore plausible that the film microstructure may also influence the $WF_6$ and $SiH_4$ adsorption reactions. This point is addressed in the experiments below. High-resolution FESEM and AFM were used to characterize the physical structures of the TiN film surfaces prior to $WF_6$ and $SiH_4$ adsorption experiments.

Another issue that is addressed below is the apparent confusion surrounding studies of $WF_6$ + TiN reactions that has lead to the speculation that W somehow "penetrates" the TiN layer [10,17]. Auger sputter depth profiles that showed long W "tails" as the TiN films were removed were ascribed to an intermixing phenomenon where the W atoms from $WF_6$ adsorption had either penetrated the TiN matrix forming a W-Ti compound [17], or had diffused into the film along grain boundaries [10]. Both of these explanations are unlikely however, and this issue is revisited in light of the results presented herein, with more plausible explanations given for the apparent intermixing phenomena.

## 4.2 TiN Sample Preparation and Characterization

### 4.2.1 RIS TiN

The reactive ion sputtered TiN films were ~ 35 nm thick and had been deposited over a 1 μm $SiO_2$ film on a p-type Si wafer. The RIS TiN deposition procedure, performed at Intel Corp., consisted of sputtering a Ti target with a $N_2$/Ar gas mixture. The films used in this study were grown under typical manufacturing conditions in order to get a fair representation of an "industrial" TiN film for the surface chemistry experiments. Fig. 4-1 shows a high magnification SEM image of a RIS TiN cross section. The film appears to have a columnar-like grain structure, although it is not well defined. There are also two distinct layers within the film. This was caused by using a two step deposition in order to ensure complete TiN coverage at locations were the front side of the wafer was held by clamps. AFM images of the TiN give a more clear indication of the surface topography. Fig. 4-2 shows top and surface plot AFM images of the RIS TiN surface as deposited. The ~ 10 nm diameter circular features are the tops of the columnar grains. The RMS surface roughness of the RIS TiN was 0.847 nm.

Some of the TiN samples were sputter cleaned with a 3 kV Ar beam rastered over the entire sample. This was done to remove any residual surface oxidation and contamination. The

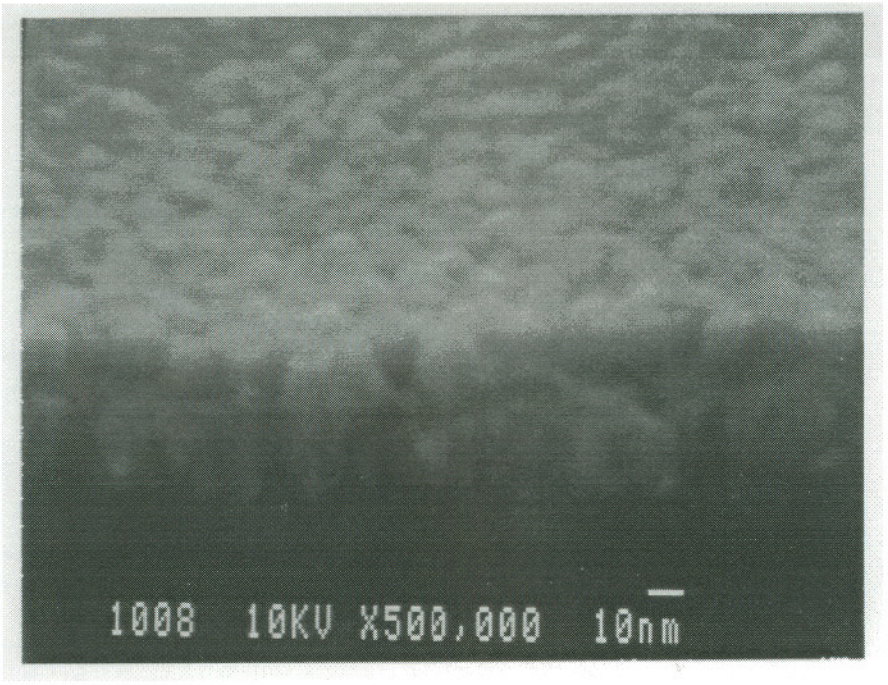


Figure 4-1. High resolution SEM image of RIS TiN film cross-section.

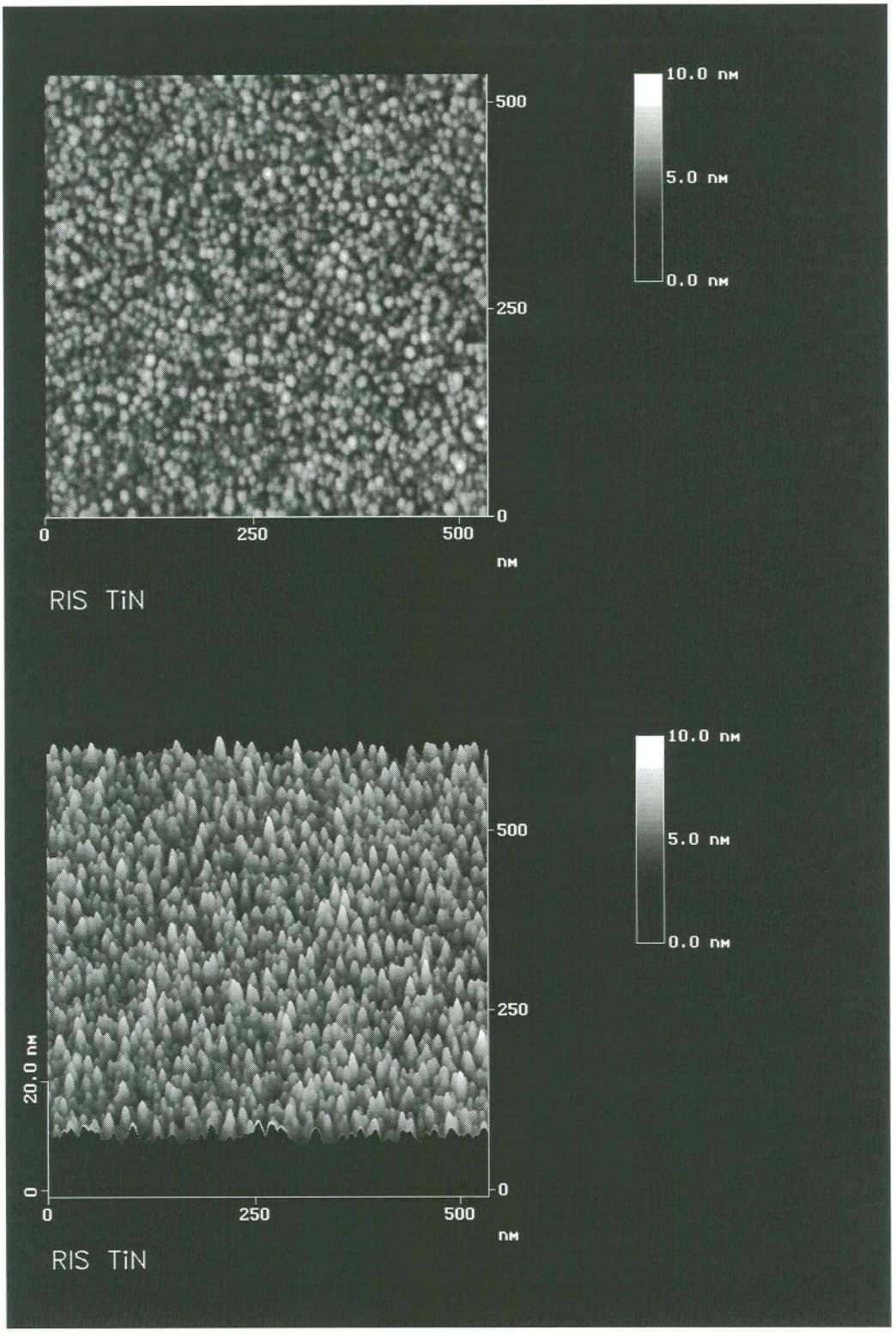


Figure 4-2. Top view and surface plot AFM images of RIS TiN surfaces.

physical effect of sputtering on the surface is illustrated in Fig. 4-3. Here the grains are elongated in the direction of the glancing-incidence Ar ion beam. After sputtering, the surface roughness slightly increased to 1.079 nm.

Both O and C were detected on the RIS TiN surface prior to sputter cleaning. Fig. 4-4 shows a typical derivative Auger spectrum from an as-received TiN surface before and after $WF_6$ exposure. The C(KLL), Ti(LMM), Ti(LMV), N(KLL), O(KLL), W(NOO), and F(KLL) transitions are labeled in the Figure. The peak-to-peak amplitudes of these transitions, along with the Si(LVV) transition at 92 eV were used to monitor the surface chemistry as the samples were exposed to $WF_6$ and/or $SiH_4$. Since the only N Auger transition, N(KLL) overlaps with the dominant Ti(LMM) transition, a quantitative determination of the TiN stoichiometry was not possible. In order to measure film stoichiometries, RBS analyses were performed on the films. The results showed a 1:1 stoichiometry to within a few atomic percent, and an O concentration of ~ 1 % throughout film. The C and O on the surface were attributed to adsorbed atmospheric gases because they could mostly be removed by sputtering. Using both AES and XPS measurements, the depth of oxidation was estimated (*cf.* Ref. 3-24) to be ~ 1 nm. The surface atomic concentration of C on the TiN was estimated at ~ 10 % and no evidence of Ti-C compounds was observed. This amount of oxidation and C contamination is typical of RIS TiN films exposed to atmosphere [4,14].

XPS analysis showed that the TiN surface was actually oxidized. Fig. 4-5 shows the shape of the Ti 2p photoelectron peak envelope before and after sputter cleaning. The strong Ti $2p_{3/2}$ component at 458 eV binding energy in Fig. 4-5(a) is indicative of Ti-O bonding [18]. After sputter cleaning, the Ti $2p_{3/2}$ peak main component is at 455 eV, which is typical for TiN [19,20]. The shoulder at 458 eV in Fig. 4-5(b) is attributed to residual oxygen in the TiN film, which is typically about 1 % at. concentration and is expected to be found along grain boundaries. The $2p_{3/2}$ peak for metallic Ti has a binding energy of 453.8 eV [20]. Since no metallic Ti peak was observed, any chemical effect due to preferential sputtering of N versus Ti was thought to be minor.

### 4.2.2 MOCVD TiN

The MOCVD TiN films were about 35 nm thick and deposited onto $SiO_2$ with a temperature of about 450 °C. The films, deposited at Novellus Corp., utilized tetrakisdimethylamidotitanium as the metal-source precursor and $H_2$ was used as a reductant gas. The TiN films were deposited by thermal decomposition of the precursor, and $H_2$ was added to help remove reaction by-products, giving a more pure TiN film. An SEM image of a film cross

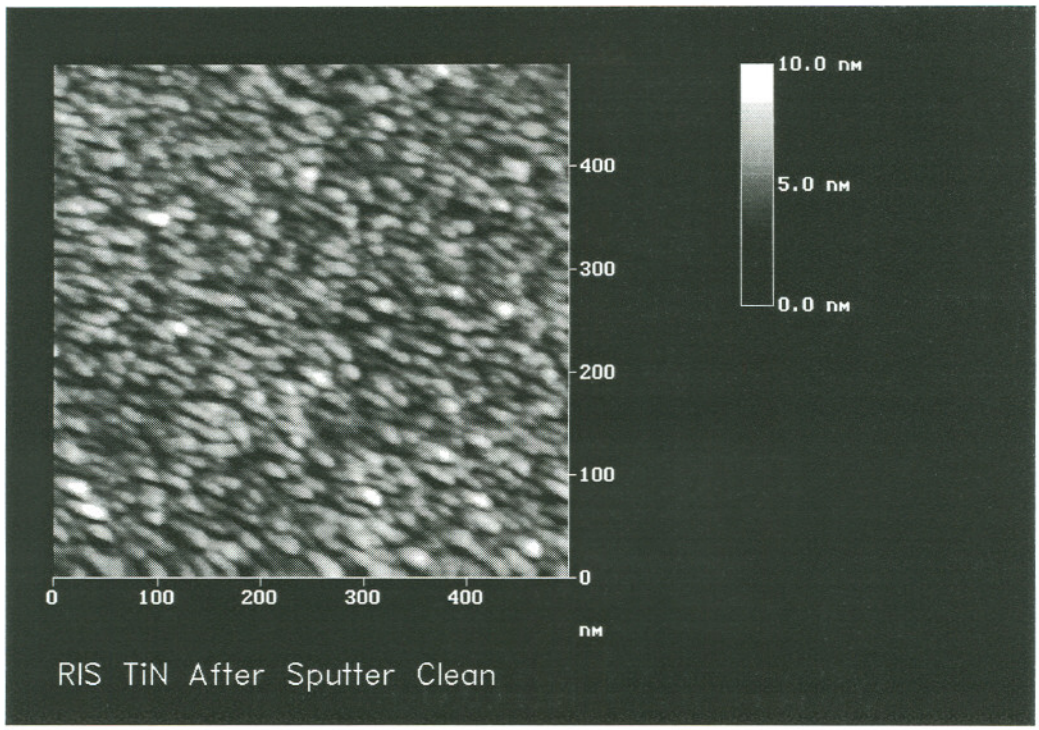


Figure 4-3. Top view AFM image of RIS TiN surface after Ar sputter cleaning.

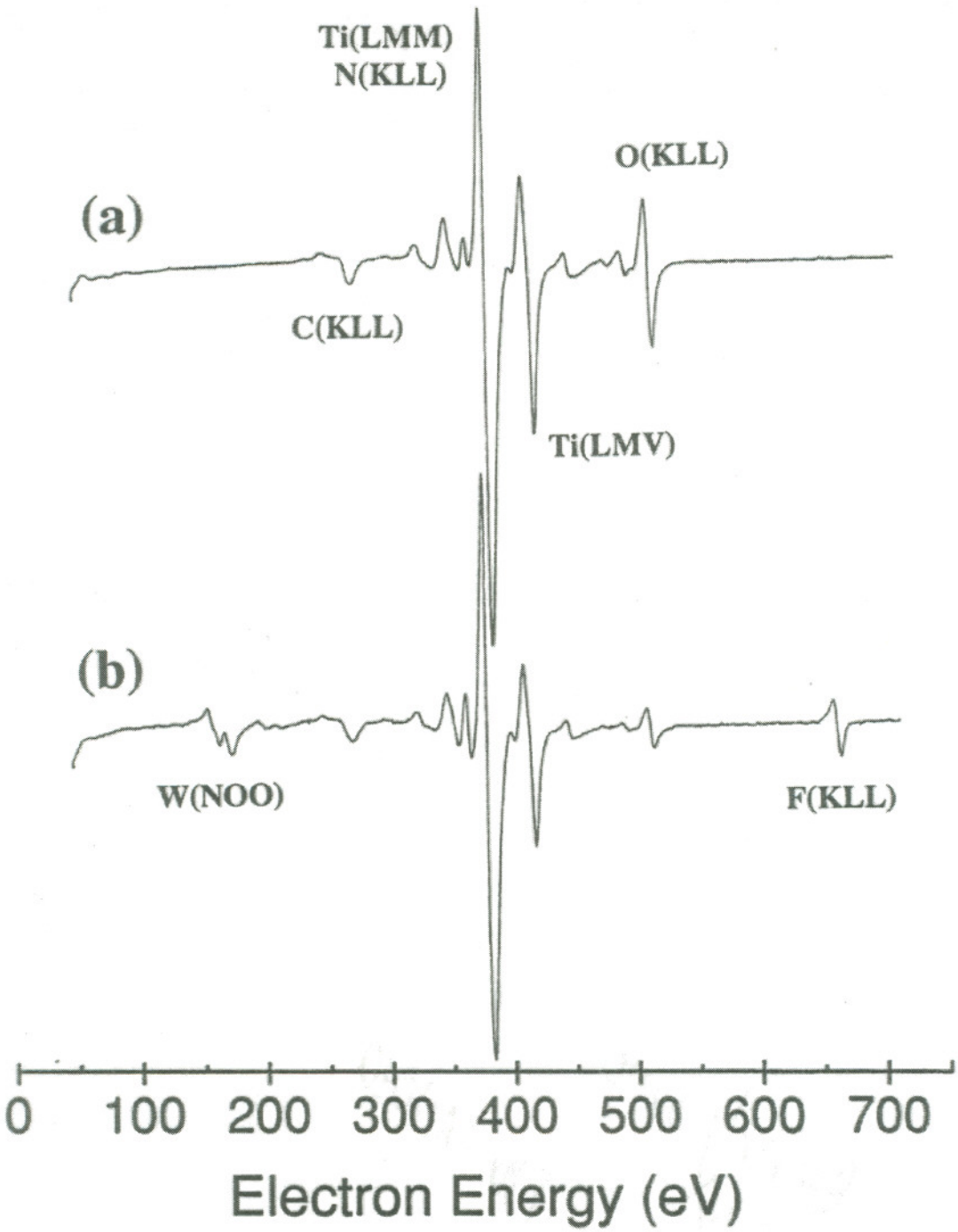


Figure 4-4. Typical Auger derivative spectra from TiN surface before and after expsure to $WF_6$.

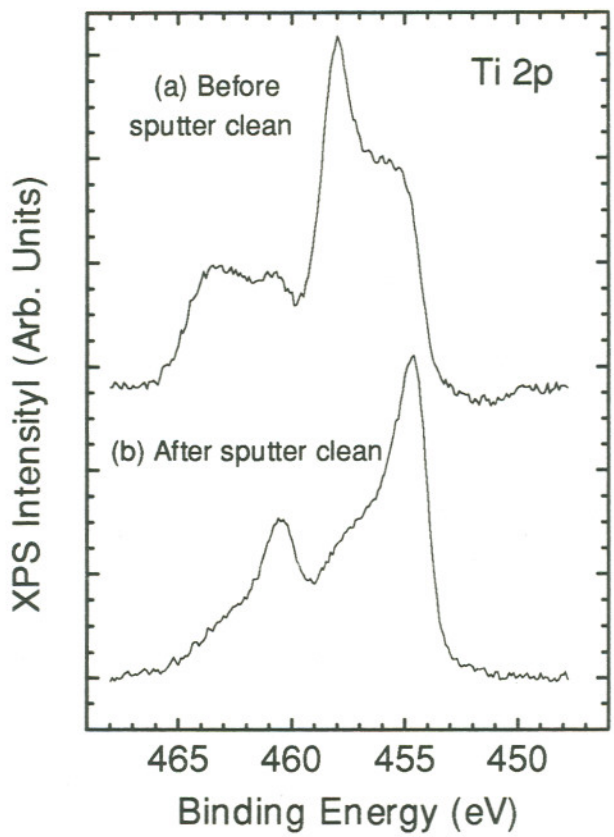


Figure 4-5. Ti 2p photoelectron peak signals from a TiN surface before and after sputter cleaning, showing the initial oxidized state of the surface.

section in Fig. 4-6 reveals a columnar structure with more surface texture than the RIS film. AFM images of this film, shown in Fig. 4-7, revealed a structure of small, ~ 7 nm grains grouped into clusters. This is indicative of a more homogenous reaction i.e. spherical or equiaxial grains. The RMS roughness of the MOCVD TiN was 2.388 nm, which is about twice that found for the RIS TiN.

The MOCVD TiN films had more surface O and C than the RIS TiN as detected with AES. Fig. 4-8 compares the relative amounts of surface O and C for the different TiN films determined from Auger derivative spectra. The data points represent an average of 15-20 separate Auger measurements and the error bars correspond to a 95% confidence interval. This plot also gives an indication of the repeatability of the Auger measurements. The additional contaminants in the MOCVD TiN film was attributed in part to unreacted or partially reacted precursor molecules caught in the film.

$WF_6$ and $SiH_4$ adsorption experiments were also carried out on the MOCVD TiN after sputter cleaning. After sputter cleaning, this film had about the same texture as the RIS film, *i.e.* elongated grains and increased roughness. The amounts of O and C were higher throughout the film, however, as indicated in Fig. 4-9, which compares Auger in-depth profile data through the RIS and MOCVD TiN films.

### 4.2.3 LPCVD TiN

The LPCVD TiN films were ~ 50 nm thick and deposited at Materials Research Corp. using an $NH_3 + TiCl_4 + H_2$ chemistry. The deposition temperature was ~ 450 °C and the substrate was a Si(100) wafer. The reaction responsible for TiN deposition was presumed to be a surface reaction of

$$TiCl_4 + NH_3 + \tfrac{1}{2}H_2 \rightarrow TiN + 4HCl \qquad (4.1)$$

Fig. 4-10 shows a SEM image of a film cross section. The columnar grain structure is more evident with this film, and the grain diameters appear to increase with film thickness. Another feature of the LPCVD film is the enhanced roughness of the TiN/Si interface. An AFM image of the LPCVD TiN surface is shown Fig. 4-11. This film had an RMS roughness of 2.625 nm. The grain diameters were 15-20 nm at the surface of the film.

In addition to surface O and C, the LPCVD TiN also contained Cl. RBS measurements detected an average Cl concentration of about 2% within in the film. Initial Auger scans confirmed this concentration level at the surface. Previous ESCA studies of these types of films [21] suggest

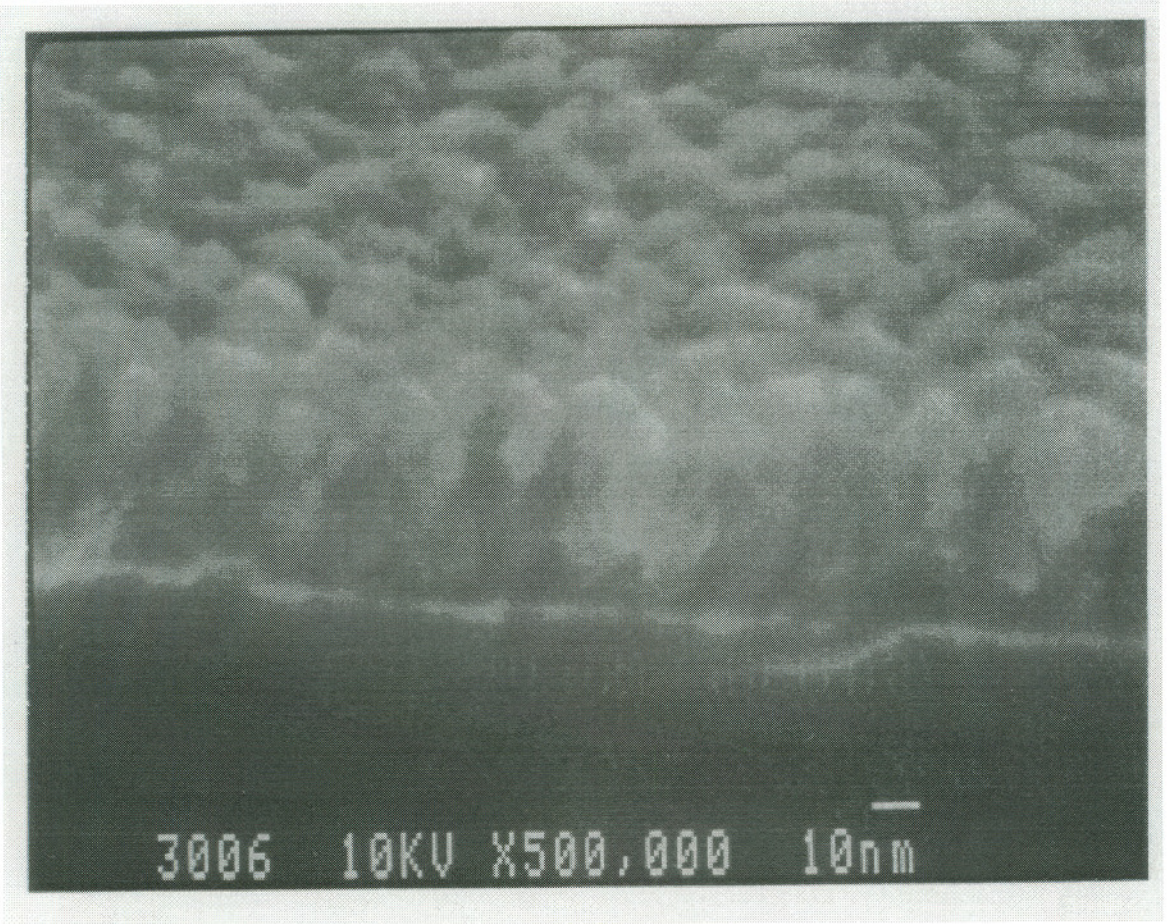


Figure 4-6. High resolution SEM image of MOCVD TiN cross section.

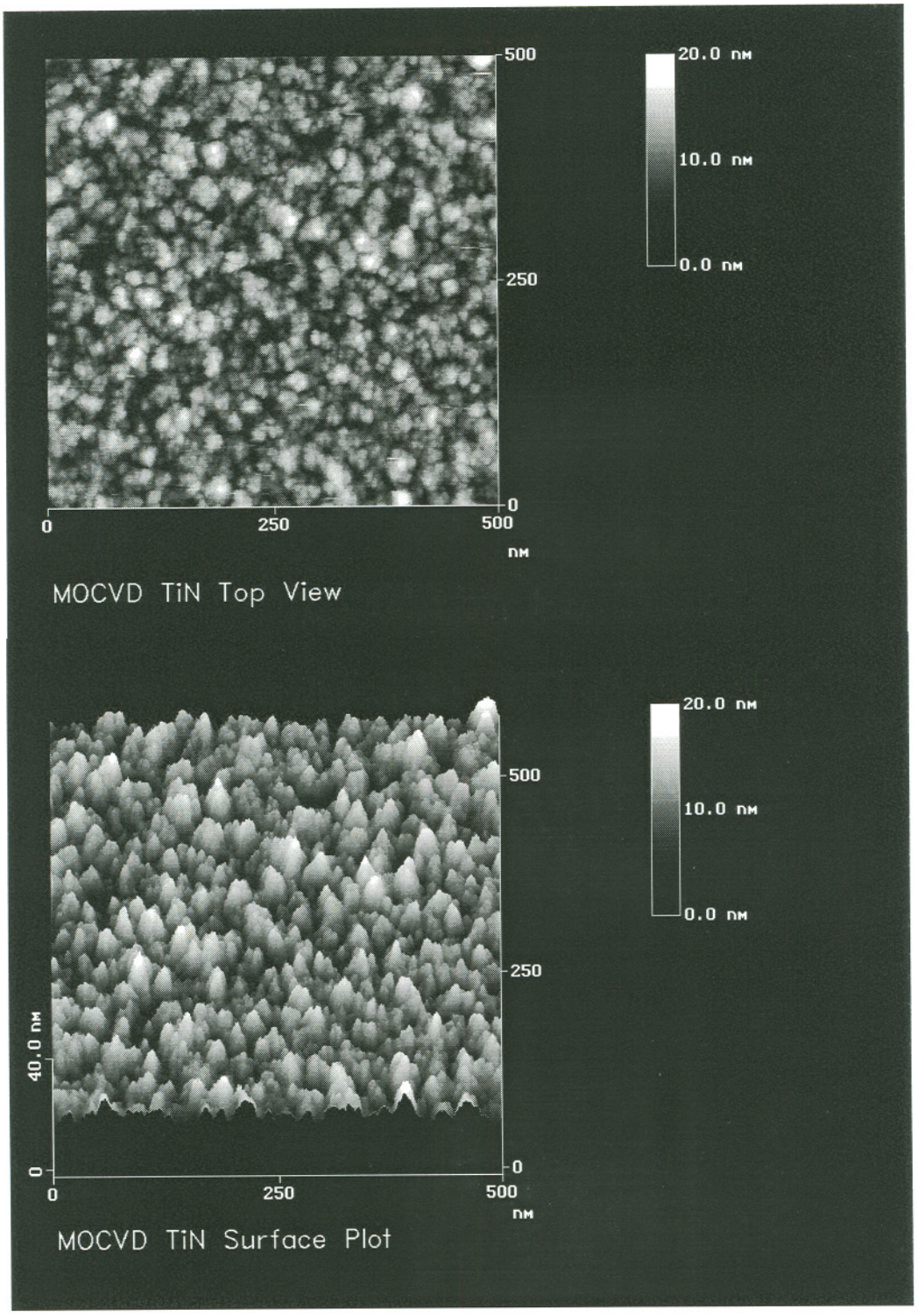


Figure 4-7. Top view and surface plot AFM images of MOCVD TiN surfaces.

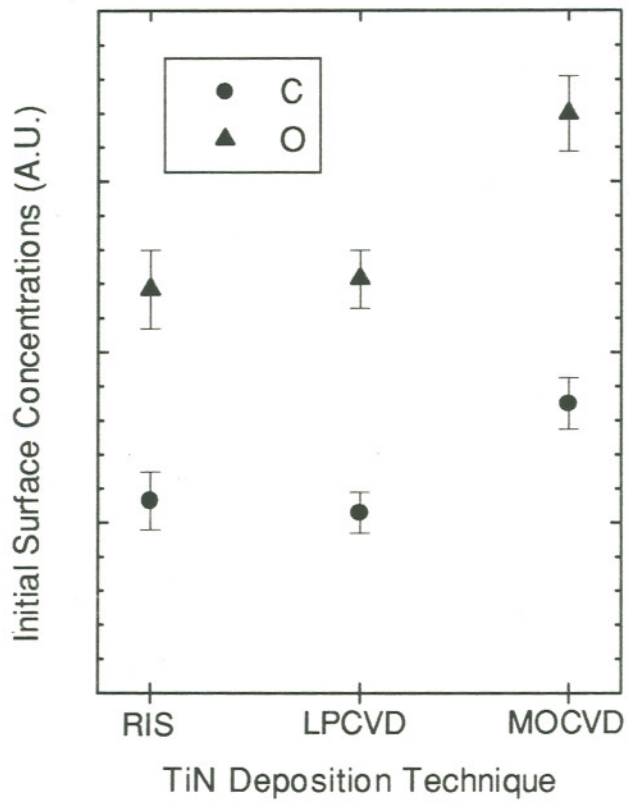


Figure 4-8. Surface O and C on TiN films after exposure to atmosphere.

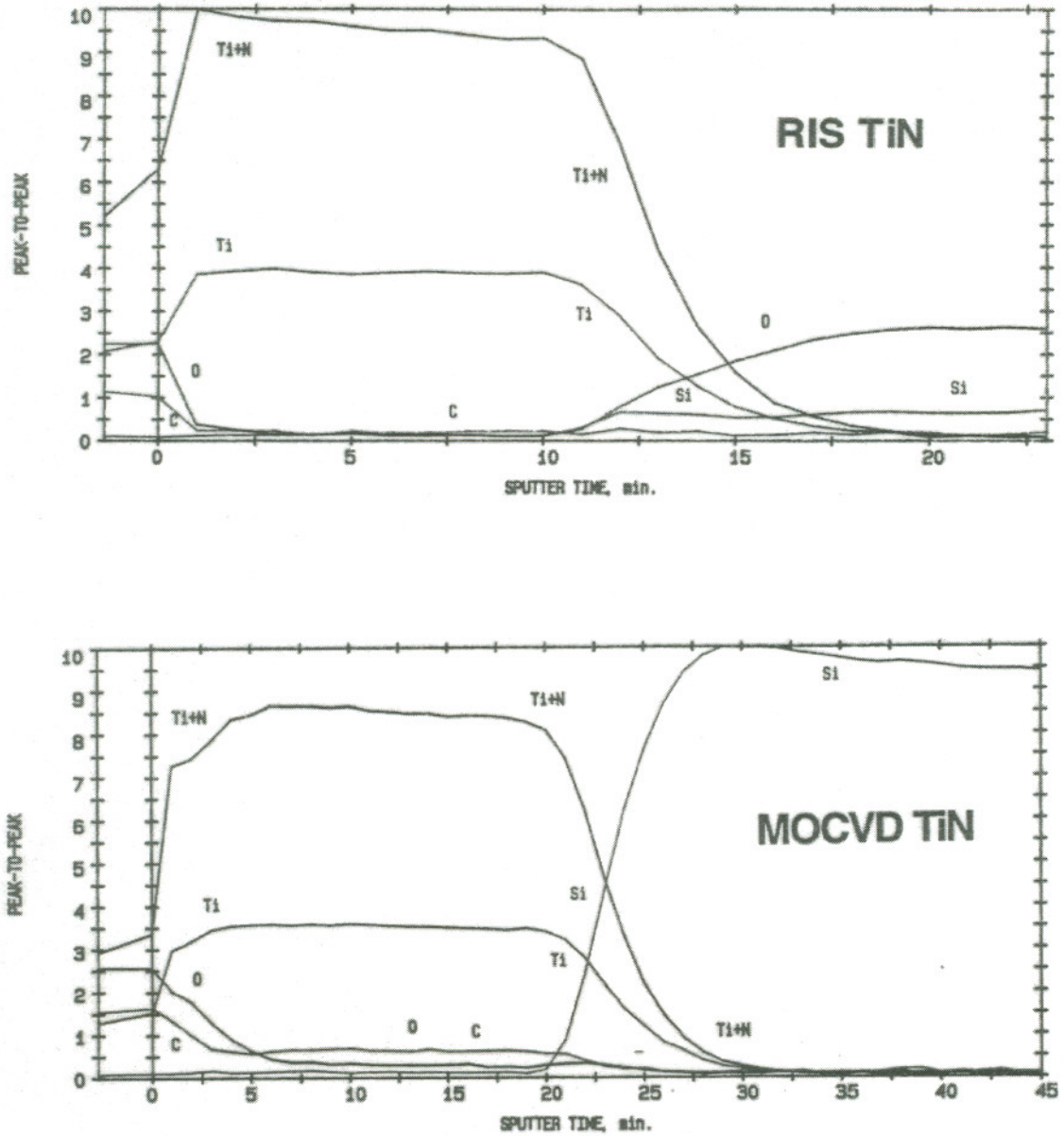


Figure 4-9. Auger sputter depth profiles of RIS TiN and MOCVD TiN films.

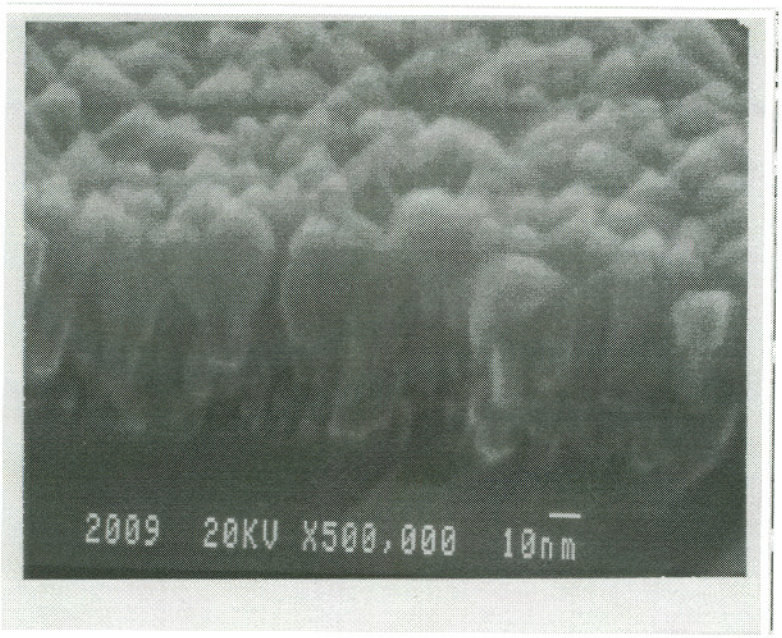


Figure 4-10. High resolution SEM image of LPCVD TiN cross section.

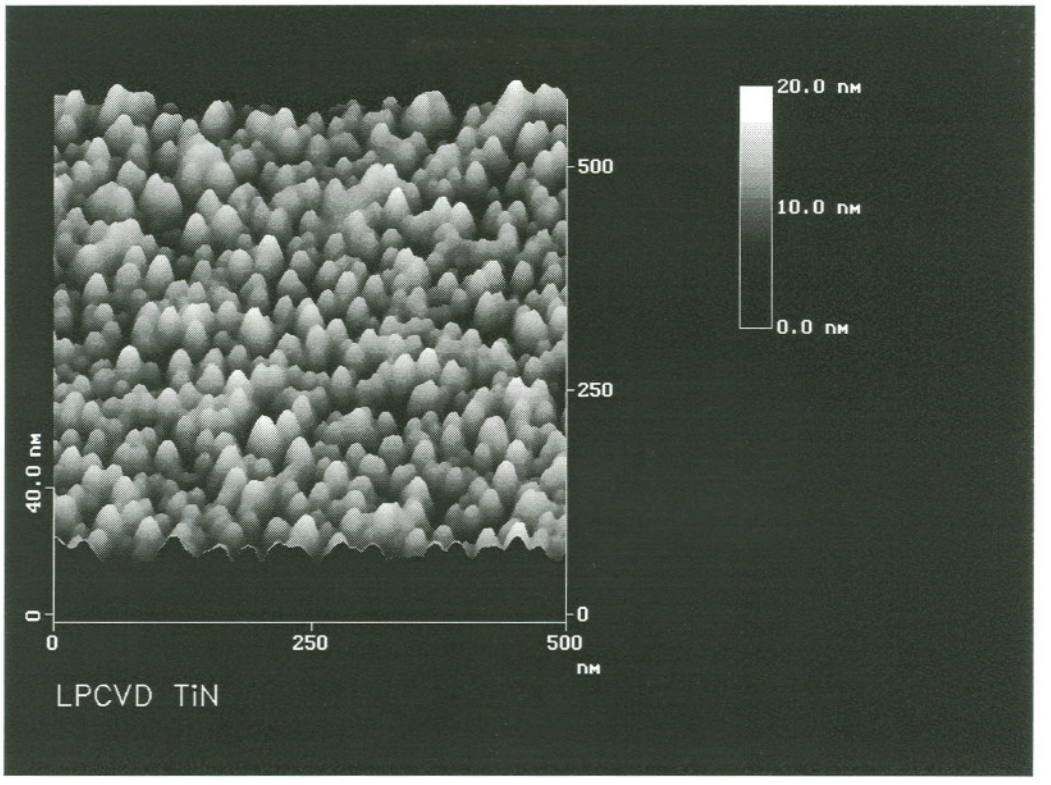


Figure 4-11. Surface plot AFM image of LPCVD TiN surface.

that this Cl is bound to the Ti forming a Ti-Cl-N matrix. Nearly all of the detectable surface Cl could be desorbed by annealing the samples to 400-450 °C for a few seconds. *In situ* RGA studies showed that both Cl and HCl were desorbed upon annealing. Thus by removing Cl and H from the surface by annealing, the combined influence of these elements on the CVD W reactions could therefore be studied independently. The initial concentrations of O and C are compared to the RIS and MOCVD TiN films in Fig. 4-8. Auger depth profiles through the LPCVD film detected about the same amounts of these elements as the RIS film.

### 4.2.4 $WF_6$ and $SiH_4$ Dosing Procedures

The gas exposures were carried out sequentially and the samples were analyzed with AES between exposures. Auger data were collected using an incident beam energy of 3 keV at 10 μA with a spot size of ~ 10 μm. Prolonged exposure to the incident Auger electron beam changed the TiN surface chemistry and caused F desorption. Therefore, the samples were moved perpendicular to the incident beam between the sequential measurements to expose a fresh area on the sample for each measurement. Auger derivative spectra were used to monitor the initial $WF_6$ and $SiH_4$ reactions. Unless otherwise indicated, the W(NOO) transition at 180 eV and the Si(LVV) transition at 92 eV were used to measure the amounts of these elements on the surface. Independent RBS measurements performed at Charles Evans & Associates were used to calibrate the W(NOO) Auger measurements for absolute coverages. Fig. 4-12 shows how derivative peak-to-peak amplitudes of the W(NOO) Auger transition correlates with absolute W coverage as measured by RBS. The relationship is linear over the entire range shown here. This correlation was used to infer W coverages from Auger derivative intensities. Only a qualitative determination of surface F coverage was possible because of electron stimulated desorption of the F. The peak shape of the Si(LVV) transition was sensitive to the presence of O on the surface, which prevented quantitative determinations of surface Si concentrations from the $SiH_4$ adsorption reactions. Semi-quantitative determinations were made from the Auger data.

## 4.3 $WF_6$ reactions with TiN, no pre-cleaning

The initial $WF_6$ + TiN reaction deposited W and F on the surface. This is illustrated in Fig. 4-13 which shows how the peak-to-peak magnitudes of the Ti(LMV), O(KLL), W(NOO), F(KLL), and C(KLL) transitions changed with $WF_6$ exposures up to 250 L. The substrate was a RIS TiN sample held at 500 °C and had received no cleaning prior to the $WF_6$ exposures. Initially the O and Ti signals decreased as W and F deposited on the surface. After about 20 L a saturation

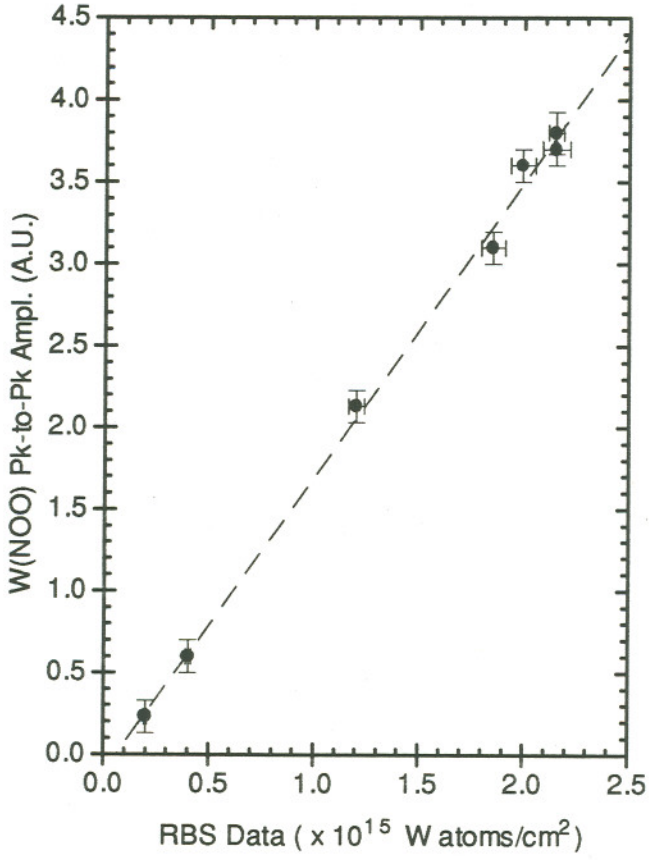


Figure 4-12. Correlation of Auger peak-to-peak amplitudes with RBS measurements.

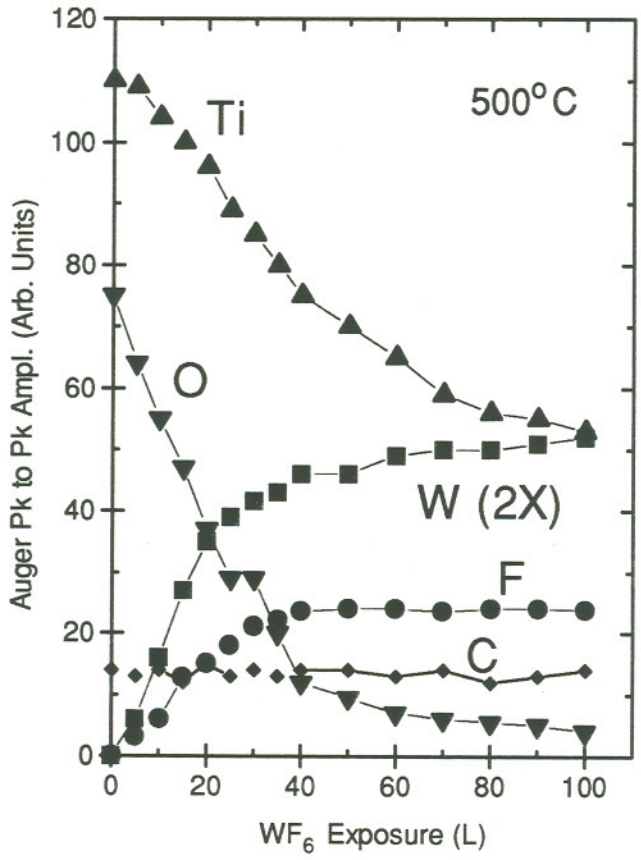


Figure 4-13. Auger peak-to-peak amplitudes for Ti(LMV), O(KLL), W(NOO), F(KLL), and C(KLL) from a RIS TiN surface after sequential expsoures to $WF_6$ at 500 °C.

effect was noticeable where the rates of W and F deposition appear to decrease. The Ti and O signals did not decrease very much beyond this point. In a later discussion this saturation effect is attributed to the surface being passivated by F. The C signal does not change very much at all during these exposures suggesting that the C atoms remain uncovered and do not participate in the initial reaction.

The initial $WF_6$ reactions were qualitatively similar on all three TiN substrates. Fig. 4-14 compares changes in the W, Ti, and O signals when the substrates were exposed to $WF_6$ up to 50 L. These samples were all held at 500 °C during the $WF_6$ exposures. In each case the saturation effect is observed after 20 L, and the O signal always decreases quicker than the Ti signal. The O signal would be expected to decrease faster if the O were consumed from the surface, forming a volatile reaction product such as $WO_xF_y$, or $TiO_xF_y$. The later would also consume Ti from the surface, but since more Ti atoms would be uncovered in the process, the Ti signal wouldn't decrease as much as the O signal. The more rapid decrease in the O signal is therefore consistent with the chemical decomposition of the Ti-O-N surface.

The decomposition of the surface $TiO_2$ would also tend to give a lower effective Ti/(Ti+N) ratio as the $WF_6$ reaction proceeded. This is indeed observed as illustrated in Fig. 4-15. Here the ratio of the Ti(LMV) to the sum of the overlapping Ti(LMM) and N(KLL) peaks are plotted versus $WF_6$ exposure for two different temperatures. Although not strictly quantitative, it does show that the relative Ti:N concentration on the surface decreases as the $WF_6$ reaction proceeds. Hence the initial $WF_6$ reaction appears to involve some etching of the surface because the surface was initially covered with $TiO_2$. This effect is more pronounced at higher temperatures, where the addition of thermal energy makes the etching reaction more favorable.

Both the initial $WF_6$ reaction rate and the saturation level increased with temperature. Fig. 4-16 shows the uptake of W from $WF_6$ + TiN reactions at 300, 450, and 550 °C. W coverages, estimated from Fig. 4-12, are plotted versus $WF_6$ exposure at these temperatures for all three TiN substrates. As seen in the Figure the initial reaction probability, or reaction rate increased with temperature. The saturation effect was observed throughout the temperature range, and the saturation levels also increased with temperature. There is a distinct difference in the saturation levels for the three different TiN films in that the saturation occurs at higher W concentrations on the CVD films.

The dashed lines shown in the plots represent the results of a first order kinetic model to the data. This model, which effectively describes the initial uptake of W on the TiN surfaces

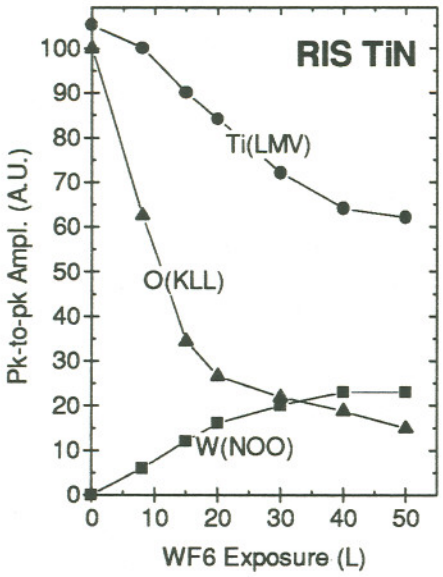


(a)

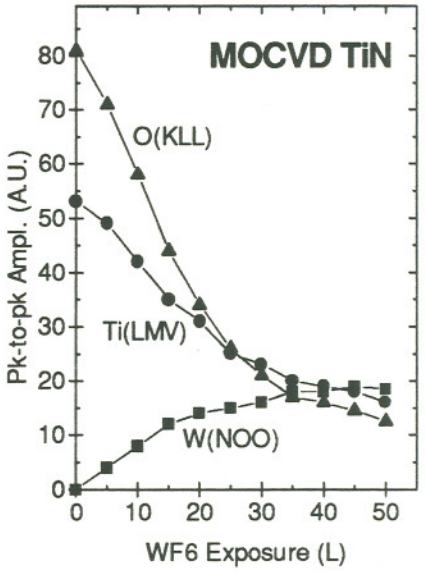


(b)

(c)

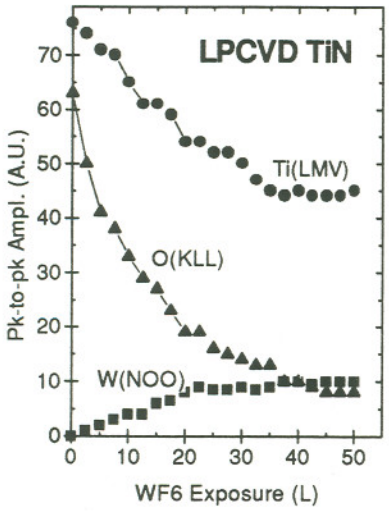


Figure 4-14. Auger peak-to-peak amplitudes for Ti(LMV), O(KLL), and W(NOO) from TiN surfaces after sequential expsoures to $WF_6$ at 500 °C: (a) RIS TiN, (b) MOCVD TiN, (c) LPCVD TiN.

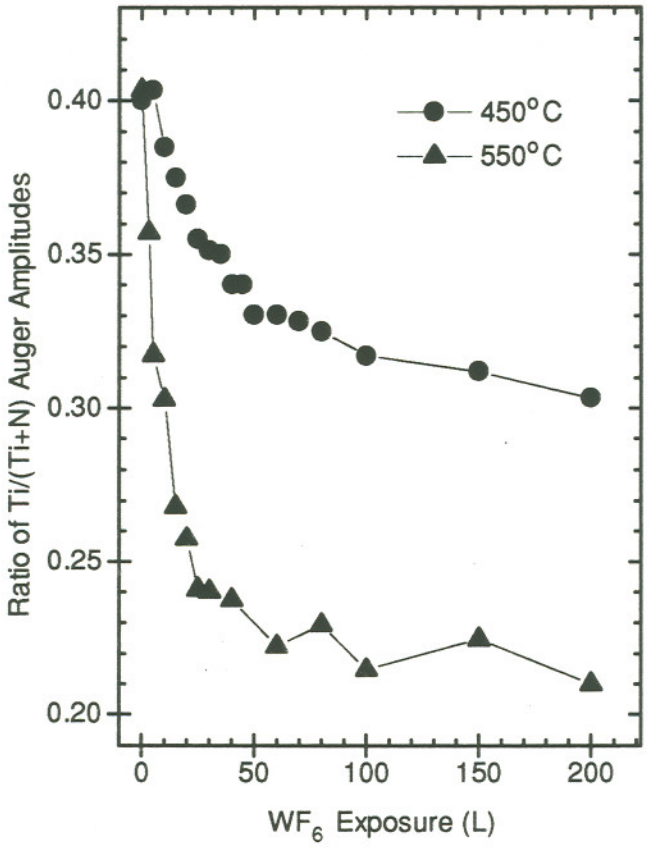


Figure 4-15. Changes in Ti(LMV) to Ti(LMM) + N(KLL) ratios from a TiN surface after exposures to $WF_6$.

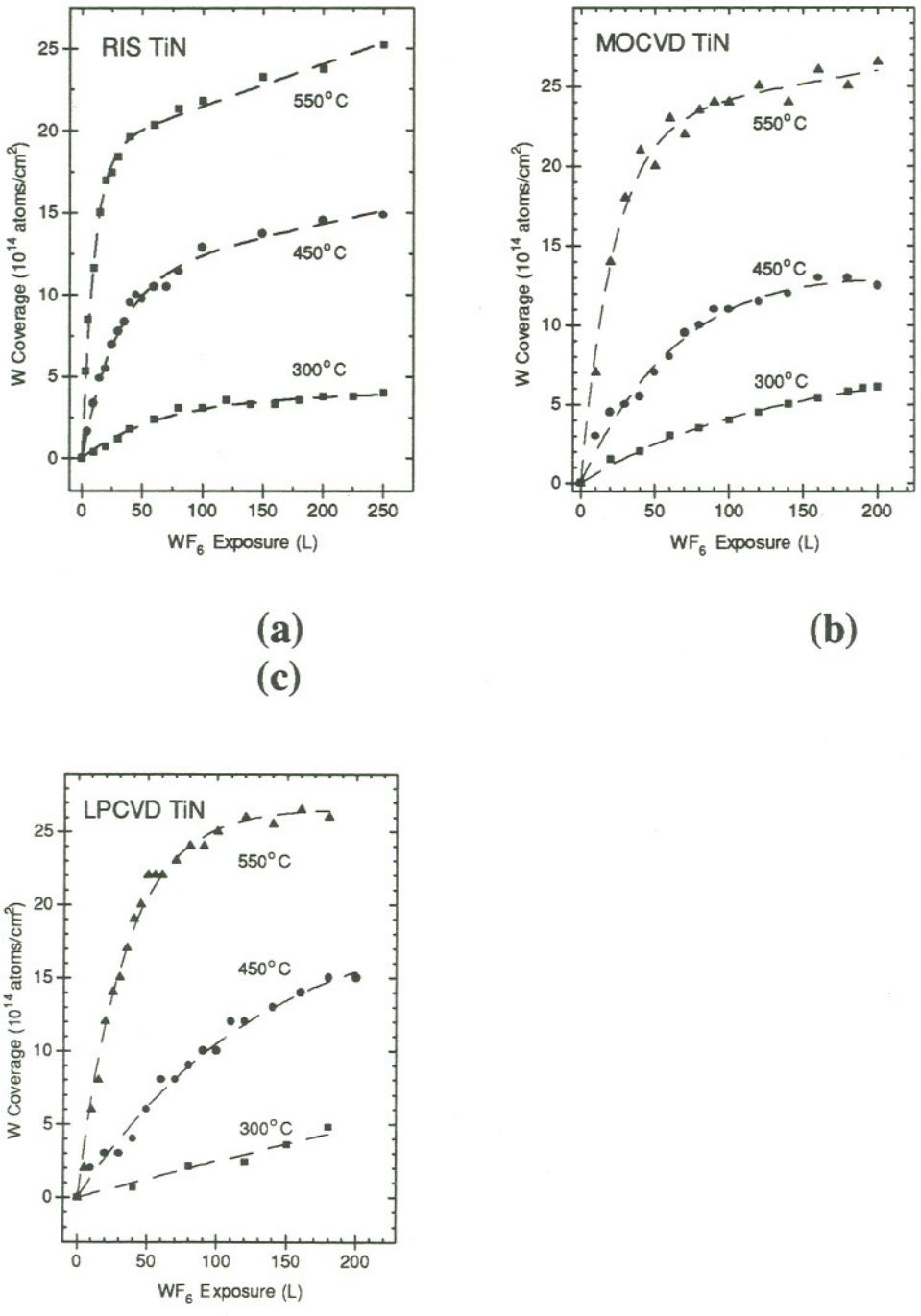


Figure 4-16. W coverage on TiN surfaces with no sputter cleaning versus $WF_6$ exposure at 300, 450, and 550 °C. The dashed lines correspond to the fitted kinetic model, Eq. 4.4.

utilizes three fitting parameters corresponding to the initial reaction probability $s_o$, saturation coverage $N_o$ (coverage at which the deposition rate rapidly begins to decrease), and the effective final reaction probability $s_f$. The kinetics model is an extension of the classical Langmuir localized adsorption model [29,30] in which the deposition rate decreases in proportion to the amount of W deposited. Alternative choices of this model are discussed in Section 4.7.4, where it is explained that there are several approaches that could be applied to the analysis of the experimental data. The starting equation for this simple model can be written as [31]

$$\frac{dN}{dt} = s_o \cdot F \cdot (1 - \frac{N}{N_o}) \tag{4.2}$$

where N is W coverage (atoms/cm$^2$), F is the incident gas molecular flux (molecules/cm$^2$·sec), $s_o$ is the reaction probability, and $N_o$ is the number of available adsorption sites or the asymptotic coverage at which the deposition rate falls to zero. Integrating Eq. (1) gives

$$N(t) = N_o \cdot (1 - e^{-s_o \cdot F \cdot t / N_o}) + A \cdot t \tag{4.3}$$

where a linear term has been added to account for the observed non-zero final deposition rate and, as discussed below, describes how W deposition continues beyond the initial layer. Since all exposures were carried out at a constant molecular flux rate F, the time variable was proportional to total exposure and the equation can be written

$$N(\xi) = N_o \cdot (1 - e^{-s_o \cdot \xi / N_o}) + s_f \cdot \xi \tag{4.4}$$

where the variable $\xi$ represents the gas exposure in Langmuirs (or molecules/cm$^2$) and $s_f$ is the final reaction probability. Eq. (3) was used in the fitting routines with the experimental data. Three independent parameters, $N_o(T)$, $s_o(T)$, and $s_f(T)$ were fit to the data with an iterative least squares fitting routine [32] used independently for each temperature. A physical interpretation of each of these three parameters is presented below. The best-fit results of the model parameters are shown below in Table 4-I.

| | 300°C | 400°C | 450°C | 500°C | 550°C |
|---|---|---|---|---|---|
| **RIS** | | | | | |
| $s_o$ | 0.003 | 0.008 | 0.040 | 0.065 | 0.146 |
| $N_o$ | 3.6 | 6.1 | 11.2 | 13.0 | 18.9 |
| $s_f$ | 0.002 | 0.008 | 0.016 | 0.020 | 0.026 |
| **MOCVD** | | | | | |
| $s_o$ | 0.006 | 0.017 | 0.022 | 0.055 | 0.102 |
| $N_o$ | 6.44 | 11.31 | 16.69 | 20.47 | 22.78 |
| $s_f$ | -- | -- | -- | -- | 0.003 |
| **LPCVD** | | | | | |
| $s_o$ | 0.0017 | 0.012 | 0.018 | -- | 0.078 |
| $N_o$ | 9.9 | 13.6 | 20.4 | -- | 29.8 |
| $s_f$ | -- | -- | -- | -- | -- |

Table 4-I. Numerical values of the kinetic model parameters for the initial $WF_6$ + TiN reaction. $N_o$ is in units of $10^{14}$ atoms/cm$^2$. $s_o$ and $s_f$ are dimensionless.

The numerical values for $N_o$ verify the observations stated above, *i.e.* the saturation levels increased with temperature and were different on the three TiN substrates. This is further illustrated in Fig. 4-17 which plots $N_o$ versus temperature for all three substrates. The $N_o$ values increased in order with the roughness, or the effective surface areas of the three films. The smoothest film, RIS TiN, had the lowest saturation values and the roughest film, LPCVD TiN had the highest $N_o$ values. It thus appears that the saturation effect is a function of effective surface area. The increase of $N_o$ with temperature suggests that the $WF_6$ reaction is thermally activated, and is discussed further in the discussion section.

The initial reaction probabilities followed an exponential temperature dependence. The data in Table 4-I are compared on an Arrhenius plot in Fig. 4-18. Here, the initial reaction probabilities, $s_o$ are plotted on logarithmic scale against inverse temperature. Error bars are shown for two of the points indicating the typical uncertainty associated with a 95% confidence level fit to the data. With the data plotted this way, the activation energies $E_a$ are represented by the straight line fit through the data according to the Arrhenius expression,

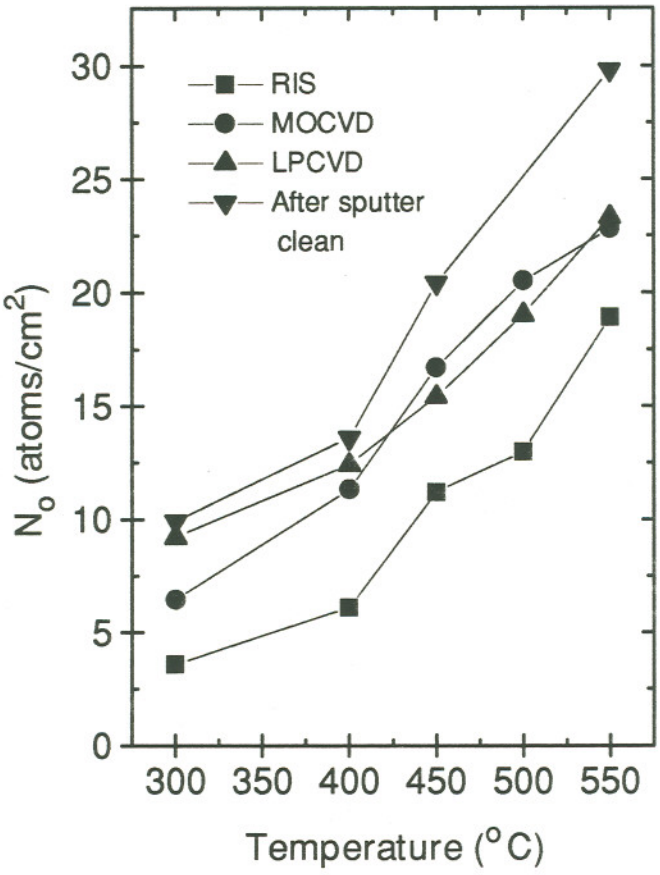


Figure 4-17. Saturation coverage parameter for RIS, MOCVD, and LPCVD TiN as fitted to $WF_6$ reaction kinetics data. Data for TiN surfaces with pre-sputter cleaning are also shown.

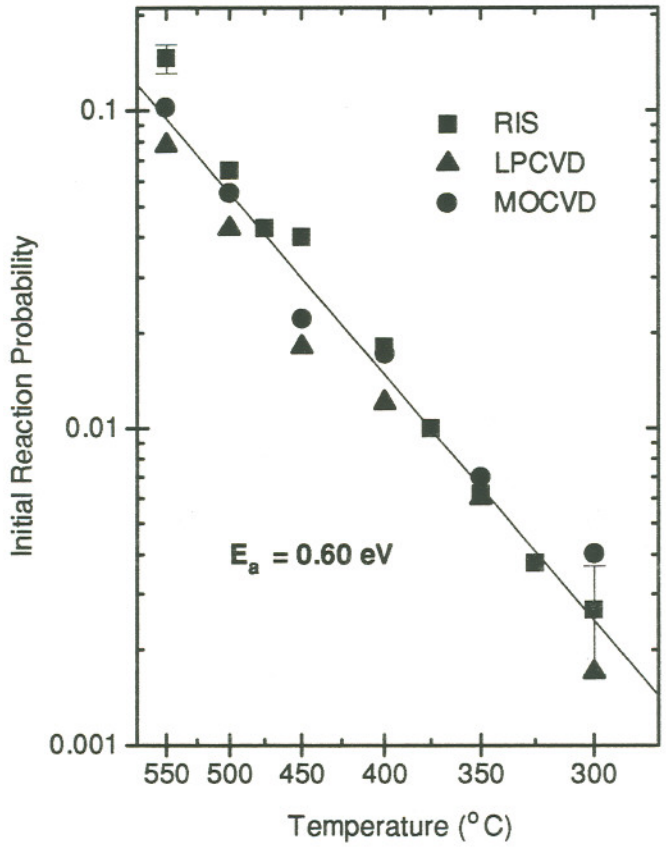


Figure 4-18. Arrhenius plot of initial reaction probability versus substrate temperature for RIS, MOCVD, and LPCVD TiN surfaces. An apparent activation energy of 0.60 eV is shown by the straight line.

$$s_{oi} \propto e^{-E_a/RT_i} \qquad (4.5)$$

The substrate temperature is given by $T$ and $R$ is the universal gas constant. These lines, shown in the Fig. 4-18 were obtained by a least squares fitting routine, and give $E_a$ values of 0.62, 0.60, and 0.54 eV for the three TiN substrates. The uncertainties in the activation energy values were about 16% indicating that the three values were not significantly different from one another. The uncertainties were estimated by summing the squares of the relative uncertainties in temperature and reaction probabilities according to the Arrhenius expression,

$$E_a = \frac{RT_1T_2}{T_2 - T_1} \ln\left(\frac{s_{o1}}{s_{o2}}\right) \qquad (4.6)$$

The "final" reaction probability parameter, $s_f$ used in the model fit indicates that the $WF_6$ reaction does completely saturate at this range of $WF_6$ exposures. The deposition rate of W does not approach zero, but rather some finite value that appears to increase with temperature. It would be difficult to apply any kinetic significance to this parameter, considering that it is obtained from data that represents such a short extent of the reaction. It does appear however, that this continued W deposition is thermally activated since the final reaction probability increases with temperature.

### 4.4 $WF_6$ + TiN with pre-cleaning

The reaction of $WF_6$ with sputter-cleaned TiN was also studied, in order to better understand the influence of surface preparation on the initial reactions. The reactivity of the TiN substrates with $WF_6$ was greater when an in situ Ar sputter clean was used. Fig. 4-19 shows the W uptake on sputter-cleaned RIS TiN versus $WF_6$ exposure for substrate temperatures of 300, 450, and 550 °C. In contrast to the data in Fig. 4-16, the initial reaction probability of $WF_6$ was relatively insensitive to temperature. After 5-10 L a temperature dependence was evident in that more W was deposited at higher temperatures. From 10 to 40 L the reaction probability (rate of W deposition) was approximately linear and increased with temperature.

There was not much difference in the reactions with the CVD TiN substrates after sputter cleaning. Fig. 4-20 shows how the uptake of W compares at 500 °C and 300 °C for the three substrates with in situ sputter cleaning. The uptake of W on the three substrates is roughly the same in that the deposition reaction occurs at the same rate throughout the 50 L range of exposures.

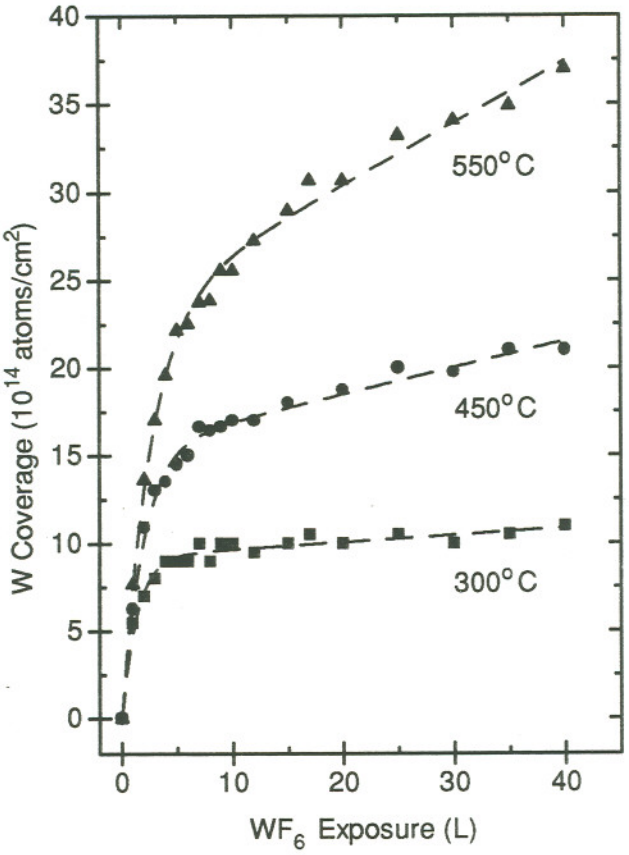


Figure 4-19. Uptake of W on sputter cleaned RIS TiN surfaces at 300, 450, and 550 °C.

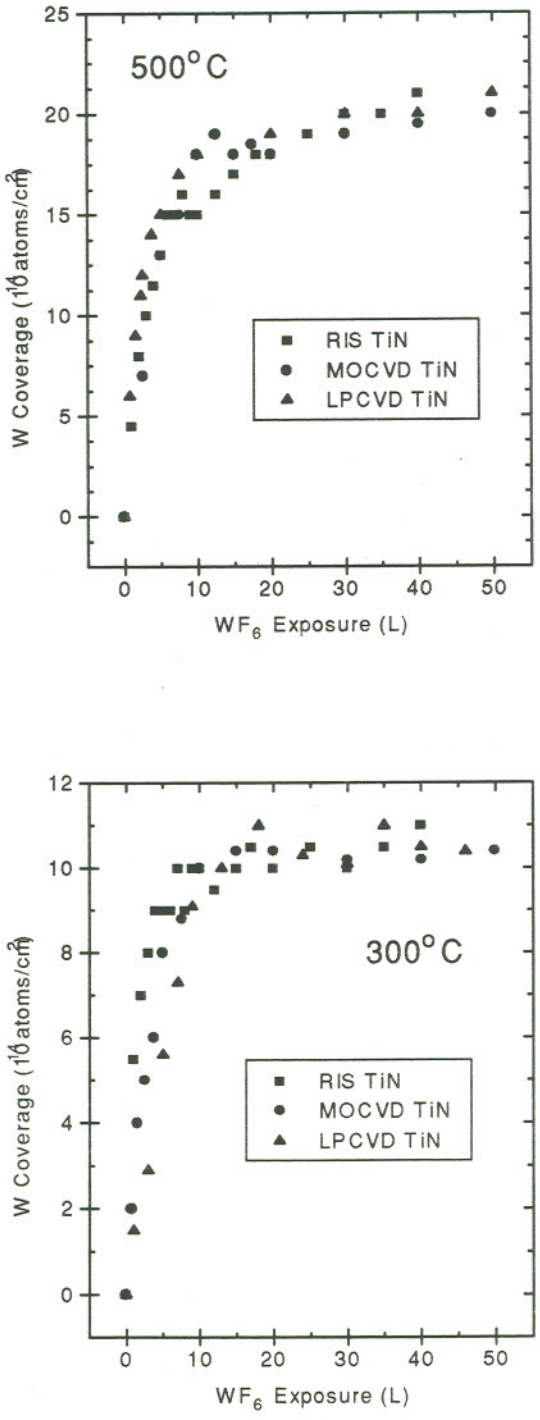


Figure 4-20. W coverage on sputter cleaned TiN surfaces versus $WF_6$ exposure at 300, and 500 ° C. The dashed lines correspond to the fitted kinetic model, Eq. 4-4.

The dashed lines in Fig. 4-19 represent the "best fit" of the same kinetic model used earlier to describe the uptake of W. The initial reaction probabilities are effectively the same throughout the 300-550 °C temperature range. This is further illustrated in an Arrhenius plot in Fig. 4-21. The initial reaction probabilities are effectively the same, and give an average activation energy of 0.4 +/- 0.4 eV. Thus, by sputter cleaning the TiN surface the activation barrier was effectively removed, and the reaction probabilities increased. This could be attributed to the removal of surface O and C contaminants, and/or to the change in surface morphology induced by the sputtering process. Some experiments are described below which address these possibilities.

Fig. 4-17 also compares the values of the saturation coverage parameter $N_o$ after sputter cleaning. The $N_o$ values are consistently higher than without sputter cleaning when compared to the RIS TiN samples. This is similar to the above observation that $N_o$ increased with surface roughness. The $N_o$ values were not much different than those obtained with the MOCVD TiN substrates, and were actually lower than the values obtained with the LPCVD TiN without sputtering.

Further experiments were carried out with the RIS TiN substrates in order to more closely examine the influence of O and C on the initial $WF_6$ reaction. Thermal desorption provided a means of isolating the influence of C on the $WF_6$ reaction. C could be removed from TiN without a significant change in the O surface concentration by quickly ramping the sample temperature to 550 °C for a few seconds. $WF_6$ deposition experiments were performed on surfaces with C/Ti Auger ratios ranging from 0.05 to 0.30 keeping O/Ti ratio fixed at ~ 1. The C/Ti ratio of 0.30 corresponded to an "as received" sample and represented the maximum amount of C seen on the surface. The value of 0.05 corresponded to the minimum amount of surface C that could be attained without significantly changing the relative amount of O on the surface. It was found that neither the $WF_6$ initial reaction probability nor the activation energy was sensitive to the initial amount of C contamination on the RIS TiN surface. Fig. 4-22 shows the initial reaction probability on the annealed sample compared to the untreated TiN at three different temperatures. The initial reaction rates did not change much when the C concentration was varied by a factor of ~ 6. This confirms the observation in Fig. 4-13 , that the C at these concentration levels does not participate in the initial $WF_6$ reaction. It is assumed that the $WF_6$ reactions on MOCVD and LPCVD TiN would behave in same manner.

The initial reaction probability and the associated temperature dependence were sensitive however to the amount of initial oxidation. The surface O concentration was controlled by adjusting the sputtering times to give a range of initial conditions. The surface C was removed much quicker than the O upon sputtering and was about the same for all of these samples. Fig.

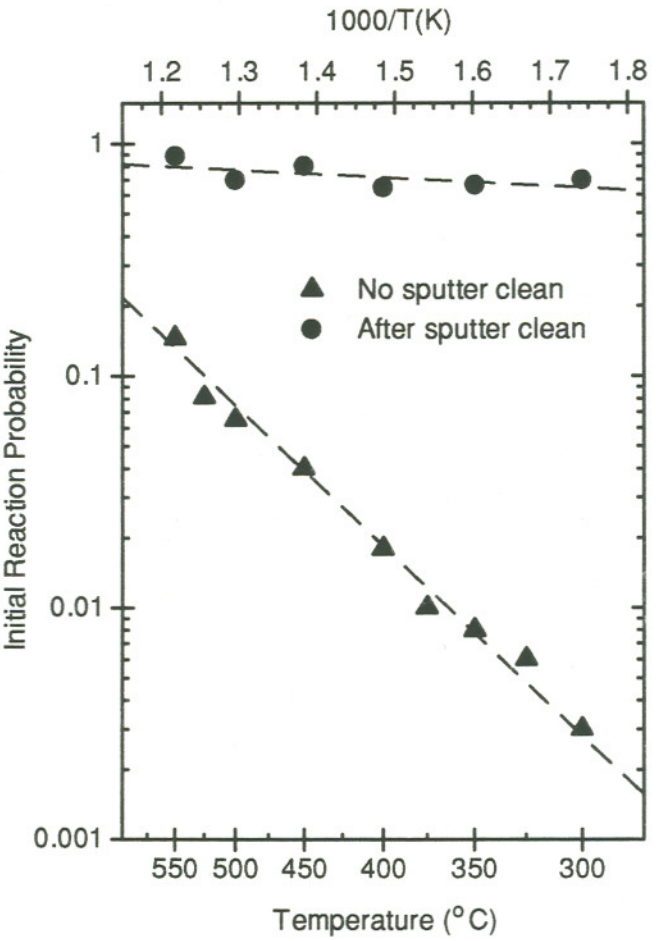


Figure 4-21. Arrhenius plot comparing initial $WF_6$ + RIS TiN reaction probabilities with and without Ar sputter cleaning.

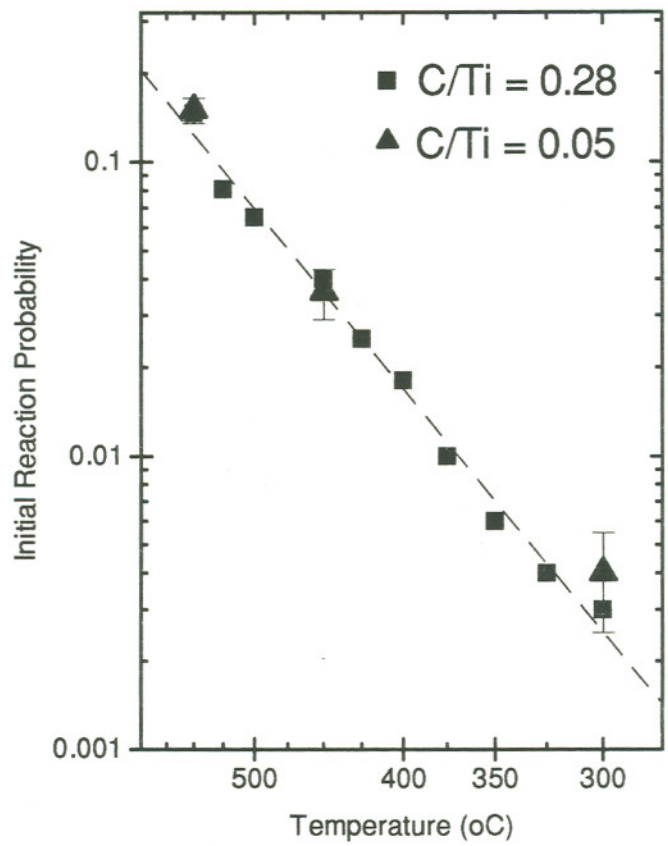


Figure 4-22. Arrhenius plot of initial $WF_6$ + RIS TiN reaction probability versus temperature for different amounts of surface C.

4-23 shows how the activation energy and the 400 °C reaction probability depend on the amount of initial oxidation. As the amount of initial O increases, the reaction probability gradually decreases while the activation energy increases. The amount of initial oxidation therefore directly influences the initial $WF_6$ reactions. This is discussed further in Section 4.7.2.

The similarity of the initial $WF_6$ reaction on the three TiN substrates suggests that small differences in surface morphology do not have much influence on the initial $WF_6$ reaction probability. The grain size distributions as well as the effective surface roughness were noticeably different, but the initial $WF_6$ reaction probability and the activation energy were not significantly different. In order to more closely examine the influence of surface morphology on the $WF_6$ reaction, a RIS TiN sample was prepared as follows. The sample was sputter cleaned for ~ 10 minutes, the typical time required to remove the surface O and C. This sample was then exposed to atmosphere for a few days to allow the surface to become oxidized until the extent of oxidation was about the same as the sample without any cleaning. The $WF_6$ reaction at 300 °C on this sample was then compared to a sample without any sputtering. The main difference between the two samples was therefore the surface morphology, *cf.* Figs. 4-2 and 4-3. The temperature of 300 °C was chosen because if there were any effect at all, it should have been most dramatic at the lower end of the temperature range. This is evidenced in Fig. 4-21 where the influence of sputter cleaning *versus* not is most significant. The reaction probability on the sputter cleaned/re-oxidized sample was close to that for an oxidized sample without any sputter cleaning, which further confirms that the surface morphology has much less of an influence on the initial $WF_6$ reaction than the initial surface O concentration.

Since the LPCVD TiN had an additional chemical contaminant Cl, the influence of Cl on the initial $WF_6$ reaction was investigated. The LPCVD TiN films as-prepared contained about 2 % atomic concentration of Cl, a by-product of the deposition chemistry. The amount of Cl at the surface could be reduced by quickly annealing the sample above 450 °C for a few seconds. The Cl(LMM) transition at 180 eV was reduced to ~ 1/3 magnitude after the anneal. Three samples were pre-annealed before the $WF_6$ exposures to examine how the initial $WF_6$ reaction is affected when the amount of surface Cl is changed. The results are shown in Fig. 4-24, which is an Arrhenius plot that includes three data points corresponding to pre-annealed LPCVD TiN samples. The initial reaction probabilities fall within the scatter of those obtained with the non-annealed

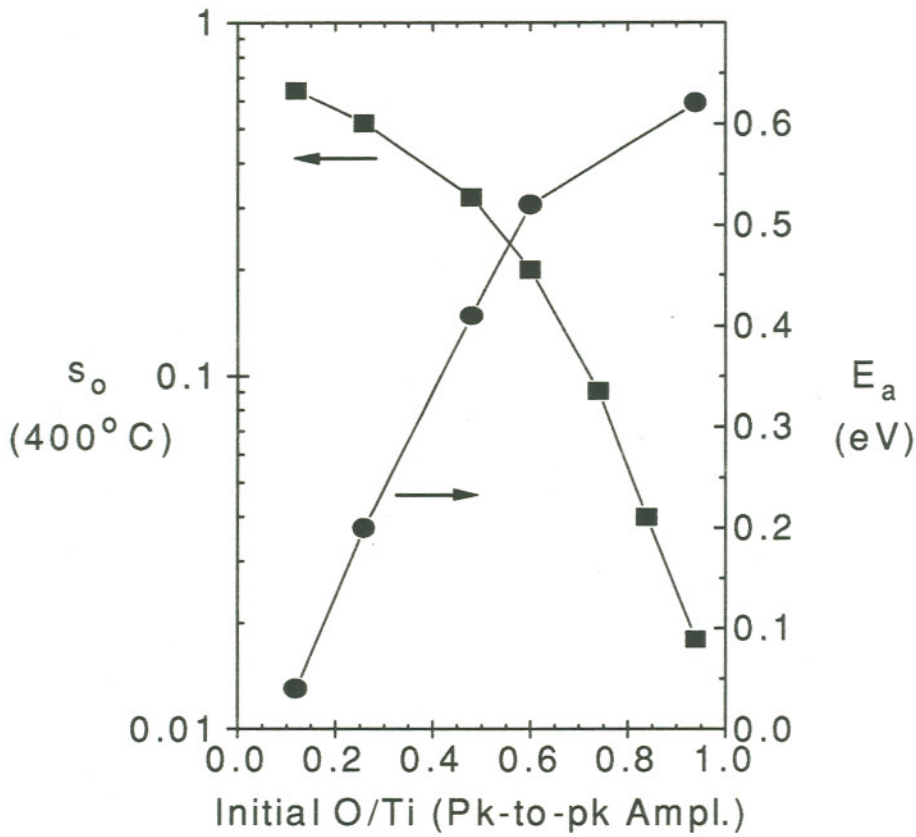


Figure 4-23. Initial reaction probability at 400 °C and average activation energy for the $WF_6$ + RIS TiN reaction versus surface O concentration.

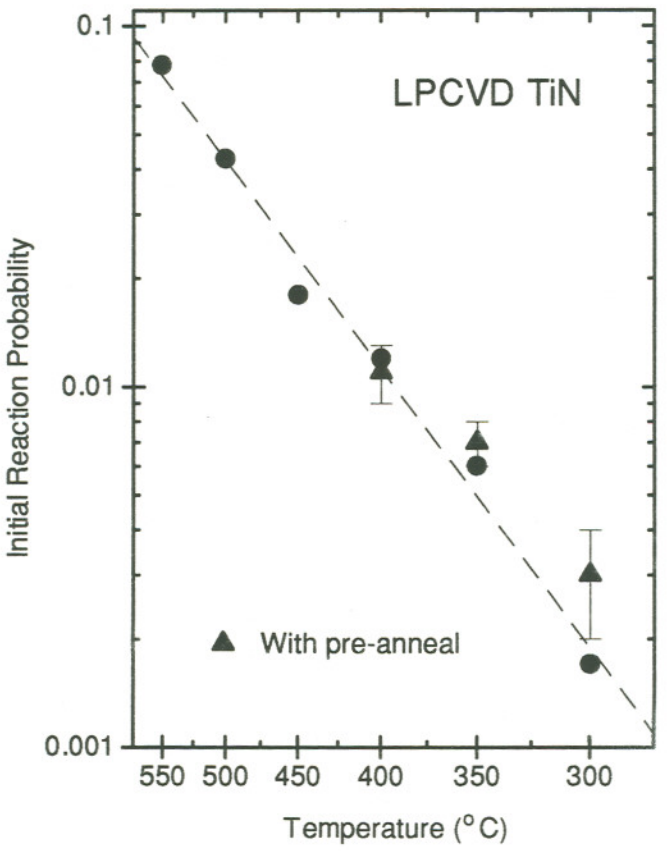


Figure 4-24. Arrhenius plot of initial $WF_6$ + TiN reaction probability versus temperature comparing the effects of a 450 °C pre-anneal. LPCVD TiN substrates were used.

samples, indicating that the surface Cl concentration does not influence the initial $WF_6$ reaction. The data points corresponding to the annealed samples have a slight indication however of a lower activation energy and a higher initial reactivity. This would be expected since the surface Cl would tend to inhibit $WF_6$ decomposition (Cl is not a very congenial electron donor). The annealed samples have less Cl (and O) which allows for easier $WF_6$ decomposition and consequent W deposition.

### 4.5 $SiH_4$ + TiN reactions

The reaction of $SiH_4$ with TiN was examined in order to understand the effects of sequential exposures, or how the reactivity of TiN may be altered by pre-exposing the surface to $SiH_4$. The initial reaction resulted in the deposition of Si. Exposures of about $10^4$ L were required for Si coverages of ~ 1 ML giving reaction probabilities of ~ $10^{-4}$. There was only a slight dependence on temperature from 300 to 550 °C, and only a small increase in the reaction rate was observed when the TiN was sputter cleaned. The amounts of Si deposited were roughly proportional to the exposure time. The influence of O and C on the $SiH_4$ reaction probability was difficult to characterize because of the long exposure times that were required. A 30 kL exposure required ~ 15 minutes, during which time the surface concentrations of O and C decreased significantly from thermal desorption.

The chemical bonding of the deposited Si was sensitive to the amount of TiN oxidation. Fig. 4-25 shows three Auger derivative spectra after 30 kL $SiH_4$ exposures at 450 °C for three different RIS TiN samples. The amount of surface O on the samples was different in each case and was controlled by varying the initial sputtering times. A small Ar peak is observed with Sample C, a result of implantation during sputtering. On Sample A, with the most O, the Si(LVV) peak shape suggests $SiO_2$ bonding, with the two symmetric features at 61 and 76 eV [22]. The Si peak for Sample C is asymmetric with a single negative excursion at 92 eV, which indicates a more covalently bonded species such as Si nitride, silicide or unreacted elemental Si [22,23]. The formation of Ti silicide, however, is not expected at these temperatures. The Si peak shape shown for Sample B appears to be a combination of the types of Si found on Samples A and C. Approximately the same amount of Si was deposited in each case, as estimated from the Si(LVV) peak intensity, corrected for the relative sensitivities of $SiO_2$ and Si [22].

The sensitivity of the $SiH_4$ reaction to temperature is illustrated in Fig. 4-26 which shows the uptake of Si at three different substrate temperatures, 300, 400, and 500 °C. Each of these samples was RIS TiN. The Si uptake is slightly greater at higher substrate temperatures. The difference in rates of Si uptake was almost insignificant compared to the scatter in the data. The

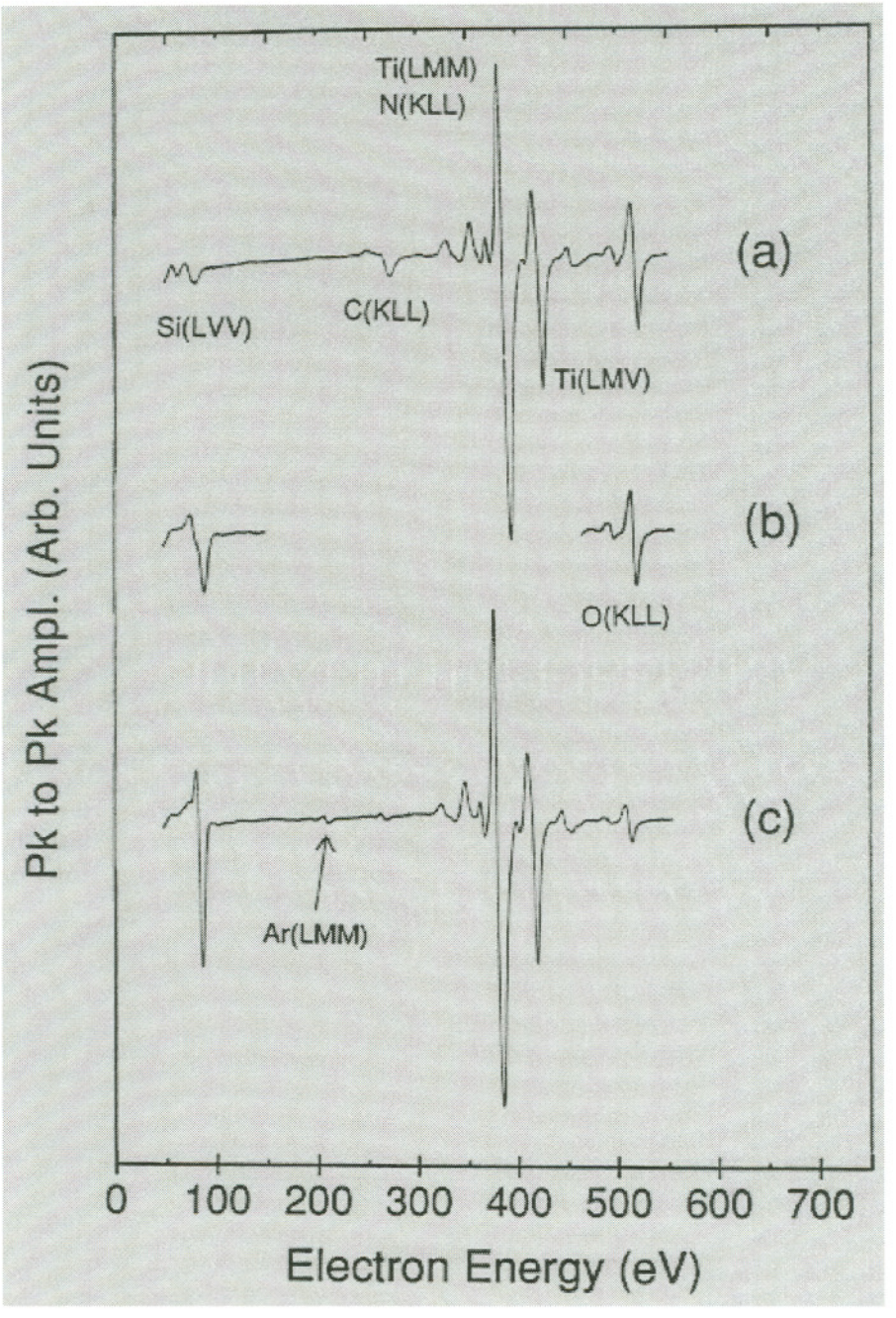


Figure 4-25. Auger derivative spectra from three different TiN surfaces after exposure to 30kL $SiH_4$ at 450°C: (a) no cleaning, (b) and (c) after a sputter clean. The magnitude of the O(KLL) peak near 500 eV indicates the relative amounts of O on the three samples.

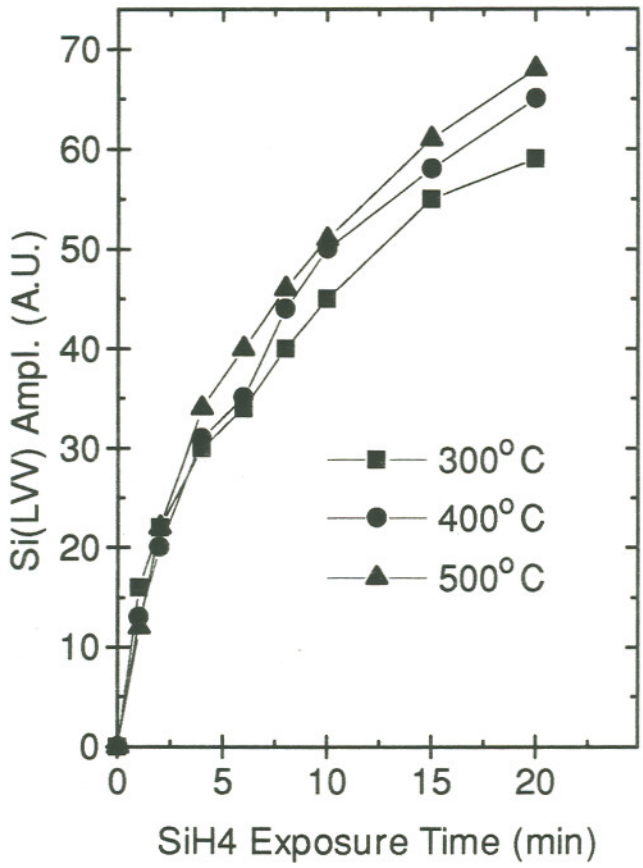


Figure 4-26. Si uptake on TiN surfaces as measured by Si(LVV) peak-to-peak amplitudes at substrate temperatures of 300, 400, and 500 °C.

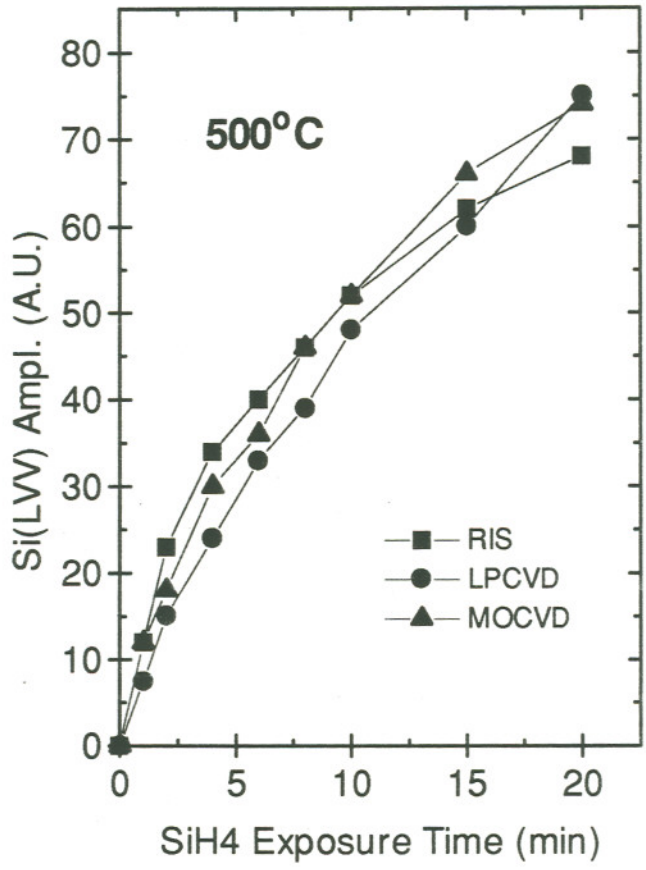


Figure 4-27. Comparison of Si uptake on RIS, MOCVD, and LPCVD TiN surfaces as measured by Si(LVV) peak-to-peak amplitudes at 500 °C.

uptake of Si on the three different TiN films was also compared. Fig. 4-27 shows the Si uptake on the three substrates at 500 °C. The initial $SiH_4$ reaction showed no measurable difference for the three TiN substrates

**4.6 Sequential $WF_6$ and $SiH_4$ reactions with TiN**

When the $WF_6$ exposure was carried out after a $SiH_4$ exposure, Si was consumed from the surface. The rate of W deposition decreased rapidly after the Si was consumed. Fig. 4-28 shows the amplitudes for W(NOO) and Si(LVV) for $WF_6$ exposures at 500 °C that followed a $SiH_4$ exposure. This TiN sample was not pre- cleaned, but was exposed to 30 kL of $SiH_4$ at 450°C and was kept inside the UHV chamber between gas exposures. About 20 L of $WF_6$ were needed to remove the surface Si after which point the deposition rate of W began to decrease. W uptake data for a sample without the $SiH_4$ pre-treatment are shown for comparison. The $SiH_4$ pretreatment has an effect similar to sputter cleaning on the $WF_6$ reaction in that more W is deposited and the initial reaction probability is higher.

Fig. 4-29 shows how the $WF_6$ reactions compare after $SiH_4$ exposures with and without a sputter pre-clean, respectively. The initial reaction probability is greater over the entire temperature range when the TiN was first sputter cleaned. The effective activation energy, however, is the same with or without sputter cleaning, 0.13 ± 0.04 eV. Thus, the $SiH_4$ exposures increased the reactivity of TiN with $WF_6$ when the TiN surface was oxidized, but the reactivity was actually less after a $SiH_4$ exposure if the TiN was first sputter cleaned. The activation energy of 0.13 eV obtained for the $WF_6$ reaction after a $SiH_4$ exposure is close to previous results reported for $WF_6$ reactions with clean Si surfaces [24,25,28]. The magnitude of the initial reaction probabilities $s_o$, 0.1 to 0.6, is consistent with results reported by Yu, *et. al.* [26] and with previous studies of $WF_6$ + Si(100) reactions [28].

The reaction of $SiH_4$ with TiN surfaces after exposure to $WF_6$ was also studied in order to learn more about the interactions of $SiH_4$ and $WF_6$ on the TiN surface during W film growth. During this reaction, some of the surface F was removed and Si was deposited. Fig. 4-30 shows the peak to peak amplitudes for Si(LVV), W(NOO), and F(KLL) during a $SiH_4$ exposure at 450 ° C for a TiN sample that had previously been exposed to 200 L of $WF_6$ at 450 °C. The TiN had not been sputter cleaned prior to $WF_6$ exposure. After ~ 20 L $SiH_4$ the deposition rate of Si decreases and F is no longer removed. The amount of attenuation of the W(NOO) peak after 20 L suggests a ML coverage of Si, and the F/Si ratio at this point is less than unity. An initial reaction probability of 0.06-0.08 is estimated from the data for the $SiH_4$ reaction after a $WF_6$ exposure, which is very close to that reported for $SiH_4$ reacting with a fluorinated W surface, 0.12 ± 0.04 [27].

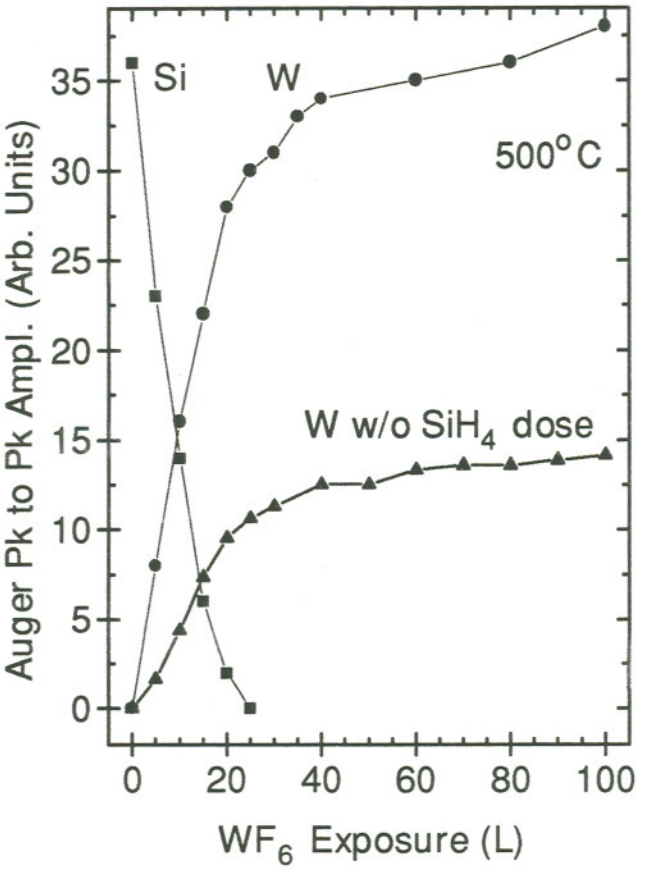


Figure 4-28. Auger peak-to-peak amplitudes for Si(LVV) and W(NOO) from a TiN surface after $WF_6$ exposures at 500 °C performed after the TiN had been exposed to 30kL of $SiH_4$ at 450 °C. The W(NOO) magnitude for a reaction without the $SiH_4$ pre-exposure is shown for comparison.

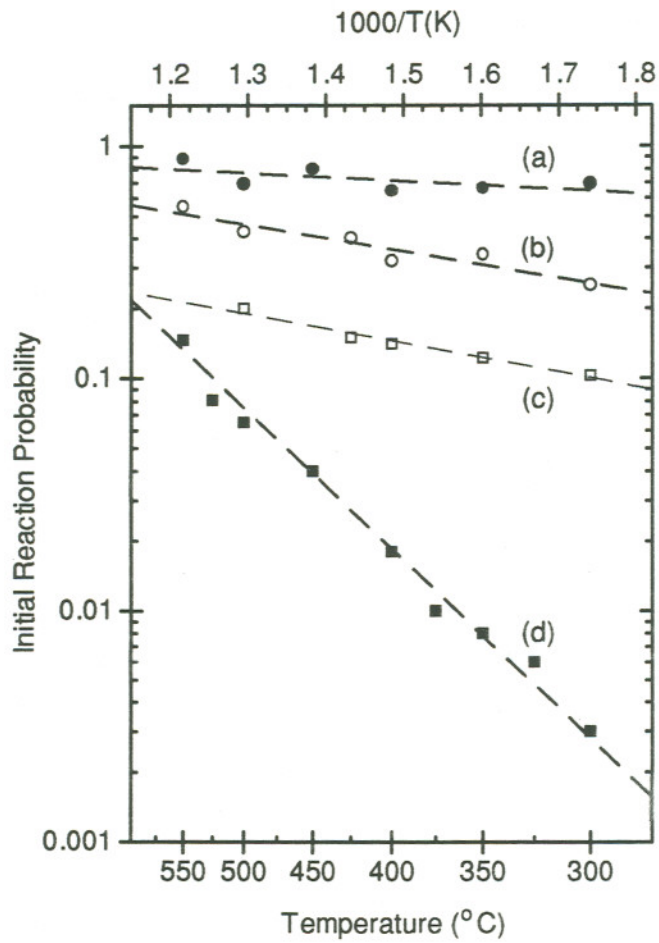


Figure 4-29. Arrhenius plot for the initial $WF_6$ + TiN reaction probabilities, $\theta_S$ for four different initial conditions: (a) after sputter clean, (b) after sputter clean + 30 kL $SiH_4$ exposure at 450 °C, (c) after 30 kL $SiH_4$ exposure at 450 °C, (d) exposed to atmosphere with no cleaning.

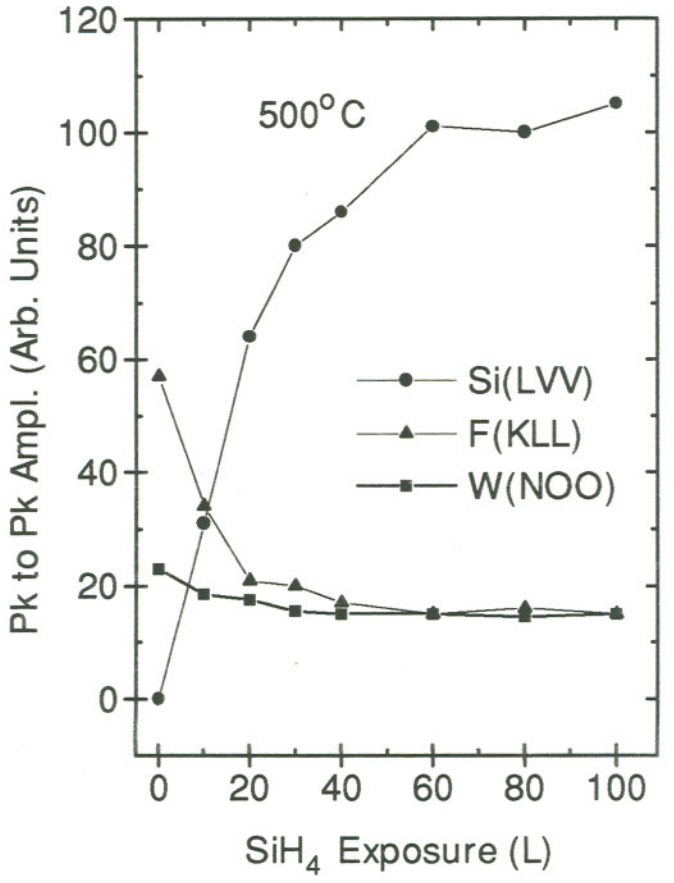


Figure 4-30. Auger peak-to-peak amplitudes for Si(LVV), F(KLL), and W(NOO) from a TiN surface after $SiH_4$ exposures at 500 °C performed after the TiN had been exposed to 200 L of $WF_6$ at 500 °C.

## 4.7 Discussion

### 4.7.1 Reaction pathways

The overall reaction of $WF_6$ with TiN has previously been shown to be [6]

$$WF_{6(g)} + \frac{3}{2}TiN_{(s)} \rightarrow W_{(s)} + \frac{3}{2}TiF_{4(g)} + \frac{3}{4}N_{2(g)} \qquad (4.7)$$

at temperatures above 70 °C. The $WF_6$ adsorbs, dissociates, and decomposes the top layer of the TiN and deposits a layer of metallic W. This reaction clearly cannot proceed beyond a monolayer W coverage unless some type of diffusion is considered. Since the diffusion of $WF_6$ or TiN through a W layer is not very likely at these temperatures [3,10] additional reactions must be considered for continued W deposition, *viz.* $WF_6$ + W(s) and $WF_6$ + $WF_x$(s). These reactions can then continue until the surface becomes saturated with F, at which point the deposition rate of W should be limited by the rate of F removal [34]. When these ideas are applied to the interpretation of our model, $s_o$ is a measure of reaction (4), $N_o$ corresponds to the coverage at which the $WF_6$ + W(s) and $WF_6$ + $WF_x$(s) reactions begin to dominate and the accumulation of F on the surface begins to limit the rate of W deposition. $s_f$ then describes the efficiency of F removal from the surface, which facilitates the continued deposition of W. The removal of F could be *via* $WF_x$ [34] or $TiF_4$ [6] or possibly as $F_2$.

Since the initial and final reaction probabilities are effectively measures of chemical reaction rates, a sensitivity of these parameters to temperature is expected. The variation of $N_o$ with temperature requires explanation. $N_o$ is the number of available adsorption sites for W deposition which normally should not depend on temperature. The effective number of sites however is reduced by the presence of surface F which blocks the adsorption sites. At higher temperatures the removal of F either by thermal desorption or chemical reaction is more favorable, which allows the initial reaction to proceed further, thus giving larger effective values of $N_o$.

### 4.7.2 Surface chemistry and morphology influences on $WF_6$ reactions

The large difference in the behavior of the $WF_6$ reactions with TiN before and after sputter cleaning is attributable to surface oxidation. Fig. 4-23 showed the trend in initial reactivity and activation energy with surface O content, which was varied by removal of O. As the relative amount of oxide was reduced, the $WF_6$ reactivity increased. The oxide reduces the reaction rate presumably by blocking reaction sites, where electrons transfer from the substrate into the $WF_6$ moiety to stimulate decomposition.[35] The sensitivity of the reaction to surface oxidation can be

explained by assuming that multiple reactions are taking place, *viz.* $WF_6$ + TiN, $WF_6$ + $TiN_xO_y$, and $WF_6$ + $TiO_2$. The Ti-O bonds are more ionic and have a higher bond dissociation energy than the Ti-N bonds. The Gibbs free energy for $TiO_2$ is –889 kJ/mole at 600 K, compared to –279 kJ/mole for TiN [36]. The adsorption and dissociation of $WF_6$ molecules has been shown to be inhibited on substrate materials of higher ionic character [35,37]. Therefore, an oxidized TiN surface can be expected to exhibit a reduced reactivity with $WF_6$.

The differences in W uptake on the three TiN substrates are attributed to differences in surface roughness or effective surface area. The surface morphology was shown to have a direct impact affect on the saturation parameter $N_o$, *cf.* Table 4-I. This explanation can also extended to the case of the sputter-cleaned RIS TiN, where the $N_o$ values were consistently higher for the sputter cleaned samples. Sputter-induced changes in surface morphology, as observed in Fig. 4-2 increased the surface roughness and could have created a higher density of surface adsorption sites causing $N_o$ to be higher. The $N_o$ values obtained for the MOCVD TiN films were less affected by sputter cleaning. This is probably because the sputter-induced roughening introduced fewer new adsorption sites on these films, since they were so much rougher initially. The RMS roughness of the RIS film increased from 0.69 to 0.86 nm after sputtering, whereas the CVD films had roughness values of 1.88 and 2.11 nm without any sputtering. The decrease in $N_o$ values observed with the LPCVD TiN samples suggest that the sputtering process effectively decreased the number of available adsorption sites.

### 4.7.3 W Thin Film Growth Modes

When simple kinetics are assumed with a constant sticking coefficient, Auger uptake data can be used to discern between different type of thin film growth modes. Examples of growth modes are shown in Fig. 4-31. The Frank-van der Merwe (FM) mode [39] assumes a layer-by-layer growth of the adsorbate whereby the first layer is completed before the second layer begins. In this case, the interaction favors wetting of the surface by the adsorbate, and surface diffusion of the adsorbed species is required. The rate of adsorption in this case must be slow enough to allow the equilibrium phase to form, otherwise the growth mode would become random, *vide infra.* The Volmer-Weber (VW) mode [40] in Fig. 4-31(b) shows the adsorbate growing in small clusters or islands. Fig. 4-31(c) shows the Stransky-Krastanov (SK) growth mode [41], where clustering occurs after a complete monolayer is deposited. The VW and SK modes also assume a high surface mobility of the adsorbed species and require the adsorption rate to be slow so the less favorable substrate-adsorbate bonding can give way to the more favorable adsorbate-adsorbate

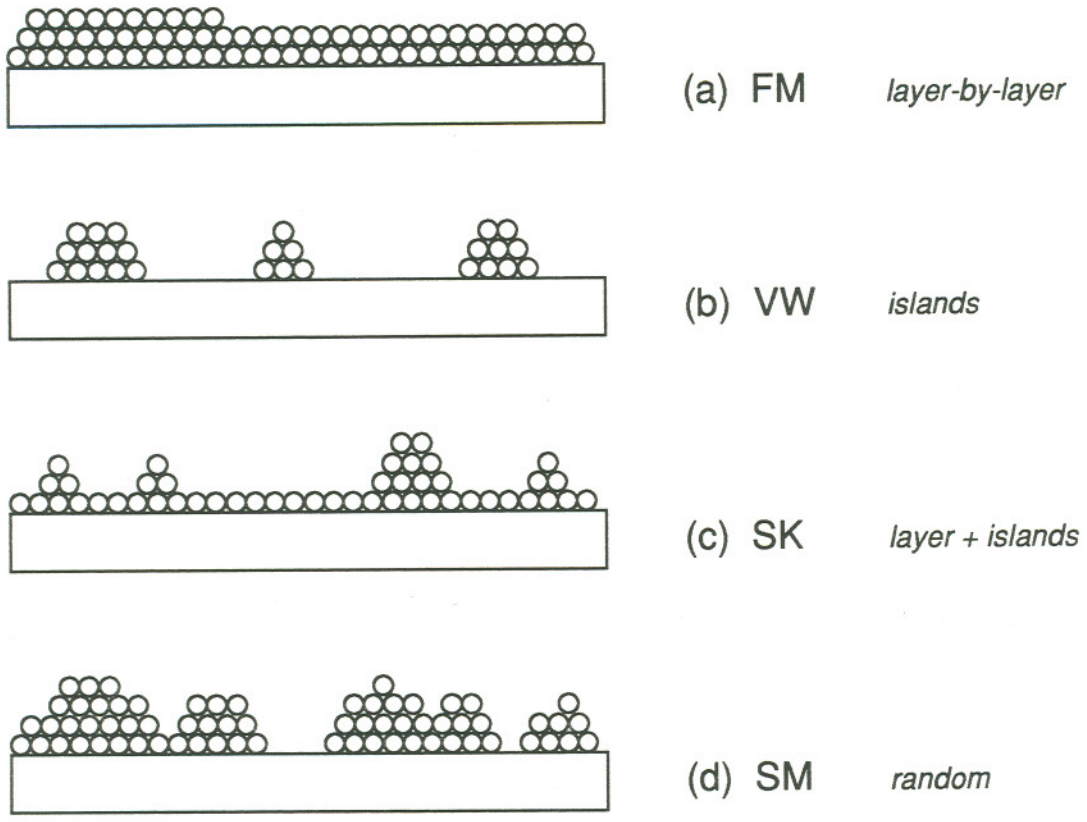


Fig. 4-31. Thin film growth modes, (a) Frank-van der Meere layer-by-layer growth, (b) Volmer-Weber island growth, (c) Stransky-Krastinov layer + islands, and (d) Poisson or random simultaneous multilayer growth.

bonding. The growth mode depicted in Fig. 4-31(d) corresponds to a random deposition where the adsorbates do not have appreciable surface mobility. This mode has been called simultaneous multi-layer (SM) growth [42], or the Poisson mode since the rate of surface coverage follows a Poisson statistical distribution [43]. The SM mode is more likely to occur when surface diffusion of the adsorbate is negligible compared to the rate of adsorption.

The expected substrate and adsorbate Auger signals for these growth modes are shown in Figs. 4-32 and 4-33. Here an island surface coverage of 50 % is assumed for the VW and SK modes. The scales on the plots have been normalized for convenience as follows. The substrate Auger signal intensity is set to unity for a clean surface, and the adsorbate signal is set to unity for a coverage of one monolayer. The horizontal axis in each plot is expressed as "amount deposited" in units of equivalent monolayers which was chosen for convenience in constructing the equations. These plots make no assumptions about the adsorption kinetics, only the strengths of the substrate and adsorbate Auger signals.

An adsorption system consisting of W overlayers on a TiN substrate was used in constructing these plots. The substrate Auger signal strengths depend on the attenuation coefficient $\alpha$ which represents the attenuation of the Auger signal passing through a monolayer of adsorbate. An estimate of $\alpha$ was made according to the equation [44],

$$\alpha = e^{-\frac{d}{\lambda \cos\beta}} \qquad (4.8)$$

where $\lambda$ is the inelastic mean free path for the emitted Auger electrons, d is the overlayer thickness, and $\beta$ is the angle of instrument detector (measured from normal). An estimate for $\lambda$ was obtained by using the universal expression [45],

$$\lambda(E) = 1430 \cdot E^{-2} + 0.54 \cdot E^{1/2} \qquad (4.9)$$

where E is the kinetic energy of the detected Auger electron. The thickness of a single W overlayer was estimated to be equal to the twice the covalent radius of a W atom, i.e. 2.60 Å [46]. An instrument factor of 0.74 was used for the cos($\beta$) term in eq. (4.8) which is typical for CMA systems.

The actual equations used in plotting the curves in Figs. 4-32 and 4-33 can be found in a number of excellent review publications [47-49] and will not be repeated here. The curves are

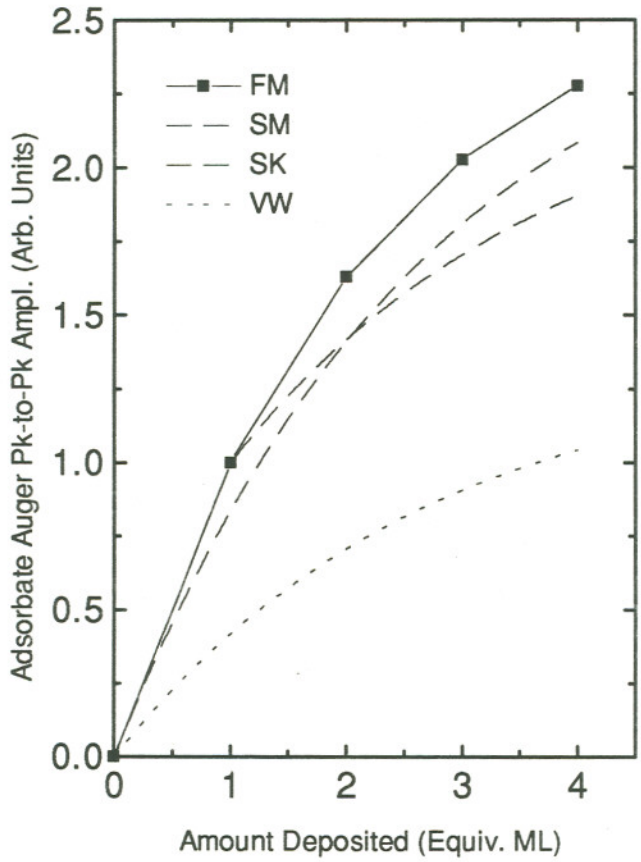


Fig. 4-32. Adsorbate Auger signal versus amount deposited for the different thin film growth modes:

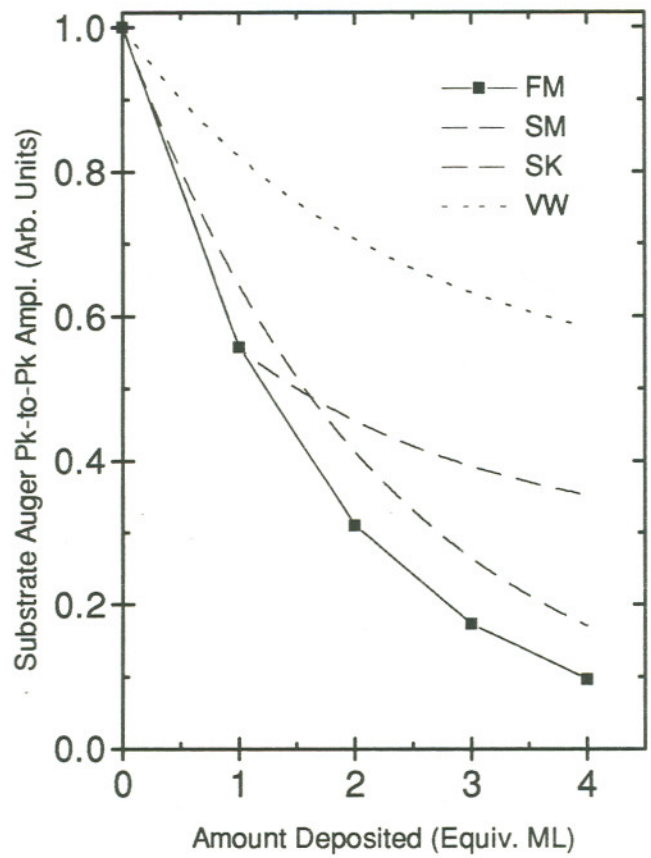


Fig. 4-33. Substrate Auger signal during different thin film growth modes:

essentially exponential with the exception of the FM curves which are straight line segments whose end points follow an exponential envelope.

Fig. 4-34 shows the W(NOO) and Ti(LMV) Auger amplitudes from a TiN surface after sequential exposures to $WF_6$ . The TiN substrate was held at 400 °C during the $WF_6$ exposure. The substrate signal quickly drops from about 80 units to less than 60 units, corresponding to a ~ 25% decrease. For a uniform complete monolayer coverage of W, the expected decrease in the Ti(LMV) signal would be 61%, using eq. (4.1). The absolute W coverage at this point was approximately $2x10^{15}$ atoms/cm$^2$, *cf.* Fig. 4-20. This coverage is close to the surface atomic density of a W crystal, and also close to that of a TiN crystal [46]. This implies that the absolute W coverage is a few equivalent monolayers. Since the substrate signal decreases by the amount expected for a complete W monolayer coverage, the Volmer-Weber thin film growth mode is unlikely. Fig. 4-33 shows that after deposition of only a few equivalent monolayers, the substrate signal in a low coverage (island coverage < 50 %) VW mode will not decrease as much as was observed with the experimental data. Therefore, the thin film growth mode in this case is more likely FM, SK, or SM. The FM and SK modes require a high degree of surface mobility of the W atoms in order to form a complete, uniform monolayer. Since previous studies [37] and theoretical models [33] have shown a low probability for W surface diffusion, the SM mode is the most likely growth mode for the $WF_6$ + TiN reaction in this case.

A clear distinction between the FM, SK, and SM modes is not possible for several reasons. The data has a relatively high amount scatter due to surface inhomogeneities such as polycrystallinity and due to influence of the electron beam with the surface chemistry. There is also no unambiguous method for defining what absolute coverage corresponds to an equivalent "monolayer" coverage.

### 4.7.4 $WF_6$ Adsorption Kinetic Models

The rate of adsorption of a gas phase species on a solid surface, $r_a$ can be expressed as,

$$r_a = s(\theta) \cdot F \qquad (4.10)$$

where $s(\theta)$ is the sticking coefficient which may depend on adsorbate coverage $\theta$, and F is the incident gas flux. This equation is an adsorption isobar since a constant background pressure is assumed. To simplify the chemisorption rate equations, $\theta$ is usually defined for $0 < \theta < 1$ where

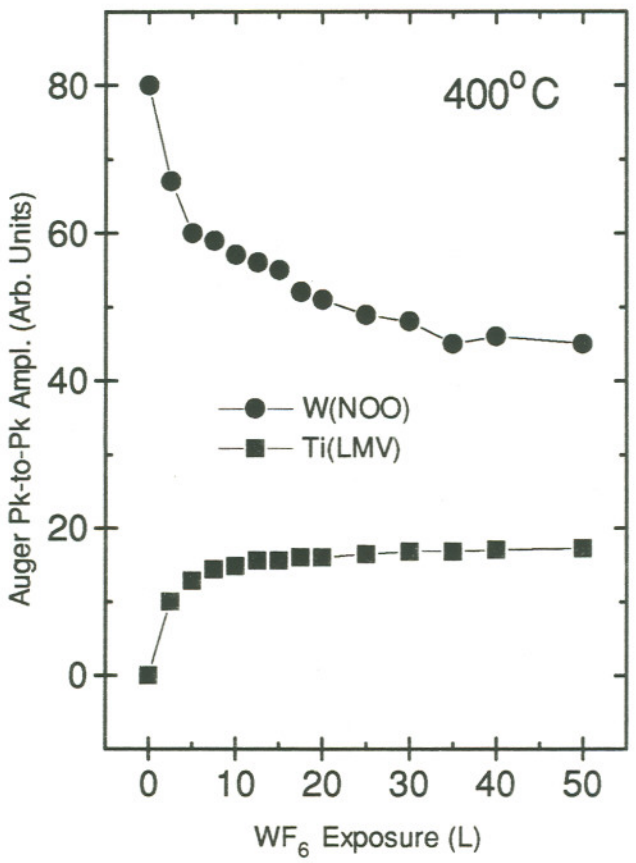


Fig. 4-34. W(NOO) and Ti(LMV) Auger amplitudes from a TiN surface after sequential exposures to $WF_6$ at 400 °C.

$\theta = 1$ corresponds to an upper limit to adsorbate coverage, or *saturation* coverage, typically one monolayer.

For non-dissociative, direct adsorption with no interaction between adsorbates,

$$s(\theta) = s(0) \cdot (1 - \theta) \tag{4.11}$$

which is essentially the Langmuir adsorption model [30]. This model assumes that there are a fixed number of identical adsorption sites each of which can accommodate a single adsorbed species. It also assumes that there are no interactions of gas phase species with occupied adsorption sites, and that there are no lateral interactions between adsorbed species or surface diffusion of adsorbed species. This model further assumes that the adsorption is localized in that adsorption sites are filled only by direct collision with gas phase species, and direct meaning that any metastable precursor or intermediate adsorption phases are ignored. Although most of these restrictions are unexpected for the $WF_6$ + TiN reaction, the Langmuir model does serve as a useful starting point for modeling different adsorption kinetics.

The adsorption process could also be dissociative, in that upon contact with the surface the adsorbate dissociates into two or more constituents that require adsorption sites of their own. For the simplest case of direct dissociative adsorption, two adjacent vacant adsorption sites are required. The sticking coefficient can be expressed [53] as

$$s(\theta) = s(0) \cdot (1 - \theta)^2. \tag{4.12}$$

This equation also assumes that the adsorption is direct and that no lateral interactions of the adsorbates occur. An example of this type of adsorption is $O_2$ adsorption on CuO [51,52]. The behavior of $s(\theta)$ for these two non-interacting direct adsorption models are shown as curves (a) and (b) in Fig. 4-35. The experimental behavior for the $WF_6$ + TiN reaction follows the behavior indicated by curve (c) which has the same basic shape as the $s(\theta)$ curve for dissociative adsorption. The experimental data differs from both curves (a) and (b) however in that $s(\theta)$ does not approach zero, but seems to approach a finite value. This suggests one of two possibilities, that the reaction does proceed via dissociative adsorption and $\theta$ has not yet reached the value of unity, or that the model is still inadequate. More details with the kinetic model are explored below.

When adsorption occurs *via* a precursor state, two rate constants need to be considered,

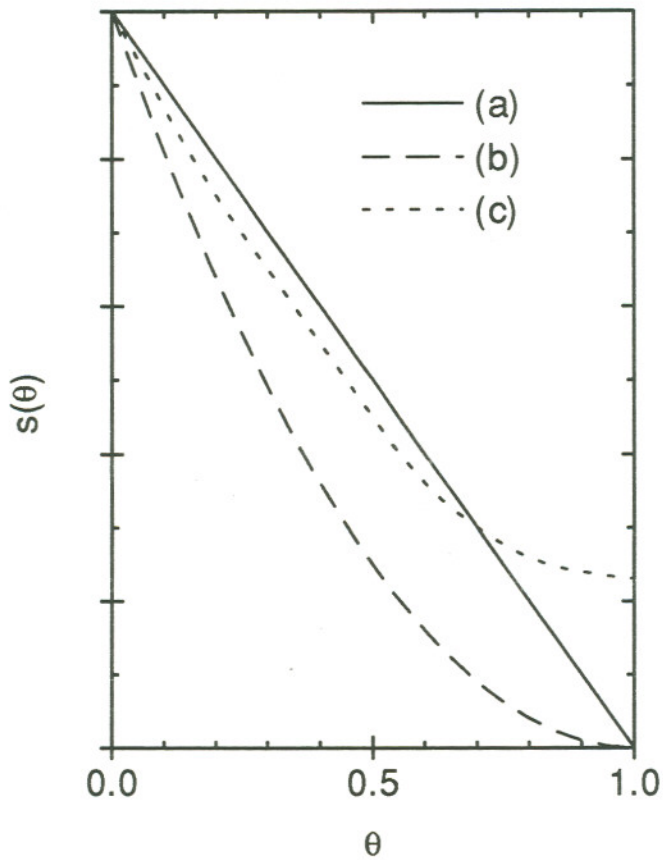


Fig. 4-35. Behavior of sticking coefficient verus adsorbate coverage for (a) simple Langmiur adsorption model, (b) dissociative adsorption model,and (c) experimental data from the $WF_6$ + TiN reaction.

$k_a$ = rate constant for precursor to final chemisorbed state

$k_d$ = rate constant for desorption from the precursor state.

The sticking coefficients for adsorption through precursor states can be expressed as [53],

$$s(\theta) = s(0)\frac{(1+K)(1-\theta)}{1+K(1-\theta)} \tag{4.13}$$

for non-dissociative, and

$$s(\theta) = s(0)\frac{(1+K)(1-\theta)^2}{1+K(1-\theta)^2} \tag{4.14}$$

for dissociative adsorption, with $K \equiv k_a/k_d$. An example of this is $O_2$ adsorption on Ag(110) [54]. The $O_2$ molecule adsorbs onto the surface, then can either dissociate into two separate O atoms, or desorb from the surface. Fig. 4-36 compares $s(\theta)$ expressions of direct and indirect adsorption. For adsorption with a significant precursor state, *i.e.* $K > 0$, the sticking coefficient is higher throughout most of the $\theta$-range, but still approaches zero when $\theta \rightarrow 1$. Since the experimental data has no way of identifying any intermediate adsorption phases, the assignment of numerical values to constant K for the purpose of modeling would be fruitless. The kinetic data itself simply cannot be used to determine whether $K = 0$ or $K \neq 0$.

Even more complexity can be introduced into the model by considering the effects of lateral interactions of the adsorbates. Here the energy of the lateral interaction must be considered in terms of its magnitude and whether it is an attractive or repulsive interaction, and also how many adsorbate neighbors are involved in the interaction. The adsorption rate expression must then be summed over a probability distribution for occupancy by neighboring sites as well as availability of vacant sites [53]. The resulting expressions for $s(\theta)$ are similar to that observed for adsorption via precursor states with some subtle differences in the shapes of the curves. The results, which are not presented here, are developed in detail by Zhdanov [31] and King and Wells [55], and are reviewed and discussed by Lombardo and Bell [52]. Again, the kinetic data is not precise enough to distinguish among the many possible variations of interactive and non-direct adsorption.

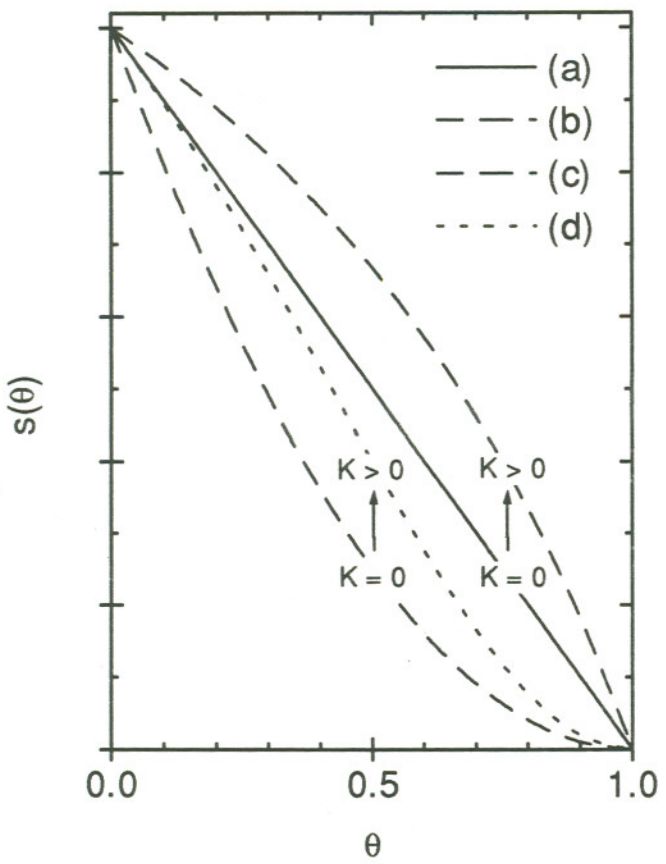


Fig. 4-36. Behavior of sticking coefficient versus adsorbate coverage for direct, K = 0, and indirect , $K \neq 0$ models for both dissociative and non-dissociative adsorption.

All of the models thus far have assumed surface homogeneity, *i.e.* all of the adsorption sites were chemically and physically identical. A more sophisticated modeling approach would have to allow for surface heterogeneity. One of the most common ways of addressing this issue is to assume that the surface can be modeled by a group of adsorption sites that span a range of adsorption energies, or effective activation energies.

A general starting equation for such an analysis is [29],

$$R(t) = \int_{\Delta} r(t,E) \cdot \chi(E) \cdot dE \qquad (4.15)$$

where r(t,E) is the local rate of adsorption on sites with activation energy E and $\chi(E)$ is the probability distribution function for the range $\Delta$ of activation energies spanned by all of the adsorption sites. For a uniform surface that can be characterized by a single activation energy, $\chi$ (E) is a Dirac delta function $\delta(E-E_a)$. An analysis based on the initial assumption of surface heterogeneity would have to begin such an equation. The kinetic data for the $WF_6$ + TiN reaction is not precise nor complete enough to distinguish among the subtle differences that surface heterogeneity modeled in this way would introduce.

If there is a distribution of activation energies, one usually [50] arrives at the Elovich equation,

$$s(\theta) = A \times e^{-B \times \theta} \qquad (4.16)$$

where A and B are constants. There are several theories that all lead to the Elovich equation. One theory is that the adsorption kinetics are controlled by diffusion-limited electron transfer from the substrate. This is possible in the case of the $WF_6$ + TiN reaction, where electron transfer is suspected of being an important factor in $WF_6$ adsorption [35].

A number of different theories can be applied to the kinetic data, but the precision of the data is not high enough to distinguish among several possibilities including: dissociative adsorption, dissociative adsorption *via* precursor states with or without lateral interactions of adsorbates. The adsorption could also have been modeled using an equation of a type similar to eq. (4.16), but there would be an ambiguity in the interpretation of the fitting constants because several approaches could be used where the constants represent different physical quantities.

### 4.7.5 Interpretation of $SiH_4$ reactions

Yu, *et. al.* [6] performed studies under UHV conditions of the $SiH_4$ reaction with TiN films prepared via ammonia nitridization of sputter cleaned Ti, sputtering of TiN targets, and nitridization of Ti-Si films. Using a UHV prepared film, a 5000 L exposure of $SiH_4$ at 300 °C deposited $4x10^{14}$ Si atoms/cm$^2$ on a TiN surface prepared in UHV, which gives a reaction probability roughly equivalent to our value of $10^{-4}$ on a sputter cleaned reactive ion sputtered TiN film. *In situ* XPS analysis of the same UHV films showed that the deposited Si was mostly unreacted elemental Si, with a small component of Si nitride [6]. Conversely, on an oxidized TiN surface the Si was bound to the O with both $SiO_2$ and suboxide components. Thus, the AES results presented in this study and the previous XPS studies showed that the $SiH_4$ reaction with TiN was not sensitive to the details of film preparation nor, consequently, to the anticipated range of TiN stoichiometries and crystallographic textures.

The Si deposited from the $SiH_4$ reaction provides a facile pathway for F removal during subsequent $WF_6$ reactions. Both the efficiency of the initial $WF_6$ reaction and the extent of the reaction are greater after a $SiH_4$ exposure, *cf.* Fig. 4-28. Once the Si is consumed, however, the $WF_6$ reaction shows a saturation behavior much the same as for the TiN surface without a $SiH_4$ exposure. This observation supports the interpretation that in the linear growth rate regime film growth is dominated by mechanisms for removal of F from the surface.

The formation of a Si-F layer from the $SiH_4$ reaction after a $WF_6$ exposure was previously studied using a W substrate [56]. The stoichiometry of the Si-F layer was $SiF_x$, with $x < 4$, but this "subfluoride" layer was found to be inert to $SiH_4$. The results in Fig. 4-30 suggest a Si-F layer formation and the $SiH_4$ reaction appeared to saturate after about one monolayer of Si was deposited. Thus even though we begin with a TiN surface, the surface reactions are very similar to those found on W and Si surfaces, after an initial W or Si layer has been deposited.

## 4.8 References for Chapter 4

4-1. J.E.J. Schmitz, "Chemical Vapor Deposition of Tungsten and Tungsten Silicides", Noyes Publications, New Park, NJ, 1992.

4-2. R.V. Joshi, D. Moy, S. Brodsky, A. Charai, L. Krusin-Elbaum, P.J. Restle, T.N. Nguyen, and C.S. Oh, Appl. Phys. Lett. 54, 1672 (1989).

4-3. K. Suguro, Y. Nakasaki, S. Shima, T. Yoshii, T. Moriya, and H. Tango, J. Appl. Phys. 62, 1265 (1987).

4-4. V.V.S. Rana, J. A. Taylor, L.H. Holschwandner, and N.S. Tsai in "Tungsten and Other Refractory Metals for VLSI Applications II", Proceedings of the Materials Research Society, E.K. Broadbent, ed., Pittsburgh, PA (1987) p. 187.

4-5. M.L. Hitchman, A.D. Jobson, L. F. Tz. Kwakman, Appl. Surf. Sci. 38, 312 (1989).

4-6. M.L. Yu, K.Y. Ahn, and R.V. Joshi, J. Appl. Phys. 67, 1055 (1990).

4-7. A. Sherman, Jap. J. Appl. Phys. 30, 3553 (1991).

4-8. P. Singer, Semiconductor International, p. 36 (Aug. 1992).

4-9. S. Kumar, D.R. Chopra, and D.C. Smith, J. Vac. Sci. Technol. B 11(5), 1815 (1993).

4-10. S. Kumar, D.R. Chopra, and G.C. Smith, J. Vac. Sci. Technol. B 10(3), 1218 (1992).

4-11. K. Hashimoto and H. Onoda, Appl. Phys. Lett., 54(2), 120 (1989).

4-12. I. Petrov, L. Hultman, U. Helmersson, J.-E.Sundgren, and J.E. Greene, Thin Sol. Films 169, 299 (1989).

4-13. L. Sorriano, M. Abbate, J.C. Fuggle, P. Prieto, C. Jimenez, J.M. Sanz, L. Galan, and S. Hoffman, J. Vac. Sci. Technol. A 11(1), 47 (1993).

4-14. C. Ernsberger, J. Nickerson, T. Smith, A.E. Miller, and D. Banks, J. Vac. Sci. Technol. A 4, 2784 (1986).

4-15. T.P. Thorpe, S.B. Qadri, S.A. Wolf, and J.H. Claassen, Appl. Phys. Lett. 49(19), 1239 (1986).

4-16. T.P. Thorpe, A.A. Morrish, and S.B. Qadri, J. Vac. Sci. Tehcnol. A 6(3), 1727 (1988).

4-17. M.J. Bozak, Thin Sol. Films 221, 55 (1992).

4-18. M.J. Vasile, A.B. Emerson, and F.A. Baiocchi, J. Vac. Sci. Technol. A 8(1), 99 (1990).

4-19. A. R. Chaourasia and D.R. Chopra, Surf. Sci. Spectra 1, 223 (1992).

4-20. C.D. Wagner, W.M. Riggs, L.E. Davis, J.F. Moulder, and G.E. Muilenberg, "Handbook of X-ray Photoelectron Spectroscopy", Physical Electronics Division, Perkin Elmer Corp., Eden Prairie, MN

4-21. R.I. Hedge, R.W. Fiordalice, E.O. Travice, and P.J. Tobin, J. Vac. Sci. Technol. B 11(4), 1287 (1993).

4-22. L.E. Davis, N.C. MacDonald, P.W. Palmberg, G.E. Raich, and R.E. Weber, "Handbook of Auger Electron Spectroscopy", Physical Electronics Division, Perkin-Elmer Corp., Eden Prairie, MN (1978).

4-23. J.M. Sanz, M. Clement, and J.M. Martinez-Duart, Thin Solid Films 221, 21 (1992).

4-24. J. Wood, Appl. Surf. Sci. 38, 397 (1989).

4-25. D.W. Hess, in "Tungsten and Other Refractory Metals for VLSI Applications", Proceedings of the Materials Research Society, R.S. Blewer, ed., Pittsburgh, PA (1986) p. 105.

4-26. M.L. Yu, B.N. Eldridge, and R.V. Joshi, AIP Conf. Proc. 167, 202 (1988).

4-27. M.L. Yu and B.N Eldridge, J. Vac. Sci. Technol. A 7, 625 (1989).

4-28. S.L. Lantz, W.K. Ford, A.E. Bell, and D. Danielson, J. Vac. Sci. Technol. A 8, 911 (1993).

4-29. M. Jaroneic, Thin Solid Films 71, 273 (1980).

4-30. I. Langmuir, J. Amer. Chem. Soc. 38, 2867 (1916).

4-31. V.P. Zhadnov, Surf. Sci. Rep. 12, 183 (1991).

4-32. MicroCal Inc., 22 Industrial Drive East, Northampton, MA.

4-33. R. Arora and R. Pollard, J. Electrochem. Soc. 138, 1523 (1991).

4-34. J.R. Creighton, J. Electrochem. Soc. 136, 271 (1989).

4-35. H. Itoh, N. Kaji, T. Watanabe, and H. Okano, Jap. J. Appl. Phys. 30, 1525 (1991).

4-36. D.R. Stull and H. Prophet, "JANAF Thermochemical Tables," NSRDS-NBS 37, U.S. NIST (formerly NBS), Washington, D.C. (1971).

4-37. J.A. Yarmoff and F.R. McFreeley, AIP Conf. Proc. 167, 210 (1988).

4-38. E.K. Broadbent and C.L. Ramiller, J. Electrochem. Soc. 131(6), 1427 (1984).

4-39. F.C. Frank and J.H. van der Merwe, Proc. Roy. Soc. (London) A, 198 (1949).

4-40. M. Volmer and A. Weber, Z. Phys. Chem. 199, 277 (1926).

4-41. J.N. Stransky and L. Krastinov, Ber. Akad. Wiss. Wien 146, 797 (1938).

4-42. M.G. Barthes and A. Rolland, Thin Sol. Films 76, 45 (1981).

4-43. A.H. Bowker and G.J. Lieberman, *Engineering Statistics*, 2nd Ed., Prentice-Hall, (1972).

4-44. C. Argile and G.E. Rhead, Surf. Sci. Rep. 10, 277 (1989).

4-45. M.P. Seah and W.A. Dench, Surf. Interface Anal. 1, 2 (1979).

4-46. Handbook of Chemistry and Physics, David R. Lide, ed., CRC Press, 1991.

4-47. G.E. Rhead, M.G. Barthes, C. Argile, Thin Sol. Films 82, 201 (1981).

4-48. D.C Jackson, T.E. Gallon, and A. Chambers, Surf. Sci. 36, 381 (1973).

4-49. J.P. Biberian and G.E. Rhead, J. Phys. F 3, 675 (1973).

4-50. A. Clark, *The Theory of Asorption and Catalysis*, Academic Press, 1970.

4-51. R. Rudham and F.S. Stone, *Chemisorption*, W.E. Garner, ed., Butterworth, 1957.

4-52. T.J. Jennings and F.S. Stone, Advan. Catalysis 9, 441 (1957).

4-53. S.J. Lombardo and A.T. Bell, Surf. Sci. Rep. 13, 1 (1991).

4-54. A W. Adamson, *Physical Chemistry of Surfaces*, 5th ed., John Wiley & Sons, (1982).

4-55. D.A. King and M.G. Wells, Proc. Roy. Soc. London A 339, 245 (1974).

4-56. J.A. Yarmoff and F. R. McFreely, J. Appl. Phys. 63(11), 5213 (1988).

# 5

# SUMMARY AND CONCLUSIONS

The effects of surface preparation on W CVD processes typically encountered in semiconductor manufacturing have been investigated in a UHV environment. This study was unique in that the traditional techniques of surface science, *i.e.* Auger electron spectroscopy was used *in situ* to monitor the initial stages of W film growth *via* $WF_6$ surface reactions. A UHV system was specially contructed in order to simulate and study CVD film growth in a precisely controlled environment, without damaging the sensitive Auger optics and electronics. The design, construction, and maintenance of a unique UHV gas dosing system were described in detail, and several electron beam and instrument effects were demonstrated that could have had a siginificant impact on the Auger data, if certain precautionary steps were not taken.

The technique of sequentially exposing Si(100) surfaces to $WF_6$ combined with in situ Auger measurements has enabled the $WF_6$ + Si reaction to be examined in a unique way. A comparison was made of the deposition of W thin films on Si(100) samples sputter cleaned in UHV to films deposited on HF-cleaned samples by measuring W deposition rates as the films were grown. The influence of residual O contamination in amounts typically encountered in a manufacturing environment were shown to have significant effects on the deposition rate of W and on the W/Si interface morphology. A thin (~ 1 nm) surface oxide layer impeded W film growth at moderate deposition temperatures (300 to 450 °C), and led to an interface structure with large scale (up to 300 nm pore size) porosity at temperatures above 450 °C.

The kinetics of $WF_6$ and $SiH_4$ reactions with RIS, MOCVD, and LPCVD TiN thin films were studied in a UHV environment. The $WF_6$ reaction nucleated a W film on TiN *via* kinetics that were sensitive to the chemical and physical properties of the TiN surfaces. A first order kinetic model was developed and used to make quantitative comparisons of $WF_6$ adsorption on the different TiN surfaces. Alternate kinetic models and interpretations were discussed. The W

uptake data was also anlayzed in terms of the traditional thin film growth modes, *i.e.* islanding versus growth by layers, *etc.* The data showed that the most likely mode of W deposition was the purely random, or Poisson growth mode throughout the temperature range studied.

The initial reaction rate was as much as two orders of magnitude greater on the sputter cleaned TiN surface than on one oxidized by exposure to atmospheric air. The initial $WF_6$ reaction rates were the same for all of the TiN samples, but the reaction deposited more W on the TiN films with greater surface roughness. Between the temperatures of 300 and 550 °C the effective activation energy for the sputter cleaned TiN samples was 0.04 eV and for the oxidized "as received" samples it was 0.6 eV. It has been shown for the first time that a thermally activated mechanism, presumably surface diffusion, dominates the reaction on oxidized TiN, in contrast to the case for a UHV sputter-cleaned surface. At higher exposures, the desorption of F limits the W deposition rate for both surfaces.

A $SiH_4$ pre-exposure of TiN accelerates the subsequent $WF_6$ reaction by depositing Si. The deposited Si reacts with the $WF_6$, providig a facile pathway for F desorption, presumably *via* formation of volatile $SiF_4$. The bonding of the deposited Si was dependent on the amount of initial surface oxidation. According to Auger line shape analysis, the Si bonds to the oxidized TiN as Si-O and to the clean TiN as elemental Si or nitride. The activation energy for the $SiH_4$ pre-exposed TiN is 0.13 eV for both clean and oxidized TiN, which is comparable to the value for $WF_6$ growth on Si, 0.16 eV.

# APPENDIX A

# ELECTRON BEAM AND INSTRUMENTAL EFFECTS

The incident Auger electron beam produced several significant effects that were observed throughout the course of these studies. The beam caused surface chemical decomposition, it stimulated desorption of surface molecules, and it appeared to assist in the adsorption of C from the UHV ambient. The sensitivity of the Auger data to instrument settings including pass energy scan speed and emission current were also explored. This Appendix illustrates these effects and explains what steps were taken to minimize these effects during routine acquisition of data.

The electron beam appeared to decompose the oxidized TiN surfaces. Fig. A-1 shows how the peak-to-peak amplitudes of the O(KLL) and Ti(LMV) transitions changed upon continuous exposure to a 3 kV electron beam. The O peak decreases in magnitude and the Ti peak increases, suggesting that the electron beam is breaking the Ti-O bonds allowing desorption or diffusion of the O atoms. The effect is most dramatic during the first minute of exposure. This observation agrees with the results of a study by Mathieu, *et.al.* [1] which showed that an electron beam has a localized reducing effect on titanium oxide films. They studied Ti-O films of different stoichiometries and found that $TiO_2$ films were more stable under electron beam bombardment than $TiO_x$ films with $x < 2$. The current densities had to greater than ~ 10 A/cm$^2$ at 5 kV in order to see the effect over a period of a couple minutes. The beam current density for this work was typically ~ 13 A/cm$^2$ at 3 kV, *cf.* Chapter 2, which is consistent with expectations based on Mathieu's results.

Deposition of C was observed when TiN surfaces under prolonged electron beam exposure. Fig. A-2 shows how the magnitude of the C(KLL) transition increased with time for a TiN surface exposed to the electron beam. The C signal increased by about 4% per minute of exposure. The error bars shown are estimated from a combination of uncertainties including

physical measurement of the peaks and instrument settings. There was also a slight change in shape of the C(KLL) peak as the exposure time increased in that the peak began to resemble the peak shape usually associated with a carbidic species of C [2]. This effect is fairly common in scanning electron microscopes where the ambient pressure is typically ~$10^{-6}$ Torr. Although this rate of C deposition is not significant in the time scale (~ 1 minute) in which the Auger data were collected, it is useful to know to what extent the electron beam is changing the surface being studied.

Chapter 4 showed that F accumulated on the TiN surfaces as they were exposed to $WF_6$. This F was very unstable when exposed to the electron beam. The magnitude of the F(KLL) transition changed dramatically when exposed to the electron beam for just a few seconds. Fig. A-3 shows the decrease of the F(KLL) peak-to-peak amplitude when a sample was continuously exposed to an electron beam. After only a few seconds the F signal had decreased substantially. This phenomena has been previously reported by Creighton, *et.al.* [3], who used beam densities nearly two orders of magnitude lower than those used in this work in order to perform quantitative measurements for surface F concentrations. Since such low current densities were impractical due to the repetitious nature of the experiments performed in this work, the effects of electron beam were minimized by keeping the exposure times as small as possible.

The Si atoms that were adsorbed onto the TiN surfaces from the $SiH_4$ exposures were also quite sensitive to the electron beam. When the oxidized TiN was exposed to $SiH_4$, the adsorbed Si atoms initially produced a Si(LVV) peak shape that suggested Si-O bonding. Upon exposure to the electron beam for a few seconds however, the Si(LVV) peak shape began to transform, as shown in Fig. A-4. Here the Si(LVV) peak is shown for increasing electron beam exposure time up to 10 minutes. The peak shape at 10 minutes is suggestive of a more covalently-bonded Si species [2]. This effect has also been reported by other researchers [4]. The electron beam has a localized reducing effect on the $SiO_2$, causing desorption of the O. The decomposition of the Si-O layers studied in this work occurred under much lower beam current densities and energies typically required to decompose a $SiO_2$ surface. At beam current densities use in this work, times of ~ 70 minutes were required in to observe the effect on a thermally-grown $SiO_2$ film [4]. This emphasizes the fragile nature of the Si-O layers formed by the $SiH_4$ exposures.

The influence of instrument parameters such as pass energy scan speed, and electron gun emission current on the Auger peak-to-peak magnitudes are shown in Figs. A-5 and A-6. In Fig. A-5 the peak-to-peak amplitude of the O(KLL) peak is plotted for several different emission current settings. The normal operating range of emission current shown in the Figure

corresponds to a ± 4% range in peak-to-peak magnitudes. The emission current tended to drift during the experiments because the filament current did not have sufficient time to completely stabilize. This was because the filament current was reduced below the emission point during gas exposures to avoid chemical reactions on or near the filament. The filament current was then increased to give an emission current of 1 mA for the Auger data acquisitions. Thus the emission current was monitored during Auger data acquisitions and adjusted as necessary to stay within the operating range shown in Fig. A-5. The 4% uncertainty is relatively small as evident by the data in Fig. 4-10.

All of the Auger spectra were physically recorded on an x-y chart recorder. Fig. A-6 shows the response of the magnitude of the peak-to-peak O(KLL) transition as recorded on the chart recorder to the CMA pass energy scan speed. This plot shows how sensitive the data were to scan speed settings. Throughout the course of the gas dosing experiments, the scan speed was typically kept between 1 and 2 eV/sec, which contributed a peak-to-peak amplitude variation of less than 2%.

The influence of additional instrument parameters were investigated including modulation voltage, lock-in time constant, electron beam focus, electron multiplier voltage, and sample position along the CMA axis. These settings were usually optimized and held fixed unless a hardware change, electronics repair mandated some adjustment.

**References for Appendix A**

A-1. H.J. Mathieu, J.B. Mathieu, D.E. McClure, and D. Landolt, J.Vac. Sci. Technol. 14(4), 1023 (1977).

A-2. L.E. Davis, N.C. MacDonald, P.W. Palmberg, G.E. Raich, and R.E. Weber, "Handbook of Auger Electron Spectroscopy", Physical Electronics Division, Perkin-Elmer Corp., Eden Prairie, MN (1978).

A-3. J.R. Creighton, J. Electrochem. Soc. 136, 271 (1989).

A-4. S. Ichimura and R. Schimizu, J. Appl. Phys. 50(9), 6020 (1979).

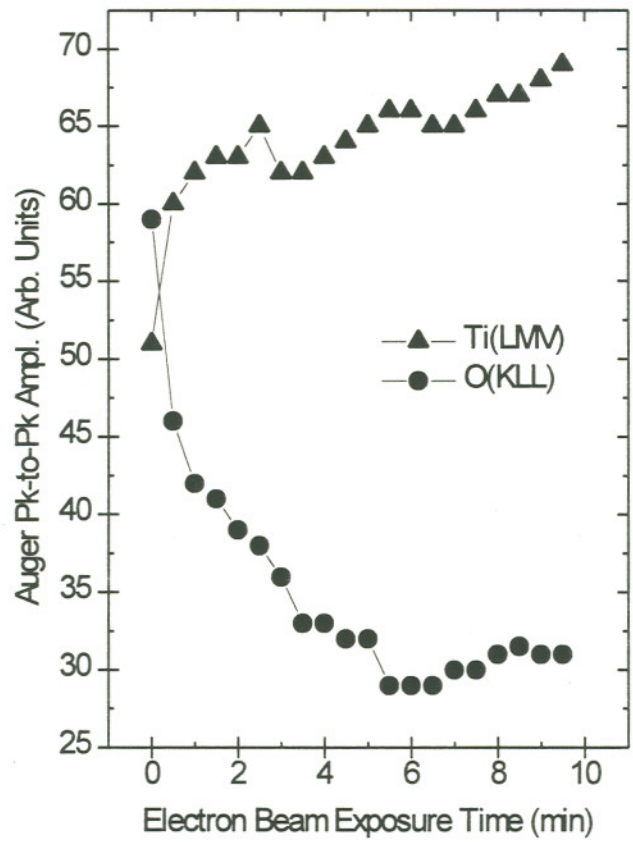


Figure A-1. Auger peak-to-peak amplitudes of the Ti(LMV) and O(KLL) transitions during prolonged exposure to the electron beam, ~ 13 A/cm$^2$.

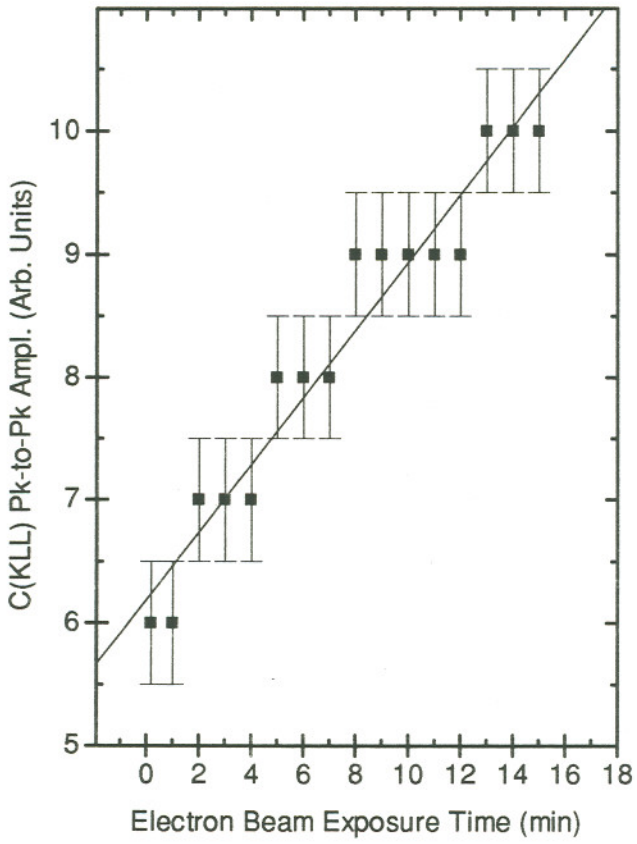


Figure A-2. Change in magnitude of the C(KLL) transition from a TiN surface upon prolonged exposure to an electron beam, ~ 13 A/cm$^2$.

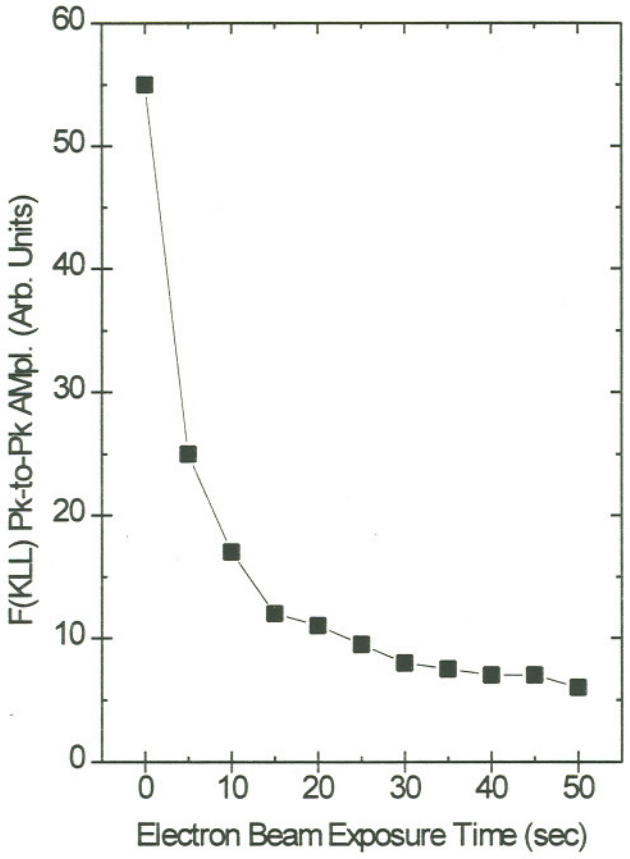


Figure A-3. Electron stimulated desorption of F from a $WF_6$-exposed TiN surface.

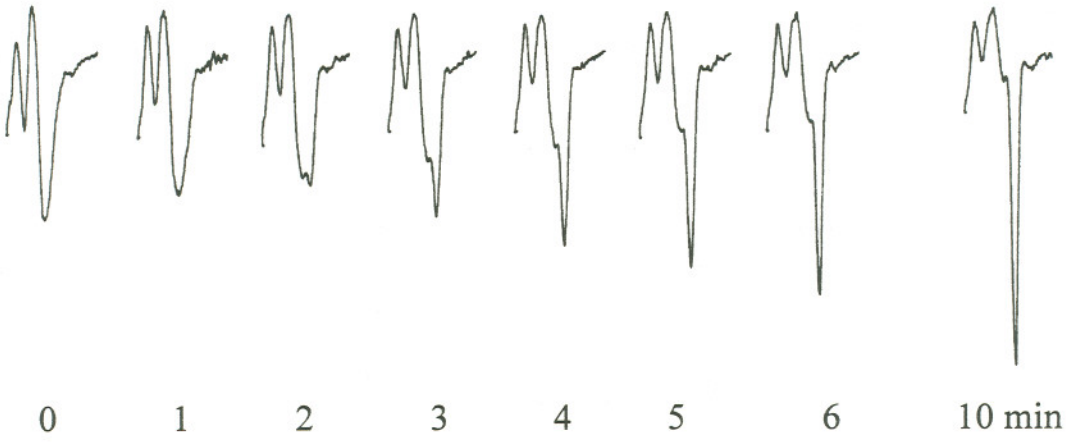


Figure A-4. Sensitivity of Si(LVV) peak shape to electron beam exposure.

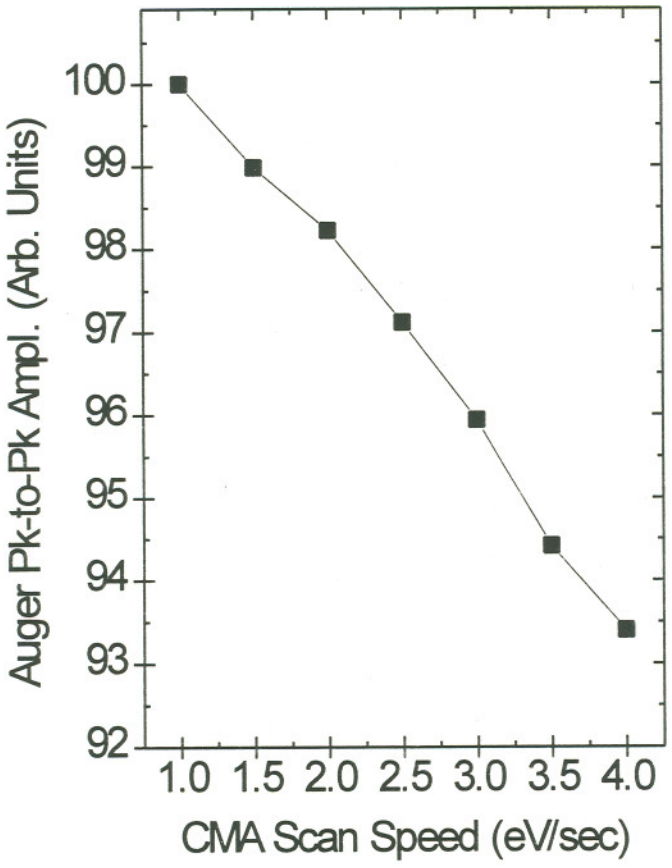


Figure A-5. Sensitivity of O(KLL) peak-to-peak amplitude to CMA scan speed.

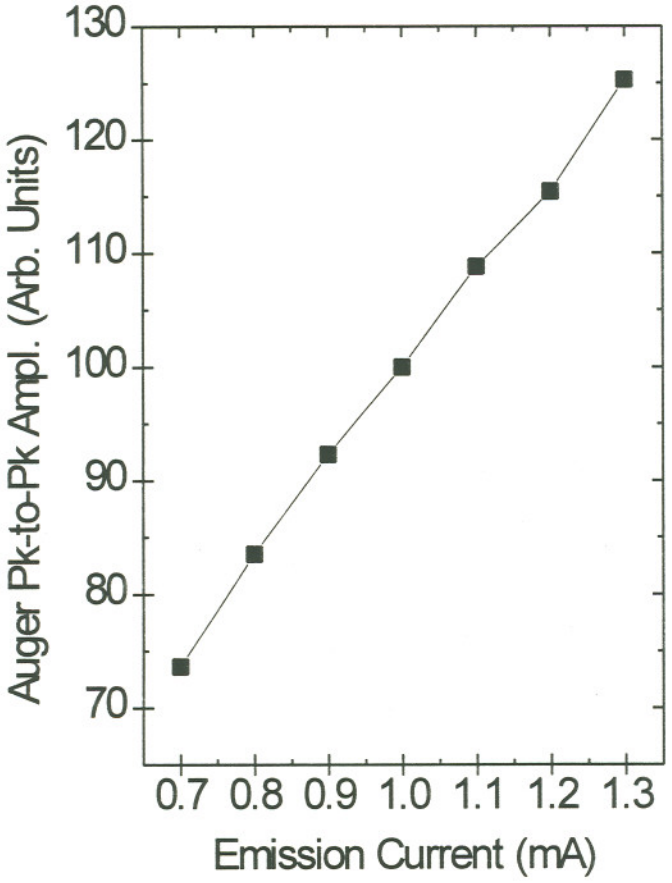


Figure A-6. Sensitivity of O(KLL) peak-to-peak amplitude to electron gun emission current.

Scott L. Lantz was born and raised in Williams County, Ohio, and attended North Central High School in the town of Pioneer. He later attended the University of Akron, and graduated in 1988 with a Bachelor of Science degree in physics and a minor degree in mathematics. He pursued graduate studies in physics at Montana State University, and graduated with a Master of Science degree in 1990. He then enrolled in a Ph.D. program in electrical engineering at the Oregon Graduate Institute, and graduated in the fall of 1994. His research interests have included surface science, and the applications of surface science in semiconductor manufacturing process development, particularly with chemical vapor deposition processes. He is currently employed by Intel Corporation as a senior process engineer.